POLITECNICO DI MILANO
DEPARTMENT OF MECHANICAL ENGINEERING
DOCTORAL PROGRAMME IN MECHANICAL ENGINEERING

MULTIDISCIPLINARY DESIGN OF ELECTRIC VEHICLES BASED ON HIERARCHICAL MULTI-OBJECTIVE OPTIMIZATION

Doctoral Dissertation of:
Kesavan Ramakrishnan

Supervisor:
Prof. Gianpiero Mastinu, Prof. Massimiliano Gobbi

Tutor:
Prof. Federico Cheli, Prof. Francesco Castelli Dezza

The Chair of the Doctoral Program:
Prof. Bianca Maria Colosimo

AY 2014-2017 – cycle XXIX

I dedicate this dissertation to my family and wife

Acknowledgements

Foremost I would like to thank my advisor, Professor Gianpiro Mastinu, from the bottom of my heart for his generous support, motivation, encouragement. His expert guidance helped me throughout the project with the right theoretical perspectives whenever I needed them.

I express my heartfelt and profound gratitude to Professor Massimiliano Gobbi, who shared his vast knowledge of the optimisation procedures. He was approachable for any queries at any time. I am also grateful to Professor Damir Žarko for his untiring support, keen interest, valuable guidance on electric machine modelling.

I would like to thank Brembo S.p.A, for the industrial opportunity where I had a chance for learning and professional development. My special thanks to Miotto Alessio, Carbone Fabio, and Galizzi Valerio for spending their precious time during my tenure in the company.

My deep sense of gratitude to my colleagues Giorgio Previati, Federico Maria Ballo, and Liunan Yang for the stimulating discussions and friendship. I also thank Mario Pennati for his support and cooperation during the time I spent in the lab.

I am very much thankful to all the researchers and professors in ADEPT (Advanced Electric Powertrain Technology) consortium for all collaborations. The training schools offered by ADEPT has broadened my knowledge in the area of advanced electric powertrain technology.

I thank my wife, Swarna, for standing next to me and giving her love and support. I am always indebted to my parents for everything that they have done for me. I would like to mention special thanks to my brother and sister. All of these would not have been possible without their constant encouragement.

This thesis became a reality with the kind support of many individuals. I would like to

extend my sincere thanks to all of them. My eternal gratitude to Politecnico di Milano-Italy, ADEPT consortium, and the European Union for the Marie-curie fellowship. I perceive this golden opportunity as a key milestone in my career development.

Extended abstract

This thesis presents a general methodology for the multidisciplinary optimal design of electric vehicles (EVs). A special attention is devoted to EVs with in-wheel motors. A number of interacting subsystems such as electric motor, power electronics, battery, and suspension are taken into account. Multi-objective optimisation (MOO) techniques are adopted together with analytical target cascading (ATC) for this complex system optimisation. The optimisation problem is partitioned into two levels where the top level consists of a model representing the electric vehicle and the bottom level contains models of battery and suspension. The vehicle model includes an electric motor model and a power electronics model. The objective functions that belong to each subsystem are treated together using MOO techniques, and the ATC coordination strategy is used to manage the interactions that naturally occur between the subsystems. This iterative methodology ensures convergence that meets the system level targets while complying with the subsystem level constraints. Appropriate models of the subsystems are developed for the optimisation purpose.

Outer rotor surface permanent magnet machines are used in the considered in-wheel motor electric vehicle. In order to develop a model to estimate the motor performances with reasonable accuracy and computational time, four possible motor scaling models such as proportional scaling of efficiency map, Willans line model, scalable saturated model, and analytical motor model are evaluated in this study. Out of all these scaling models, the performance of analytical motor model largely depends on the electromagnetic calculation used to estimate the air-gap field solutions. Hence, six widely used analytical/semi-analytical methods are studied in detail. The methods are based primarily on conformal mapping, mode matching, and harmonic modelling. In the case of conformal mapping, the slotted air gap of the complex machine geometry is

transformed to a smooth slotless air gap where the analytical expression for the field solution is known. The solution in the canonical domain is then mapped back to the original slotted air gap. Mode matching or subdomain method, as it is called in different sources, utilises the solution of Laplace's equation to model the slotted air gap. In harmonic modelling, the machine cross-section is divided into homogeneous regions that are represented using Fourier series and coupled with each other using boundary conditions. The boundary value problems in both the mode matching and harmonic models are solved to obtain the field solutions. The performances of these electromagnetic models are evaluated by comparing the global parameters such as cogging torque, electromagnetic torque, back-emf as well as the simulation time with the results from finite element transient analysis. The motor scaling models are also compared against a commercial software. Based on this study, the analytical motor model with complex permeance method is selected.

Since the EVs with in-wheel motors may be prone to have degraded ride comfort performance, a special attention is devoted to the suspension subsystem. The benefits of passive suspension components such as inerter and additional relaxation spring are studied in alleviating the problems associated with the increased unsprung mass. A linear quarter-car model is used to represent the vehicle corner. Three suspension performance indices, namely, discomfort, road holding, and working space are derived analytically for a random irregular road excitation. The suspension architectures featuring the inerter and/or relaxation spring are compared with the conventional passive suspension by taking the performance indices individually. It is proven that the inerter and relaxation spring provide improved performances when they are arranged in specific layouts.

The battery model is used to arrange the cells in a balanced scheme to achieve uniform utilisation of the cells. The total number of cells are calculated from the energy and maximum power requirements of the vehicle. The vehicle mass is modelled as a function of battery and motor sizes.

In this thesis, an optimisation methodology is proposed by combining the benefits of ATC and MOO techniques. A complex problem is partitioned into subsystems which are optimised individually using appropriate optimisers. The interactions between the subsystems are maintained using the ATC coordination strategy. Whenever the subsystems have multiple conflicting objective functions, the MOO techniques are employed to obtain the Pareto-optimal solutions. In the case of conventional All-in-one (AiO) approach, a single optimiser is used for the complete optimisation problem which may not be effective for certain problem types.

The proposed optimisation methodology is demonstrated on a multi-disciplinary design

problem of in-wheel motor electric vehicles. The Pareto-optimal solutions are obtained at the system level as well as the subsystem level. Performance difference between the proposed ATC based methodology and AiO approach is evaluated based on the accuracy of the results and computational time. It can be observed that the proposed methodology is much faster than the AiO approach for complex system optimisations.

Contents

CHAPTER 1

Introduction and Literature review

Most of the real-world design problems are complex and have multiple conflicting objectives. For example, in a design optimisation problem of automobiles, the objectives such as fuel economy, acceleration, and comfort can be given different weights based on the vehicle characteristics as in Fig. 1.1. A compact car requires less acceleration compared a performance car. Conversely, the fuel economy requirement of the compact car is high. The multi-objective optimisation (MOO) techniques can be employed to obtain the Pareto-optimal set that can give the decision makers an insight into the problem before the final selection. Electric vehicles are particularly sensitive to the mentioned trade-offs as the energy stored on-board is quite limited. Hence, the energy consumption and acceleration requirements have to be studied carefully.

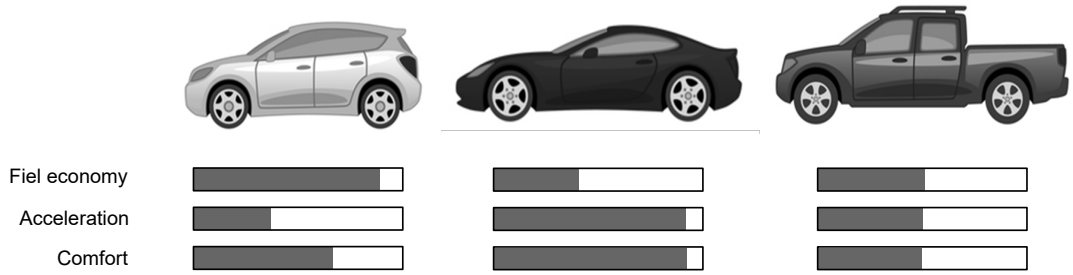

Fig. 1.1: *Performance requirements of vehicles, Images from http://www.travisma.com*

An in-wheel electric vehicle with outer rotor electric motors is considered as the reference vehicle. It uses Li-ion battery cells in the battery pack and the independent suspension systems.

Several methods exist in the literature to solve the multi-objective optimisation problems as listed in Table 1.1.

Table 1.1: *Summary of optimisation methods used for vehicle design*

	Methods	Description	Citations
Scalarization methods	Weighted sum, constraint method, goal programming	MOO problems are transformed into single objective optimisation problems	[1] [2]
Pareto methods	Pareto filtering, weighted sum method, constraint method, analytical method, multi-objective evolutionary algorithms	Objective functions are simultaneously handled to obtain the complete Pareto-optimal set	[3–6]
Multi-level models	Analytical target cascading (ATC), collaborative optimisation (CO), network target coordination (NTC), bi-level integrated system synthesis (BLISS)	complex systems are decomposed into multiple subsystems and the interactions between the subsystems are maintained using coordination strategies.	[7–10]

Scalarization methods transform a multi-objective optimisation problem into a single objective problem either by weighting the normalised objective functions (weighted sum method) or by optimising one of the objective functions while using the others as constraints (constraint method). In the goal programming method, target values are defined for objective functions and the deviations from these target values are minimised. The scalarization methods require subjective preferences on the objective functions before obtaining the results. On the other hand, the Pareto methods handle the objective functions simultaneously. Pareto filtering method numerically filters the non-dominated solutions from the complete feasible solution space. Though the mathematical formulations of the weighted sum and constraint Pareto methods are similar to the scalarization methods, their weights and constraint values are varied, respectively, to get the complete Pareto optimal solutions. Derivation of the Pareto-optimal solutions analytically may utilise the Fritz-John necessary condition for optimality [11]. The multi-objective evolutionary algorithms rank the population by nondomination and work iteratively to obtain the Pareto front. The authors in [5, 6] have optimised the electric motor geometry based on the conflicting design objectives at the vehicle level using Pareto filtering. Bingzhan et al. applied multi-objective evolutionary algorithms for component sizing and the control strategy optimisation of hybrid electric powertrain in [12]. However, the model complexity that can be handled by the single level or All-in-one (AiO) multi-objective optimisation is limited.

In the multi-level models, a complex system is decomposed into multiple subsystems and the interactions between them are maintained using coordination strategies. Analytical target cascading (ATC), collaborative optimisation (CO), network target coordination (NTC), and bi-level integrated system synthesis (BLISS) are the possible coordination strategies. Especially, the ATC algorithm is used for the problems in the automotive industry. Kim et al. structured the ATC algorithm based on the activities performed in the product development organisations of automotive industry in [7, 13]. The convergence of the method was studied in [14] and proved that an optimum solution could be found by recursively solving the hierarchical problems. Researchers have successfully implemented this approach in different interesting applications such as engine calibration [15–17], combined product and process design [18], and marketing linked product development process [19]. Bayrak et al. optimised the hybrid electric powertrain architectures and sized the components in [20]. In the presented ATC formulations, the authors considered single objective function for each subsystem. On the other hand, by combing the MOO techniques with ATC algorithm, it is possible to handle multiple objective functions and obtain the Pareto-optimal solutions.

Hence, in this thesis, the design optimisation problem of the in-wheel motor electric vehicles that involves multiple design objectives and multi-physics subsystems is solved by combining the ATC and MOO techniques. The system model is partitioned into manageable subsystems and each mathematical programming problem is solved using dedicated optimiser. The possible algorithms that can be used for solving the subsystems are summarised and compared in Table 1.2 [21]. The multiple objective functions that belong to each subsystem are treated together using MOO techniques. The ATC algorithm achieves the synergy between the solutions from different subsystems.

Table 1.2: *Methods for solving optimisation problem*

Method	Type	Efficiency	Accuracy	Discrete design variables
Exhaustive	Nonderivative	- -	++ (discrete variables) -(continuous variables)	Yes
Uniformly distributed sequences	Nonderivative	-	-	Yes
Evolutionary strategies	Nonderivative	+	+	Yes
"Standard" nonlinear programming (e.g. Sequential quadratic programming)	Derivative	++	+	No

Note: - - very bad; - poor; + good; ++ very good.

The exhaustive search method estimates the objective functions by systematically enumerating all feasible design candidates and hence it is computationally expensive. The computation time can be reduced without much loss in the accuracy by using uniformly distributed sequences (e.g. Sobol). For the optimisation problems with discrete design variables, the evolutionary strategies (e.g. genetic algorithm) are the best performing methods. Instead, the "standard" nonlinear programming such as sequential quadratic programming can be adopted when the objective functions and constraints are twice continuously differentiable and the design variables are continuous.

In the in-wheel motor electric vehicle optimisation problem, the considered subsystems are the electric motor, power electronics, suspension, and battery. Detailed models are presented for the motor and suspension subsystems. A simplified analytical model estimates the losses in the inverter and a battery model arranges the cells in a balanced scheme to ensure their equal utilisation.

Modelling of electric motor

In order to mathematically model the in-wheel motors, an appropriate method should be selected from the possible options in the literature by analysing their performance differences. Therefore, the results of proportional scaling of efficiency map, Willans line (WL) model, scalable saturated motor model, and analytical motor model are compared against commercial software. The proportional scaling of efficiency map model is valid only in the neighbourhood of the reference motor where the efficiency map would not change drastically [22]. The WL model was developed to relate the input fuel energy and the output power in internal combustion engines [23]. The approach was extended to electromechanical energy conversion devices such as electric machines in [24]. The accuracy of WL model in estimating the operating efficiencies of the scaled machines is limited. The scalable saturated motor model [25], which combines the current-dependent flux linkage and loss models in [26, 27] and the scaling laws in [28–31], gives good results compared to FEM calculations.

There are many accurate and computationally effective analytical motor models in the literature, which have their own merits and demerits. It is important to evaluate their differences to get the maximum benefit. Hence, an attempt is made here to compare Carter method, relative permeance model [32], complex relative permeance model [33], Schwarz-Christoffel Toolbox based semi-analytical conformal mapping (SC) [34], mode-matching (MM) [35–38], and harmonic model (HM) [39, 40]. The first four models are fundamentally based on the conformal mapping. For the semi-analytical conformal mapping, MATLAB SC Toolbox is utilised to numerically map the complex polygons to simple rectangles. The MM and HM use the solutions

of Laplace's or Poisson's equations that are represented in the tangential direction as Fourier series [35,41]. The considered analytical models assume infinite magnetic permeability of the stator and rotor core and ignore the saturation effect in the air-gap field solution. This approach is justified by the fact that the influence of saturation on the field distribution is not significant in the surface permanent magnet machines (SPM). Since the influence of end winding is not considered in these models, they can be used in a two-dimensional plane to solve the Laplace's or Poisson's equations based on scalar or vector magnetic potential formulation [39, 42–44]. The field solutions in the air gap can then be post-processed to calculate the cogging torque, electromagnetic torque, back-emf, and losses. After analysing the results in detail, the complex relative permeance based analytical motor model [45] that offers closed form solutions of the global parameters is taken to model the in-wheel motor [46].

Modelling of suspension

Increased unsprung mass of the in-wheel motor electric vehicles is one of the key concerns that the designers have to address while optimising the ride comfort performances. The passive suspension components such as inerter and relaxation spring can be taken into account to improve the dynamic behaviours of the conventional suspension system [47]. The performance of the additional passive components were proven to give benefits in [48–50]. The thesis presents a theoretical evaluation of different suspension architectures to understand their performance differences considering the increased unsprung mass. The suspension architectures are optimised for the vehicle body discomfort, road holding, and working space as in [6, 51].

Structure of the document

Chapter 2 provides a brief overview of multi-objective optimisation methods and multi-level optimisation. Mathematical formulation of the ATC algorithm which will be used in the optimisation of in-wheel motor electric vehicles is presented.
In Chapter 3, the electromagnetic modelling techniques are compared in terms of accuracy and calculation time. The global parameters such cogging torque, total torque, back-emf, and core losses are calculated using six analytical models and the results are compared against a FEM model.
Chapter 4 discusses the electric motor scaling methods such as proportional scaling of efficiency map, Willans line (WL) model, scalable saturated motor model, and analytical motor model. The results obtained from the scaling methods are compared against Motor-CAD software results.
Thermal and acoustic behaviours of the electric motor are studied in Chapter 5 and 6

respectively. A thermal model based on lumped parameter thermal networks (LPTN) is built for the considered outer rotor SPM machine. A distributed loss and capacitance (DLC) element as proposed in [52] is used for the improved estimation of nodal temperatures. The LPTN network is solved by introducing the losses obtained from the motor model and considering the effects of rotational speed on boundary conditions. For the acoustic calculation, the electromagnetically induced radial forces, obtained from the motor model, are used as the excitation forces. As the rotation speed of the moving noise source (rotor) is low, it can be assumed as a stationary member [53] and the analytical acoustic models of an outer stator motor [54–56], available in the literature, can be adopted.

Chapter 7 examines the benefits of passive suspension components such inerter and relaxation spring in improving the suspension performances. Six different suspension architectures are studied. The best performing suspension architecture is selected and optimised along with the in-wheel motor to mitigate the problems associated with the increased unsprung mass.

In Chapter 8, the in-wheel motor electric vehicle is optimised using the proposed hierarchical multi-objective optimisation algorithm and its performance is compared with AiO optimisation approach. The AiO multi-objective optimisation problem is formulated as presented in [4, 51]. In the optimisation problem, the vehicle mass should be modelled as a function of motor size and number of battery cells for appropriate results. Since the number of battery cells is an integer valued design variable, the evolutionary algorithms, which are computationally expensive, are required. The proposed ATC based methodology divides the problem into two levels where the subsystem models are arranged hierarchically. The subsystems are solved individually using appropriate optimisation techniques and the coordination strategy (ATC) helps to achieve synergy between the solutions. This approach reduces the overall calculation time significantly without comprising on the accuracy.

CHAPTER 2

Complex system optimisation

A complex system such as electric vehicle involves interacting subsystems with multiple design objectives. Different methodologies have been proposed in the literature to partition the system into manageable subsystems and to optimise them in isolation using suitable algorithms. The interactions between the subsystems, which closely mimic design groups in a product development organisation, can be managed using feedback based coordination strategies. Thus the complex system design optimisation problems can be solved for the synergised optimum solution that meets the system level targets while complying with the subsystem level constraints. Collaborative optimisation (CO), Analytical target cascading (ATC), network target coordination (NTC), and bi-level integrated system synthesis (BLISS) are the widely-used coordination strategies. The ATC algorithm is preferred specifically in the automotive industry.

In order to optimise two or more objective functions in each subsystem, the MOO techniques can be adopted. The Pareto-optimal solution set could assist the designers to analyse the possible trade-offs between objective functions. By combining the MOO techniques with the hierarchical ATC algorithm, the problem complexities can be managed and the Pareto-optimal solutions can be derived synergistically. This chapter introduces the MOO techniques and multi-level optimisation algorithms that will be used later for the optimisation of in-wheel motor electric vehicle parameters.

2.1 Multi-objective optimisation

In most of the practical optimisation problems, the designers have to handle more than one objective functions. When an attempt to improve one objective function worsens the other, it is not possible to derive a single optimum solution. Whereas the MOO techniques produce the Pareto-optimal set which are the best-compromised solutions of the problem. The general MOO problem is formulated as in [4, 57, 58],

$$\min_{\mathbf{x}\in\mathbb{R}^{n_{dv}}} \mathbf{F}(\mathbf{x}) \tag{2.1}$$

subject to

$$\begin{aligned} \mathbf{G}(\mathbf{x}) &< 0 \\ \mathbf{H}(\mathbf{x}) &= 0 \\ \mathbf{x} &\in \mathbf{X} \end{aligned}$$

where $\mathbf{x} = (x_1, x_2, ..., x_n)$ is the design variables vector, $\mathbf{F}(\mathbf{x}) = (f_1(\mathbf{x}), f_2(\mathbf{x}), ..., f_k(\mathbf{x}))$ is the objective functions vector, $\mathbf{G}(\mathbf{x}) = (g_1(\mathbf{x}), g_2(\mathbf{x}), ..., g_m(\mathbf{x}))$ is the inequality constraints vector, $\mathbf{H}(\mathbf{x}) = (h_1(\mathbf{x}), h_2(\mathbf{x}), ..., h_m(\mathbf{x}))$ is the equality constraints vector, and $\mathbf{X}$ defines the upper and lower bounds of the design variables.

2.1.1 Pareto optimal solution

In a multi-objective optimisation problem with n design variables and k objective functions, $\mathbf{x}^*$ is defined as the Pareto-optimal solution if there does not exist another solution $\mathbf{x} \in S$ (feasible space) such that:

$$\begin{aligned} f_j(\mathbf{x}) \leq f_j(\mathbf{x}^*) \quad j = 1, 2, ..., k \\ \exists l: \ f_l(\mathbf{x}) < f_l(\mathbf{x}^*) \end{aligned} \tag{2.2}$$

The condition for Pareto-optimal solution in (2.2) states that it is not possible to improve any objective function without worsening at least one of the others. For all the non-Pareto solutions, at least one of the objective function can be improved without affecting the others. Pareto-optimal fronts of a problem with 2 design variable and 2 objective functions are given in both objective functions and design variables domains in Fig. 2.1. A weak Pareto-optimal front includes also the region where $f_1 = f_2$ (marked in red) and the same is mathematically formulated as in (2.3).
$\nexists\, x$

$$\begin{aligned} f_j(\mathbf{x}) < f_j(\mathbf{x}^*) \quad j = 1, 2, ..., k \\ \exists l: \ f_l(\mathbf{x}) < f_l(\mathbf{x}^*) \end{aligned} \tag{2.3}$$

A Pareto-optimal solution can be regarded as the global solution only when the MOO problem is convex or quasi-convex [59, 60].

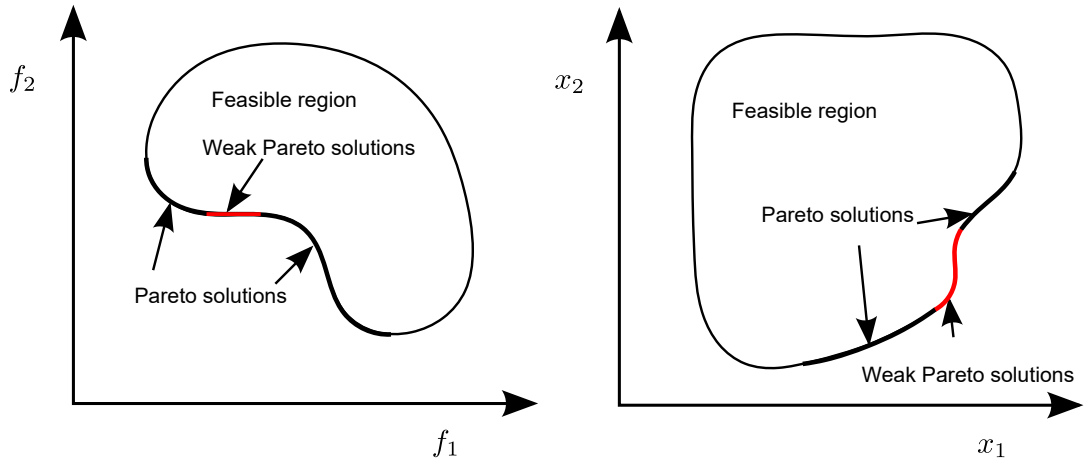

(a) Objective functions domain (b) Design variables domain

Fig. 2.1: *Schematic diagram of Pareto optimal solutions*

2.1.2 Calculation methods for Pareto-optimal solution

As a first step, the problem is formulated according to (2.1). The feasible space of the design variables that meets all the constraints is computed. Global Sensitivity Analysis (GSA) [4] is used to understand the relationship between the design variables and the objective functions. The GSA can also be used to assess the correlation between the objective functions. When the objective functions are strongly correlated, the redundancy can be eliminated by reducing the number of objective functions. The Pareto-optimal solution can then be calculated between the partially correlated or conflicting objective functions using the methods discussed below.

Numerical sorting of Pareto-optimal set:

An exhaustive search method that considers all the equidistant points on a regular grid of design variables requires a large number of functional evaluations. Hence, a Sobol low discrepancy sequence is used for sampling the design variables within their bounds for better efficiency [61]. The objective functions are calculated for each combination of the design variables and the Pareto-optimal solution set that satisfy the conditions in (2.2) is computed.

Constraint method:

Constraint method is the most effective option for calculating the Pareto-optimal set [4]. The problem is formulated as in (2.4) where only one objective function is considered and the others are converted to constraints.

$$\min_{\mathbf{x}\in\mathcal{F}} \; f_1(\mathbf{x})$$
$$f_2(\mathbf{x}) \geq \epsilon_2 \quad f_3(\mathbf{x}) \geq \epsilon_3 \quad \ldots \quad f_k(\mathbf{x}) \geq \epsilon_k \tag{2.4}$$

The complete Pareto-optimal set can be obtained by varying the values of $\epsilon_{i=2,3..n_k}$ within the interested range of the objective functions.

Weighted sum method:

The method scalarises the multi-objective problem by summing the normalised objective functions in (2.5). Each objective function is given a weight (λ_i) which is varied during the optimisation process to get the Pareto-optimal set.

$$\min_{\mathbf{x}\in\mathcal{F}} \quad \lambda_1 \, \bar{f}_1(\mathbf{x}) + \lambda_2 \, \bar{f}_2(\mathbf{x}) + \ldots + \lambda_k \, \bar{f}_k(\mathbf{x}) \tag{2.5}$$

where

$$0 \leq \lambda_i \leq 1 \, ; \quad \sum_{i=1}^{k} \lambda_i = 1$$

A generic result of weight sum (WS) method is compared with constraint method for a two objective functions problem in Fig. 2.2. It can be observed that WS method is not effective when the problem is not completely convex.

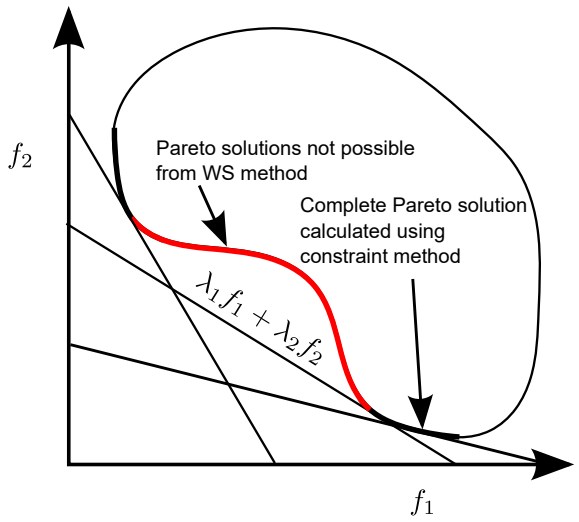

Fig. 2.2: *Comparison between weighted-sum and constraint methods*

In both the weighted sum and constraint methods, it is advisable to normalise the objective functions as in (2.6).

$$\bar{f}_i = \frac{f_i - f_{i,min}}{f_{i,max} - f_{i,min}} \tag{2.6}$$

Evolutionary algorithm

Genetic Algorithms (GA) are probably the most used evolutionary algorithms in MOO. The initial populations can be ranked by nondomination as in Fig. 2.3 and are assigned an artificial fitness associated with their level of Pareto optimality and distribution. The algorithm iteratively converges and the solutions are distributed on the whole Pareto-optimal set [4].

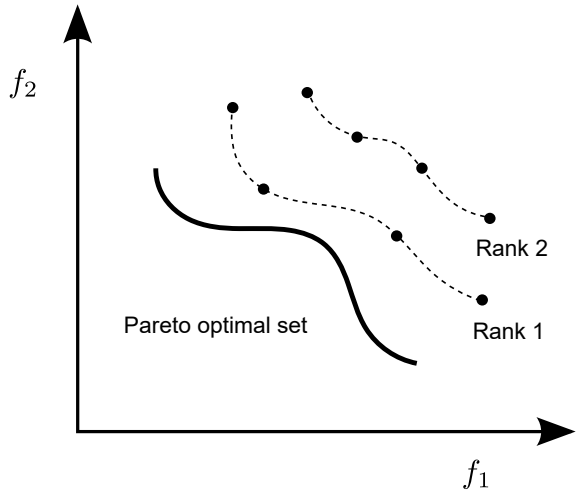

Fig. 2.3: *Population evolution in the objective functions domain. Image adapted from [4]*

Analytical method

Let the objective function and constraint vectors of (2.1) be continuously differentiable with respect to the decision vector $\mathbf{x}^* \in S$. A necessary condition (Fritz John) for $\mathbf{x}^*$ to be the Pareto-optimal [4, 62] is that there must exist vectors $\lambda \in \mathbf{R}^k \geq 0$ and $\mu \in \mathbf{R}^m \geq 0$. If $(\lambda, \mu) \neq (0, 0)$

$$\begin{aligned} \textstyle\sum_{i=1}^{k} \lambda_i \nabla f_i(\mathbf{x}^*) + \sum_{j=1}^{m} \mu_j \nabla g_j(\mathbf{x}^*) = 0 \\ \mu_j g_j(\mathbf{x}^*) = 0 \quad \forall j = 1, ..., m \end{aligned} \tag{2.7}$$

The condition is sufficient if the objective functions and the constraints are convex or pseudoconvex [63–65]. Equation (2.7) can be written in matrix form as given in [58, 66].

$$\mathbf{L} \cdot \delta = 0 \tag{2.8}$$

The term $\mathbf{L}$ represents a $[(n+m)\times(k+m)]$ matrix.

$$\mathbf{L} = \begin{bmatrix} \nabla\mathbf{F} & \nabla\mathbf{G} \\ \mathbf{O} & \mathbf{G} \end{bmatrix} \tag{2.9}$$

where

$$\nabla\mathbf{F} = [\nabla f_1\ \nabla f_2\ ...\ \nabla f_k] \tag{2.10}$$

$$\nabla\mathbf{G} = [\nabla g_1\ \nabla g_2\ ...\ \nabla g_m] \tag{2.11}$$

$$\mathbf{G} = diag(g_1,\ g_2, ...,\ g_m) \tag{2.12}$$

and $\mathbf{O}$ is the null matrix with dimensions $[m\times k]$. δ is a vector containing λ and μ ($\delta = [\lambda \quad \mu]^T$). The matrix form of the Fritz John conditions can be utilised to derive the analytical expression of the Pareto-optimal set. The conditions in (2.7) can be relaxed by removing $\delta \geq 0$. This relaxation implies that we are dealing with necessary conditions also in the presence of convex objective function and constraints. Therefore, the analytical expression derived on the basis of the relaxed form contains the actual Pareto-optimal set and also non-Pareto-optimal solutions which can be eliminated by computing the minimum of each objective function [67].

When the number of design variables are greater than the number of objective functions ($n \geq k$), the non-trivial solutions [68] can be obtained by equating $\mathbf{L^T L}$ to zero.

$$det(\mathbf{L^T L}) = 0 \tag{2.13}$$

If the $\mathbf{L}$ matrix is a square ($n = k$), i.e. the number of design variables is equal to the number of objective functions, the condition is reduced to

$$det(\mathbf{L}) = 0 \quad \Rightarrow \quad \left(\prod_{i=1}^{m} g_i\right) \cdot det(\nabla\mathbf{F}) = 0 \tag{2.14}$$

When the above problem is unconstrained, the $\mathbf{L}$ matrix becomes $\mathbf{L} = \nabla\mathbf{F}$, and the solutions in (2.13) and (2.14) are given as

$$\begin{aligned} det(\nabla\mathbf{F^T}\ \nabla\mathbf{F}) &= 0 \\ det(\nabla\mathbf{F}) &= 0 \end{aligned} \tag{2.15}$$

For a simple multi-objective unconstrained problem, which has two design variables and two objective functions ($n = k = 2$), the generic form Pareto-optimal solution is

$$det(\nabla\mathbf{F}) = 0 \quad \Rightarrow \quad \frac{\partial f_1}{\partial x_1}\cdot\frac{\partial f_2}{\partial x_2} = \frac{\partial f_1}{\partial x_2}\cdot\frac{\partial f_2}{\partial x_1} \tag{2.16}$$

When the number of design variables is less than the number of objective functions ($n \leq k$), $det(\mathbf{L^T L})$ is always zero, and the problem is no longer a minimisation problem. The analytical expression can be simply derived by substitution method [69].

2.2 Single-level optimisation

A complex system involves multi-physics subsystems that interact together to perform a task. In order to optimise the overall system level performances, it has to be formulated as the multi-disciplinary optimisation (MDO) problem. In many cases, the MDO problem is centralised in a single level where all the subsystems are evaluated together as in Fig. 2.4. Though the approach could produce high efficiency in certain situations (when the system model is simple and differentiable with respect to continuous design variables), it is difficult to map many organisational structures due to its centralisation [70].

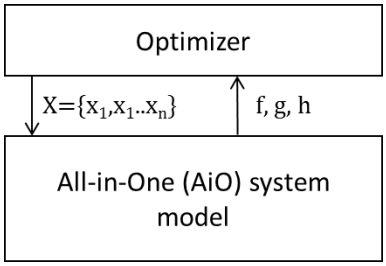

Fig. 2.4: *All-in-one layout*

When there are more than one objective functions in the AiO system model, the multi-objective optimisation techniques, in Section 2.1, can be adopted to handle them simultaneously. However, the problem becomes difficult to be managed when there are more than three objective functions. It may also happen that the design variables are in both integer and continuous domains which can be solved using evolutionary algorithms for optimisation. As the number of functional evaluations required by the evolutionary algorithms are high and in each iteration all the subsystems are evaluated, the single level optimisation of complex systems can be significantly time consuming.

2.3 Multi-level optimisation

In the single level optimisation, all the design decisions are made by a single optimiser. Instead, the complex problem can be partitioned into multiple manageable subsystems based on their functionalities as in Fig. 2.5. These subsystems, which closely mimic design groups in product development organisations, can be solved by exploiting the expertise of each group in terms of dedicated modelling tools and optimisers. As appropriate algorithms are used for each subsystem, the solutions are obtained with reduced computational effort. The system level optimiser coordinates the subsystems to achieve a synergistic solution that meets the overall targets.

A detailed formulation of the analytical target cascading approach is given here and

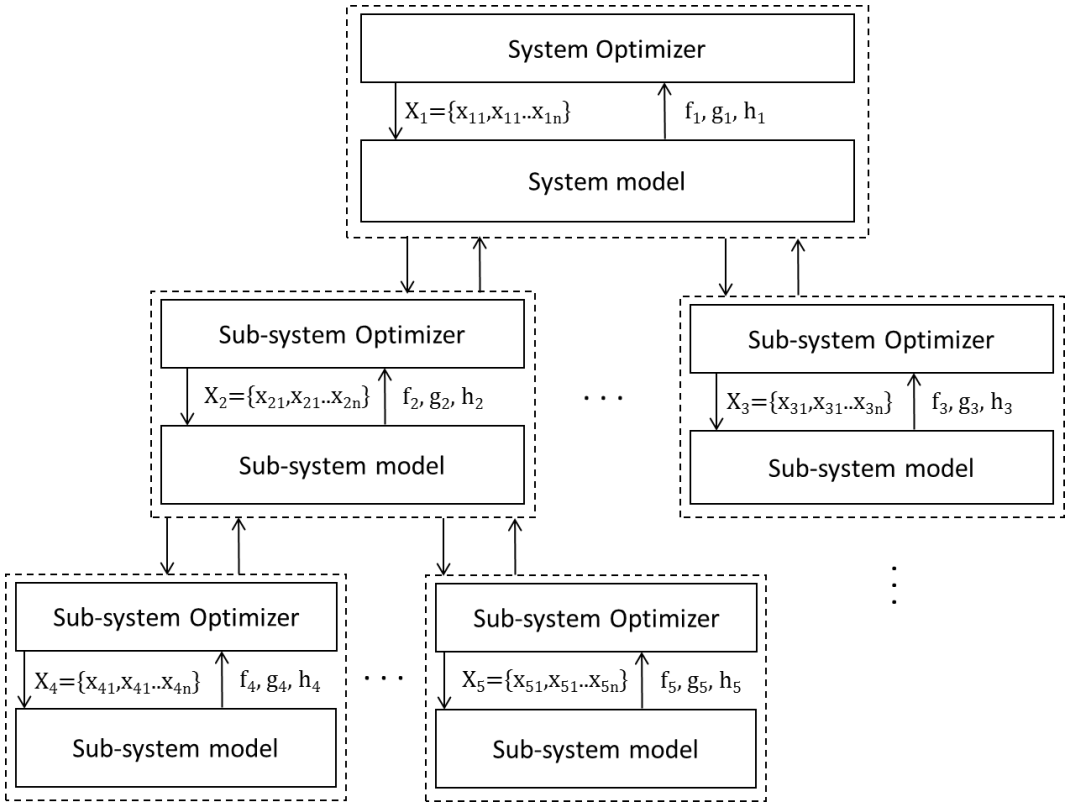

Fig. 2.5: *Multi-level optimisation layout*

the same will be used to solve an in-wheel motor electric vehicle optimisation problem along with MOO techniques in Chapter 8.

2.3.1 Analytical target cascading

A generic flowchart of two level analytical target cascading approach is shown in Fig.2.6, and its mathematical formulation is given in (2.17). The optimised results from system model are cascaded to the subsystems as targets and the responses from subsystem models are given back for further corrections. This feedback based interactions are handled using linking variables. The design variables that are used in multiple subsystem models are treated as shared design variables.

$$\begin{aligned} \min_{\overline{x}_{ij}=\{x_{ij},t_{ij},r_{ij}\}} \quad & f_{ij}(\overline{x}_{ij}) + \phi_{ij}(c_{ij}, v_{ij}, w_{ij}) \\ \text{subject to} \quad & h_{ij}(\overline{x}_{ij}) = 0 \\ & g_{ij}(\overline{x}_{ij}) \leq 0 \\ where, \quad & \phi_{ij} = v_{ij}^T\, c_{ij} + ||w_{ij} \circ c_{ij}||_2^2 \\ & c_{ij} = t_{ij} - r_{(i+1)j} \end{aligned} \tag{2.17}$$

where f_{ij} is the objective functions vector of each sub-system, t_{ij} is the target linking

variables vector from j^{th} element of i^{th} level, $r_{(i+1)j}$ is the response linking variables vector from j^{th} element of $(i+1)^{th}$ level, ϕ_{ij} is the consistency constraints vector which relaxes the equality constraints $(c_{ij} = 0)$ between targets and responses using augmented-lagrangian (AL) function [71], h_{ij} and g_{ij} are the equality and inequality constraints vectors respectively, and x_{ij} is the local design variables vector. The symbol $\circ$ is used to denote term-by-term multiplication of vectors. The Lagrangian multiplier (v) and penalty weights (w) are updated linearly in the successive ATC iterations as in (2.18).

$$\begin{aligned} v^{y+1} &= v^y + 2w^y \circ w^y \circ c^y \\ w^{y+1} &= \beta w^y \end{aligned} \tag{2.18}$$

where y represents the number of iteration. The factor β should be $2 < \beta < 3$ for fast convergence [71]. The convergence criteria is set at the top-level as $||c^y|| < \epsilon_1$ and $||c^y - c^{y-1}|| < \epsilon_2$. The values of ϵ_1 and ϵ_2 are predefined by the designers.

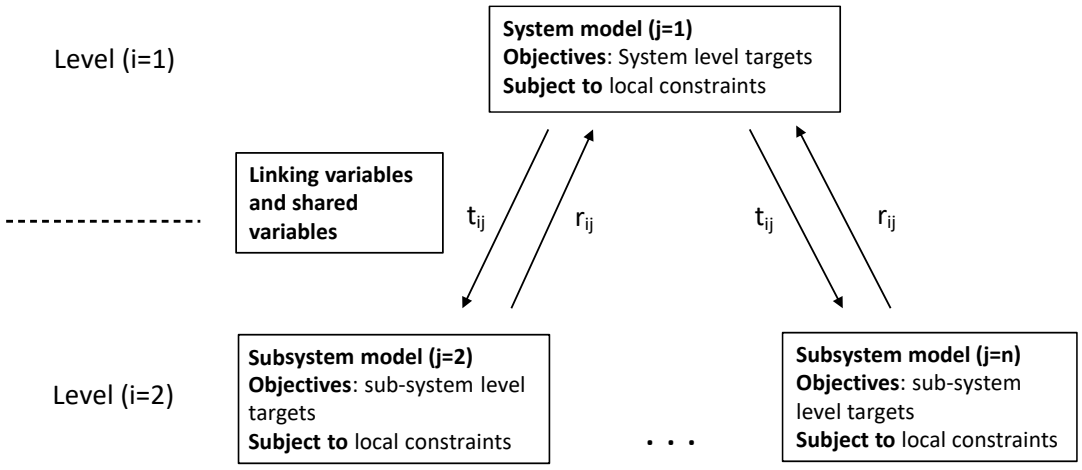

Fig. 2.6: *General hierarchical structure of ATC*

CHAPTER 3

Comparison of electromagnetic field calculations

In the design optimisation of electric vehicles, an electric motor model with reasonable accuracy and less computational complexity is required in the optimisation routine [72–75]. Chapter 4 presents a comparison study of four such models including the analytical motor model. In the literature, there are many analytical and semi-analytical modelling methods available. In order to select an appropriate method for this specific application, the performance differences associated with these methods should be well understood. Therefore, six modelling techniques are studied in this chapter [76]. The methods are based primarily on conformal mapping, mode matching, and harmonic modelling. In the case of conformal mapping, the slotted air gap of a complex machine geometry is transformed to a smooth slotless air gap where analytical expression for field solution is available. The solution in the canonical domain is then mapped back to the original slotted air gap domain. Mode matching or subdomain method is using the solution of Laplace's equation to model the slotted air gap. In harmonic modelling, the machine cross section is divided into homogeneous regions that are represented using Fourier series and coupled with each other using boundary conditions. The boundary value problems in both the mode matching and harmonic models are solved to obtain the field solutions. The performances of the modelling methods are evaluated by comparing the global parameters such as cogging torque, electromagnetic torque, back-emf, and the simulation time with the results of the finite element transient analysis.

3.1 Modelling techniques

A surface permanent magnet machine with twenty poles is considered as a test bench, and its parameters are given in Table 3.1. Analytical conformal mapping, semi-analytical conformal mapping, mode matching, and harmonic modelling are studied in detail. Carter factor, relative permeance, and complex permeance methods are included under the analytical conformal mapping. As a first step in calculating the global parameters

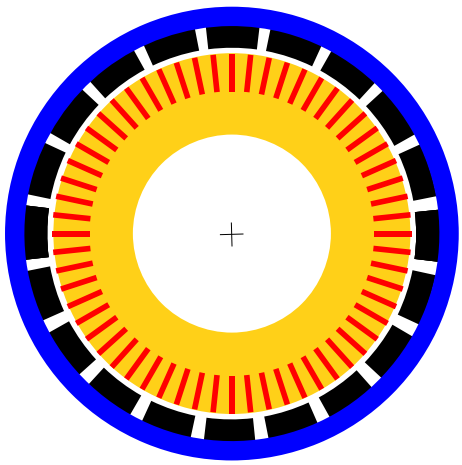

Fig. 3.1: *Symbolic outer rotor surface PM machine*

Table 3.1: *Outer rotor surface PM motor parameters*

Parameters	Symbol	Value	Unit
No. of poles	$2p$	20	-
No. of slots	Q_s	60	-
Magnet arc to pole pitch ratio	α_p	0.75	-
Rotor surface radius	R_r	80.2	mm
Magnet surface radius	R_m	76.2	mm
Stator outer radius	R_s	75	mm
Air-gap centre	r	75.6	mm
Magnet remanence	B_r	1.19	T
Core length	l_a	60	mm
Slot depth	d_s	12	mm
No. of conductors in a slot	N_c	6	-

including motor torque, back-emf, and losses, the air gap flux density is obtained. In this machine, the magnets are mounted on the rotor inner surface as in Fig. 3.1 and radially magnetised. The presence of slots in the stator reduces the flux density locally

near the slots which in turn reduces the total flux per pole. Hence it is important to include the slotting effect in the flux calculations. The slotless air-gap field solution is derived as defined by Zhu *et al.* in [32] and the Carter factor, relative permeance, and complex permeance methods account for the slotting effect in different ways.

Slotless air gap field solution

The air-gap region is divided into magnet (I) and air (II) as shown in Fig. 3.2, because the governing equations for the field solutions of these two regions are different.

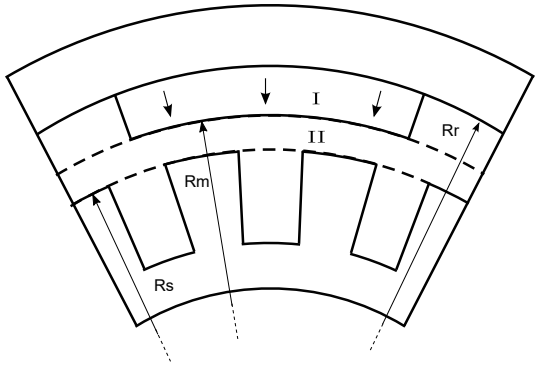

Fig. 3.2: *Cross section of outer rotor surface PM machine*

Inside the magnets, the field distribution has two components. First one is intrinsic flux density (B_{Ii}), due to the permanent orientation of grains caused by magnetisation, and the second one is (B_{Ih}) excitation component, due to its operating magnetic field intensity [77].

$$\vec{B_I} = \vec{B}_{Ii} + \vec{B}_{Ih} \tag{3.1}$$

So the relationship between the flux density $\vec{B_I}$ and the magnetic field intensity $\vec{H_I}$ in the magnet is

$$\vec{B_I} = \mu_0 \vec{M} + \mu_0 \mu_r \vec{H_I} \tag{3.2}$$

where $\vec{M}$ is the magnetisation vector, μ_r is the relative permeability of magnet, and μ_0 is the permeability of vacuum. The magnetisation is expressed in terms of remanent flux density in (3.3).

$$\vec{M} = \frac{\vec{B_r}}{\mu_0} \tag{3.3}$$

In the air, there is no intrinsic component, so (3.2) yields

$$\vec{B_{II}} = \mu_0 \vec{H_{II}} \tag{3.4}$$

Two fundamental postures (3.5) and (3.6) are valid for the magnetostatic fields in the

current free region as per Gauss's law of magnetism and Ampere's law respectively.

$$\nabla.\vec{B_{II}} = 0 \tag{3.5}$$

$$\nabla \times \vec{B_{II}} = 0 \tag{3.6}$$

Since the magnetic flux density has a zero curl, it can be expressed as the gradient of a scalar field.

$$\vec{B_{II}} = \mu_0 \vec{H_{II}} = -\mu_0 \nabla \varphi_{II} \tag{3.7}$$

Equation 3.7 is substituted into 3.6 to obtain the laplacian equation.

$$\nabla(\nabla\varphi_{II}) = \nabla^2\varphi_{II} = 0 \tag{3.8}$$

In the magnet, the scalar magnetic potential is calculated with a slightly different approach. The magnet body is replaced with an equivalent fictitious magnetisation volume charge.

$$\rho_m = -\nabla.(\mu_0\vec{M}) \tag{3.9}$$

The Maxwell's equation which relates the field $\vec{B}$ to its source, the magnetisation charge, is given by

$$\nabla.\vec{B_I} = \rho_m \tag{3.10}$$

By equating 3.9 and 3.10,

$$\nabla.\vec{B_I} = \nabla.(-\mu_0\mu_r\nabla\varphi_I) = -\nabla.(\mu_0\vec{M}) \tag{3.11}$$

Equation (3.11) yields Poison's equation,

$$\nabla^2\varphi_I = \frac{1}{\mu_r}\nabla.\vec{M} \tag{3.12}$$

In polar coordinates, the magnetisation $\vec{M}$ is defined as

$$\vec{M} = M_r\vec{r} + M_\theta\vec{\theta} \tag{3.13}$$

where,

$$M_r = \sum_{n=1,3,5,..}^{\infty} M_n cos(np\theta)$$

$$M_\theta = 0$$

where p is the number of pole pairs and n is the harmonic order. Figure 3.3 shows the direction of magnetisation vector which is always perpendicular to the magnet surfaces in radial magnetisation. Hence the tangential component of magnetisation vector is always zero Fig. 3.4. The harmonic components M_n are expressed as a function of B_r and α_p.

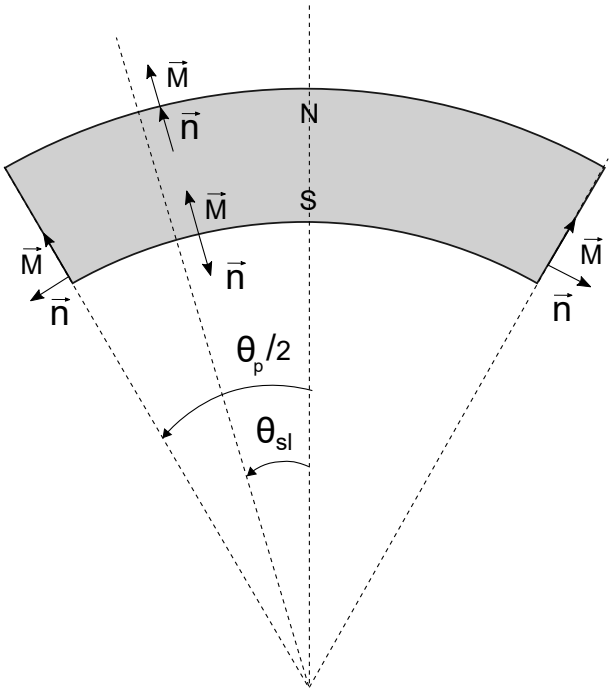

Fig. 3.3: *Direction of magnetisation: Radial*

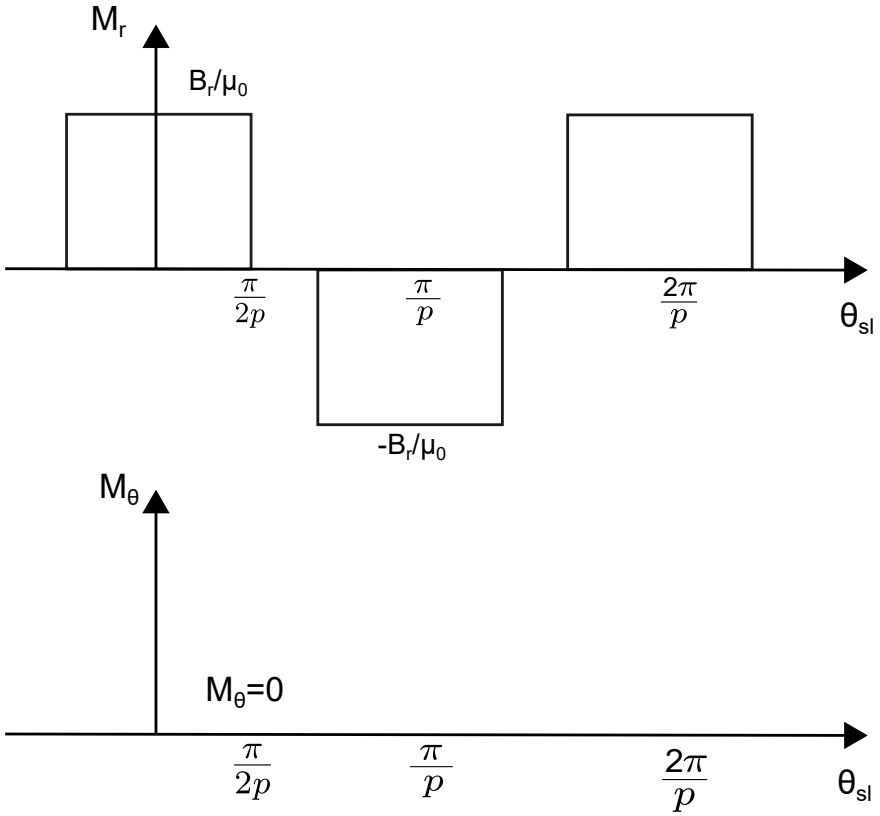

Fig. 3.4: *Radial magnetisation waveform*

$$M_n = \frac{B_r}{\mu_0}\frac{4}{n\pi}\sin\frac{n\pi\alpha_p}{2}$$

Laplace equation governing the air gap flux density 3.8 is given in the cylindrical coordinates as

$$\frac{\partial^2\varphi_{II}}{\partial r^2} + \frac{1}{r}\frac{\partial\varphi_{II}}{\partial r} + \frac{1}{r^2}\frac{\partial^2\varphi_{II}}{\partial\theta^2} = 0 \tag{3.14}$$

In the magnet, the flux density governed by Poisson's equation (3.12) is expressed in cylindrical coordinate as

$$\nabla\vec{M} = \frac{1}{r}M_r + \frac{\partial M_n}{\partial r} + \frac{1}{r}\frac{\partial M_\theta}{\partial\theta} = \sum_{n=1,3,5,..}^{\infty}\frac{1}{r}M_n cos(np\theta) \tag{3.15}$$

$$\frac{\partial^2\varphi_I}{\partial r^2} + \frac{1}{r}\frac{\partial\varphi_I}{\partial r} + \frac{1}{r^2}\frac{\partial^2\varphi_I}{\partial\theta^2} = \frac{1}{\mu_r}\sum_{n=1,3,5,..}^{\infty}\frac{1}{r}M_n cos(np\theta) \tag{3.16}$$

Since

$$H_I = -\nabla\varphi_I = -\frac{\partial\varphi_I}{\partial r}\vec{r} - \frac{1}{r}\frac{\partial\varphi_I}{\partial\theta}\vec{\theta} \tag{3.17}$$

The relation between the radial and tangential components of the field intensity $\vec{H}$ and the scalar magnetic potential is

$$H_{rI} = -\frac{\partial\varphi_I}{\partial r} \tag{3.18}$$

$$H_{\theta I} = -\frac{1}{r}\frac{\partial\varphi_I}{\partial\theta} \tag{3.19}$$

General Solutions in Polar Coordinates

The scalar magnetic potential in the air is a Laplacian problem, which can be solved by the separation of variables [78] method. Equation 3.14 can be broken up into the product of functions, each having only one variable. Hence the unknown scalar potential can be written in the form

$$\varphi(r,\theta) = R(r)F(\theta) \tag{3.20}$$

Substituting 3.20 in 3.14 and dividing it by RF/r^2,

$$\frac{r^2}{R}\frac{d^2R}{dr^2} + \frac{r}{R}\frac{dR}{dr} = -\frac{1}{F}\frac{d^2F}{d\theta^2} = \lambda^2 \tag{3.21}$$

where λ is the separation constant.

$$\frac{d^2F}{d\theta^2} + \lambda^2 F = 0 \tag{3.22}$$

$$r^2\frac{d^2R}{dr^2} + r\frac{dR}{dr} - \lambda^2 R = 0 \tag{3.23}$$

The general solution of 3.22 is

$$F(\theta) = C_1 cos(\lambda\theta) + C_2 sin(\lambda\theta) \tag{3.24}$$

Since the magnetic distribution is periodic even function, $F(\theta)$ should also be periodic. Thus $C_2 = 0$ and $\lambda = np$.

$$F(\theta) = C_1 cos(np\theta) \tag{3.25}$$

Equation 3.23, known as Cauchy-Euler equation, can be solved by making a substitution $r = e^u$ and reducing to an equation with constant coefficients.

$$R(r) = C_3 r^{np} + C_4 r^{-np}, n = 1, 2, 3, ... \tag{3.26}$$

Substitution of 3.26 and 3.25 yields

$$\varphi_I(r, \theta) = \sum_{n=1}^{\infty} (A_{nI} r^{np} + B_{nI} r^{-np}) cos(np\theta) \tag{3.27}$$

In the magnets, the general solution is the sum of homogeneous and particular equations. Therefore when $np \neq 1$,

$$\varphi_{II}(r, \theta) = \sum_{n=1}^{\infty} (A_{nII} r^{np} + B_{nII} r^{-np}) cos(np\theta) + \sum_{n=1,3,5,..}^{\infty} (\frac{M_n}{\mu_r[1 - (np)^2]}) r cos(np\theta) \tag{3.28}$$

and np=1

$$\varphi_{II}(r, \theta) = (A_{1II} r + B_{1II} r^{-1}) \cos(\theta) + \frac{M_1}{2\mu_r} r \ln r cos(\theta) \tag{3.29}$$

The boundary conditions for the external rotor motor are defined as,

$$\begin{aligned} H_{\theta I}(r, \theta)|_{r=R_s} &= 0 \\ H_{\theta II}(r, \theta)|_{r=R_r} &= 0 \\ B_{rI}(r, \theta)|_{r=R_m} &= B_{rII}(r, \theta)|_{r=R_m} \\ H_{\theta I}(r, \theta)|_{r=R_m} &= H_{\theta II}(r, \theta)|_{r=R_m} \end{aligned} \tag{3.30}$$

where R_m is radius of the magnet $(= R_s + g)$, R_r rotor radius $(= Rs + g + l_m)$, g is the air gap length, and l_m is and magnet thickness. The field components are calculated by solving the boundary value problem defined in the (3.27)-(3.30).

For external rotor motors $(np \neq 1)$

$$B_{slr}(r, \theta) = \sum_{n=1,3,5,..}^{\infty} -\frac{\mu_0 M_n}{\mu_r} \frac{np}{(np)^2 - 1} \left[\left(\frac{r}{R_m} \right)^{np-1} + \left(\frac{Rs}{R_m} \right)^{np-1} \left(\frac{Rs}{r} \right)^{np+1} \right] \left\{ \frac{(np-1) \left(\frac{Rm}{Rr} \right)^{2np} + 2 \left(\frac{Rm}{Rr} \right)^{np-1} - (np+1)}{\frac{\mu_r+1}{\mu_r} \left[1 - \left(\frac{Rs}{Rr} \right)^{2np} \right] - \frac{\mu_r-1}{\mu_r} \left[\left(\frac{Rs}{Rm} \right)^{2np} - \left(\frac{Rm}{Rr} \right)^{2np} \right]} \right\} \cos(np\theta) \tag{3.31}$$

$$B_{sl\theta}(r,\theta) = \sum_{n=1,3,5,..}^{\infty} -\frac{\mu_0 M_n}{\mu_r}\frac{np}{(np)^2-1}\left[\left(-\frac{r}{R_m}\right)^{np-1} + \left(\frac{Rs}{R_m}\right)^{np-1}\left(\frac{Rs}{r}\right)^{np+1}\right] \left\{\frac{(np-1)\left(\frac{Rm}{Rr}\right)^{2np} + 2\left(\frac{Rm}{Rr}\right)^{np-1} - (np+1)}{\frac{\mu_r+1}{\mu_r}\left[1-\left(\frac{Rs}{Rr}\right)^{2np}\right] - \frac{\mu_r-1}{\mu_r}\left[\left(\frac{Rs}{Rm}\right)^{2np} - \left(\frac{Rm}{Rr}\right)^{2np}\right]}\right\} \sin(np\theta) \quad (3.32)$$

For external rotor motors ($np = 1$)

$$B_{slr}(r,\theta) = \sum_{n=1,3,5,..}^{\infty} \frac{\mu_0 M_1}{2\mu_r}\left[1+\left(\frac{Rs}{r}\right)^2\right] \left\{\frac{np\left(\frac{Rm}{Rs}\right)^2 - np\left(\frac{Rr}{Rs}\right)^2 + \left(\frac{Rr}{Rs}\right)^2 \ln\left(\frac{Rm}{Rr}\right)^2}{\frac{\mu_r+1}{\mu_r}\left[1-\left(\frac{Rr}{Rs}\right)^2\right] - \frac{\mu_r-1}{\mu_r}\left[\left(\frac{Rm}{Rr}\right)^2 - \left(\frac{Rr}{Rm}\right)^2\right]}\right\} \cos(np\theta) \quad (3.33)$$

$$B_{sl\theta}(r,\theta) = \sum_{n=1,3,5,..}^{\infty} \frac{\mu_0 M_1}{2\mu_r}\left[-1+\left(\frac{Rs}{r}\right)^2\right] \left\{\frac{np\left(\frac{Rm}{Rs}\right)^2 - np\left(\frac{Rr}{Rs}\right)^2 + \left(\frac{Rr}{Rs}\right)^2 \ln\left(\frac{Rm}{Rr}\right)^2}{\frac{\mu_r+1}{\mu_r}\left[1-\left(\frac{Rr}{Rs}\right)^2\right] - \frac{\mu_r-1}{\mu_r}\left[\left(\frac{Rm}{Rr}\right)^2 - \left(\frac{Rr}{Rm}\right)^2\right]}\right\} \sin(np\theta) \quad (3.34)$$

3.1.1 Carter factor

Slotting reduces the flux in the air gap as well as distorts the magnetic field solution [32] locally. Carter factor accounts for the reduction of flux across the slot pitch due to increased reluctance near the slot region.

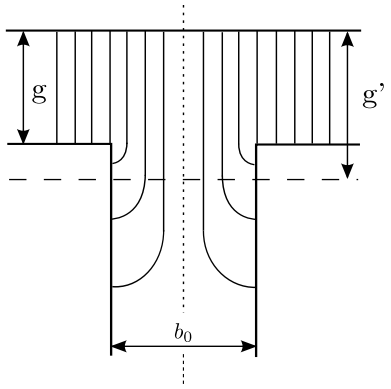

Fig. 3.5: *Carter factor model*

The slotted air-gap flux density can be calculated in the radial direction by multiplying the slotless radial field solution with Carter factor (k_c) or by substituting the effective

air-gap length (g') directly in (3.31) or (3.33).

$$\begin{aligned} B_s &= k_c B_{sl} \\ g' &= k_c g \end{aligned} \tag{3.35}$$

where,

$$k_c = \frac{\tau_s}{\tau_s - \frac{2b_0}{\pi}\left(\arctan\frac{b_o}{2g} - \frac{g}{b_o}\ln\left[1+\left(\frac{b_o}{2g}\right)^2\right]\right)}$$

3.1.2 Relative permeance model

The relative permeance $(\tilde{\lambda})$, which is modelled based on flux path length and modification factor (γ) [32] as in (3.36), is multiplied with the radial slotless field solution. The variation of the flux density in the radial direction is captured by correcting the modification factor (γ) that changes the flux path length as shown in Fig. 3.6. The influence of slotting on the tangential field solution of the air gap is neglected.

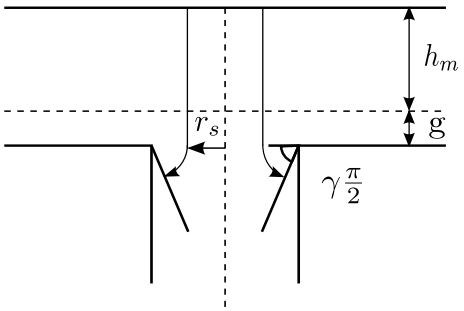

Fig. 3.6: *Relative permeance model*

Hence the relative permeance can be expressed as,

$$\tilde{\lambda} = \begin{cases} \frac{g+l_m/\mu_R}{g+l_m/\mu_R+\gamma\frac{\pi}{2}\left[\frac{b_0}{2}-r_s\right]}, & \text{for the slot region} \\ 1, & \text{for the tooth region} \end{cases} \tag{3.36}$$

where,

$$\gamma = \frac{g + l_m/\mu_R}{\pi b_0/4}\left(\frac{B_{max}}{B_{min}} - 1\right)$$

3.1.3 Complex relative permeance model

In the relative permeance model, the radial component of the field solution in the slotted air gap is estimated fairly well, but the tangential component, which is useful to derive the closed form solutions of the global parameters including cogging torque, is not included. The complex relative permeance model captures the influence of slotting

on both the radial and tangential components of the air-gap field. The field produced by the magnets in the slotted air gap of an unloaded machine (B_s) is computed from the slotless air gap field solution (B_k) and complex relative air gap permeance (λ). The complex relative permeance was introduced for an inner rotor machine using conformal mapping by Zarko et al. in. [45]. The flux density in the air gap is defined as a complex number by representing its radial and tangential components as the real and imaginary parts respectively.

$$\begin{aligned} B_s =& B_k\lambda^* = (B_{kr} + jB_{k\theta})(\lambda_a + j\lambda_b)^* \\ B_{sr} + jB_{s\theta} =& (B_{kr}\lambda_a + B_{k\theta}\lambda_b) + j(B_{k\theta}\lambda_a - B_{kr}\lambda_b) \end{aligned} \tag{3.37}$$

It can be observed that the radial component of the slotted air gap flux density is a function of both radial and tangential components of the slotless air gap field solution. The same is valid for the tangential component of the slotted air gap flux density.
The slotted air gap shape (S plane) shown in Fig. 3.8 is transformed into a slotless air gap (K plane) as in Fig. 3.13. Conformal transformation, a special kind of complex function that preserves the angle between intersecting curves at all points in the mapped complex variable planes, is employed as the perpendicularity between equipotential lines and flux lines should be preserved for magnetostatic calculations. Four different conformal mapping functions, as in Fig. 3.7, are used in the process of obtaining the slotless air gap as the canonical domain. The field solution in the slotless air gap is calculated using (3.31) to (3.34), and then is mapped back to the S plane. When the number of vertices in Z-plane is less than 4, the Schwarz-Christoffel transformation can be performed analytically [43]. For this purpose, the actual slot shape is replaced by an infinitely deep slot with parallel sides.

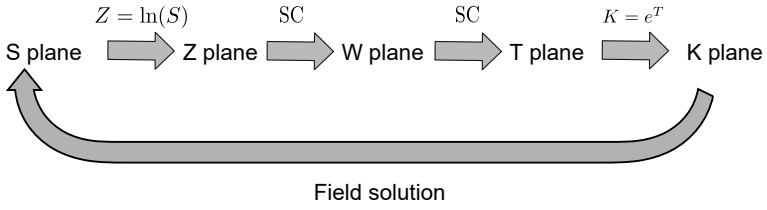

Fig. 3.7: *Steps involved in finding the field solution by converting the slotted air gap into a slotless air-gap domain*

Transformation from S plane to Z plane

The slot geometry in cylindrical coordinates is converted to Cartesian coordinates using a simple logarithmic conformal transformation [79]. As the relative permeance is periodic along the air gap path, a single slot is sufficient to be considered as in Fig. 3.8.

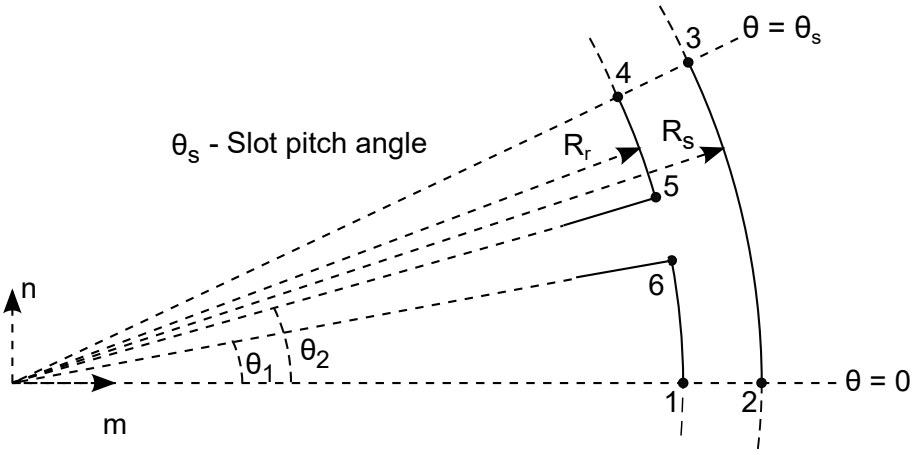

Fig. 3.8: *Single inifinitely deep slot opening in S-plane*

$$s = re^{j\theta} \tag{3.38}$$

The mapping function is

$$\begin{aligned} z &= \ln(s) \\ x + jy &= \ln(r) + j\theta \end{aligned} \tag{3.39}$$

The resulting Z-plane is shown in Fig. 3.9.

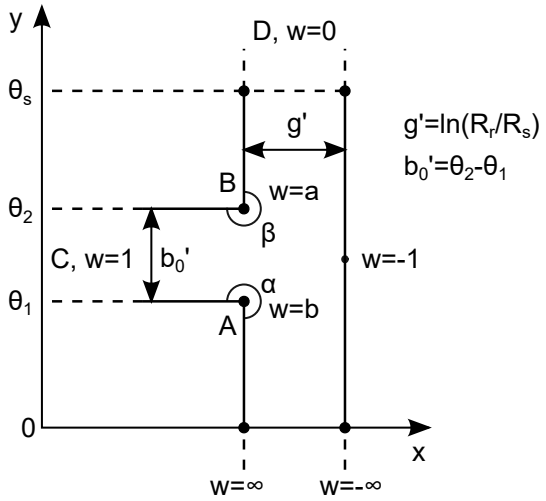

Fig. 3.9: *Slot opening in Z-plane*

Transformation from Z plane to W plane

Schwarz-Christoffel transformation [43] connects the real axis of W-plane with the boundaries of Z-plane polygon in such a way that the upper half of the W-plane forms

the interior of the polygon. Figure 3.10 shows the slot opening in the Z-plane with corresponding w-values.

In the differential equation (3.40), A is a scaling and rotational constant. a, b, c, and d are points on the real axis of the W-plane corresponding to the vertices of the polygon in the Z-plane. α, β, γ, and λ are the interior angles of the polygon.

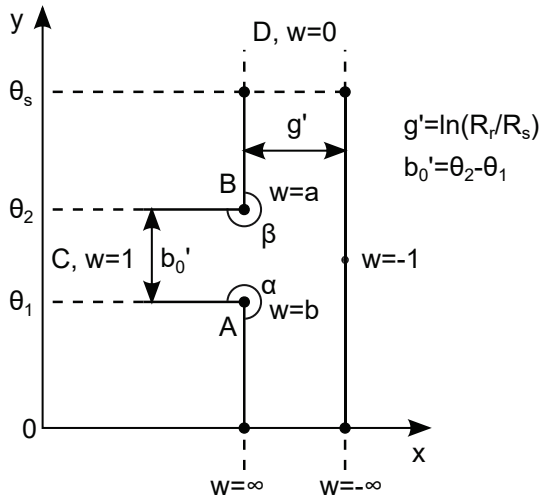

Fig. 3.10: *Slot opening in Z-plane with w-values*

$$\frac{dz}{dw} = A(w-a)^{\frac{\alpha}{\pi}-1}(w-b)^{\frac{\beta}{\pi}-1}(w-c)^{\frac{\gamma}{\pi}-1}(w-d)^{\frac{\delta}{\pi}-1} \tag{3.40}$$

Two of these four constants(a, b, c, and d) can be given convenient values because by fixing the values of two constants, the distance between the corresponding points in the Z-plane is defined and this can be given correct value by a suitable choice of A-value [43]. The remaining constants are calculated based on the polygon dimensions.

$$\frac{dz}{dw} = A\frac{(w-a)^{\frac{1}{2}}(w-b)^{\frac{1}{2}}}{(w-1)(w)} \tag{3.41}$$

The integrated value of equation (3.41) along any path in the W-plane will be equal to the corresponding value in the Z-plane.

$$z = \int A\frac{(w-a)^{\frac{1}{2}}(w-b)^{\frac{1}{2}}}{(w-1)(w)}dw \tag{3.42}$$

The value of A can be found by integrating (3.41) along the largest semi-circle in the W-plane and equating it to air gap length in the Z-plane.

$$w = Re^{j\theta} \tag{3.43}$$

The differential form of w is

$$dw = jRe^{j\theta}d\theta \tag{3.44}$$

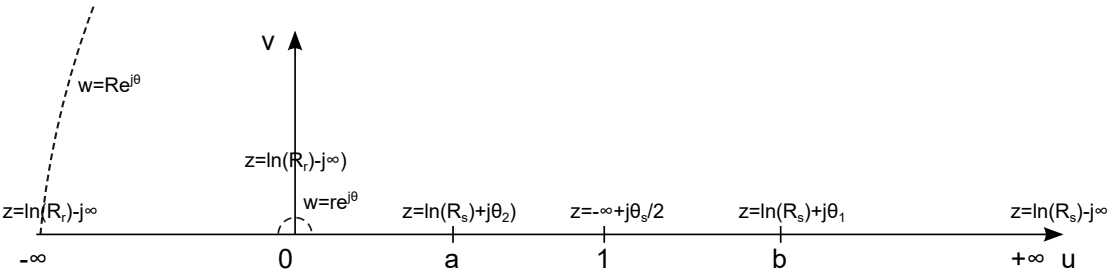

Fig. 3.11: *Slot opening in W-plane*

Substitution of 3.43 and 3.44 in 3.42 gives

$$z = \int_0^{\pi} \frac{A(Re^{j\theta} - a)^{\frac{1}{2}}(Re^{j\theta} - b)^{\frac{1}{2}}}{(Re^{j\theta} - 1)Re^{j\theta}} jRe^{j\theta}d\theta \tag{3.45}$$

As $R >> a, b$, and unity

$$z = \int_0^{\pi} \frac{A(Re^{j\theta}Re^{j\theta})^{\frac{1}{2}}}{Re^{j\theta}Re^{j\theta}} jRe^{j\theta}d\theta = \int_0^{\pi} jAd\theta = j\pi A \tag{3.46}$$

In the Z plane, $\int dz = g'$ and therefore

$$A = -j\frac{g'}{\pi} \tag{3.47}$$

The similar integral can be done along the smallest semi-circle in W-plane.

$$w = re^{j\theta} \tag{3.48}$$

The differential form of w is

$$dw = jre^{j\theta}d\theta \tag{3.49}$$

Substitution of 3.48 and 3.49 in 3.42 gives

$$z = \int_0^{\pi} \frac{A(re^{j\theta} - a)^{\frac{1}{2}}(re^{j\theta} - b)^{\frac{1}{2}}}{(r^{j\theta} - 1)re^{j\theta}} jre^{j\theta}d\theta \tag{3.50}$$

As $r << a, b$, and unity

$$z = \int_0^{\pi} \frac{A(ab)^{\frac{1}{2}}}{(-1)re^{j\theta}} jre^{j\theta}d\theta = \int_0^{\pi} -jA(ab)^{\frac{1}{2}}d\theta = j.j\frac{g'}{\pi}(ab)^{\frac{1}{2}}\pi = -g'(ab)^{\frac{1}{2}} \tag{3.51}$$

Since $\int dz = g'$,

$$(ab)^{\frac{1}{2}} = -1 \Rightarrow a = \frac{1}{b} \tag{3.52}$$

Substituting 3.47 in 3.42

$$z = -j\frac{g'}{\pi}\int \frac{(w - a)^{\frac{1}{2}}(w - b)^{\frac{1}{2}}}{(w - 1)(w)}dw \tag{3.53}$$

Equation 3.53 is integrated by substitution method

$$p^2 = \frac{w-a}{w-b} \tag{3.54}$$

which can be converted as

$$w = \frac{bp^2 - a}{p^2 - 1} \tag{3.55}$$

and differentiated as

$$dw = -\frac{2p(b-a)}{(p^2-1)^2}dp \tag{3.56}$$

then 3.53 becomes

$$z = -j\frac{2g'}{\pi}\int \frac{(a+1)^2(a-1)p^2}{(1-p^2)(a^2-p^2)(p^2+a)}dp \tag{3.57}$$

After splitting the integrand into partial fractions,

$$z = -j\frac{2g'}{\pi}\int \left(\frac{1}{1-p^2} - \frac{a}{a^2-p^2} - \frac{a-1}{a+p^2}\right)dp \tag{3.58}$$

The solution of integral is

$$z = -j\frac{g'}{\pi}\left[\ln\left|\frac{1+p}{1-p}\right| - \ln\left|\frac{a+p}{a-p}\right| - \frac{2(a-1)}{\sqrt{a}}\tan^{-1}\frac{p}{\sqrt{a}}\right] + C_1 \tag{3.59}$$

The integration constant and a can be calculated using the values of z at the points A and B.

It can be noted that when $w \to a$, $p = 0$ and $z = \ln(R_s) + j\theta_2$

$$z = -j\frac{g'}{\pi}\left[\ln(1) - \ln(1) - \frac{2(a-1)}{\sqrt{a}}\tan^{-1}0\right] + C_1 = C_1$$

$$C_1 = \ln(R_s) + j\theta_2 \tag{3.60}$$

Similarly when $w \to b$, $p = \infty$ and $z = \ln(R_s) + j\theta_1$

$$z = -j\frac{g'}{\pi}\left[\ln(-1) - \ln(-1) - \frac{2(a-1)}{\sqrt{a}}\tan^{-1}\infty\right] + \ln(R_s) + j\theta_2 \tag{3.61}$$

$$\ln(R_s) + j\theta_1 = j\frac{g'}{\pi}\frac{2(a-1)}{\sqrt{a}}\frac{\pi}{2} + \ln(R_s) + j\theta_2 \tag{3.62}$$

$$g'\frac{(a-1)}{\sqrt{a}} = -(\theta_2 - \theta_1) = -b_0' \tag{3.63}$$

In equation 3.63, the only unknown variable is b that can be written as

$$a = \left[-\frac{b_0'}{2g'} + \sqrt{\left(\frac{b_0'}{2g'}\right)^2 + 1}\right]^2 \tag{3.64}$$

Transformation from T plane to W plane

In order to transform the T-plane shown in Fig. 3.12 into W-plane, Schwarz-Christoffel method is used again. The vertice E in T-plane is assigned as the origin of W-plane, the area in between the plates will occupy the upper half of the W-plane. It is observed that the points numbered 1 to 2 don't have the same angular coordinates $\theta = 0$ and the same is valid for the points 3 and 4 which no longer have the angular coordinates $\theta = \theta_s$.
The Schwarz-Christoffel differential equation governing the mapping between the T-plane and the W-plane is

$$\frac{dt}{dw} = A_1(w-e)^{\frac{\alpha_1}{\pi}-1} \tag{3.65}$$

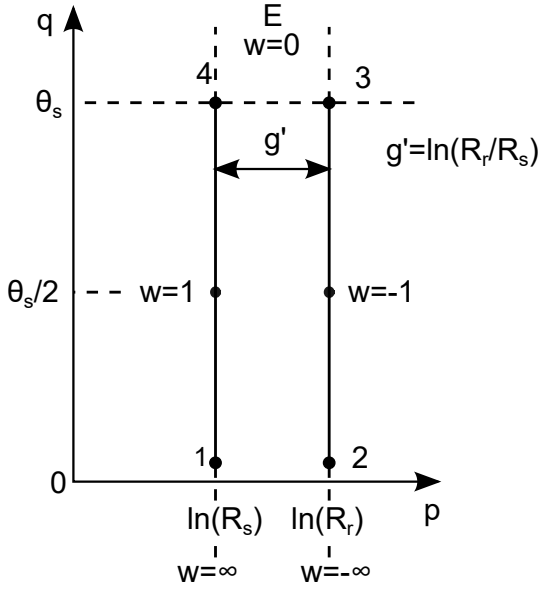

Fig. 3.12: *Slot opening in T-plane*

If the parallel plates are opened at the corner where $w = 0$, the (3.65) becomes

$$dt = \frac{A_1}{w}dw \tag{3.66}$$

After integration

$$t = A_1 \ln w + B_1 \tag{3.67}$$

The constants A_1 and B_1 can be found using the points where $w = 1$ and $w = -1$. The corresponding values for t are derived from the Fig. 3.12.
when $w = -1$

$$\ln(R_r) + j\frac{\theta_s}{2} = A_1 \ln(-1) + B_1 = j\pi A_1 + B_1 \tag{3.68}$$

and when $w = 1$

$$\ln(R_s) + j\frac{\theta_s}{2} = A_1 \ln(1) + B_1 = B_1 \tag{3.69}$$

Equations 3.68 and 3.69 can be solved to get,

$$A_1 = \frac{1}{j\pi} ln(\frac{R_r}{R_s}) = -j\frac{g'}{\pi} \tag{3.70}$$

$$B_1 = ln(R_r) + j\frac{\theta_s}{2} \tag{3.71}$$

So the transformation equation 3.67 becomes

$$t = -j\frac{g'}{\pi} \ln w + \ln(R_s) + j\frac{\theta_s}{2} \tag{3.72}$$

Transformation from T plane to K plane

The exponential mapping function converts the two parallel plates in T-plane to a circular shape in K-plane. The resulting slotless air gap profile of a single slot is shown in Fig. 3.12.

$$k = e^t \tag{3.73}$$

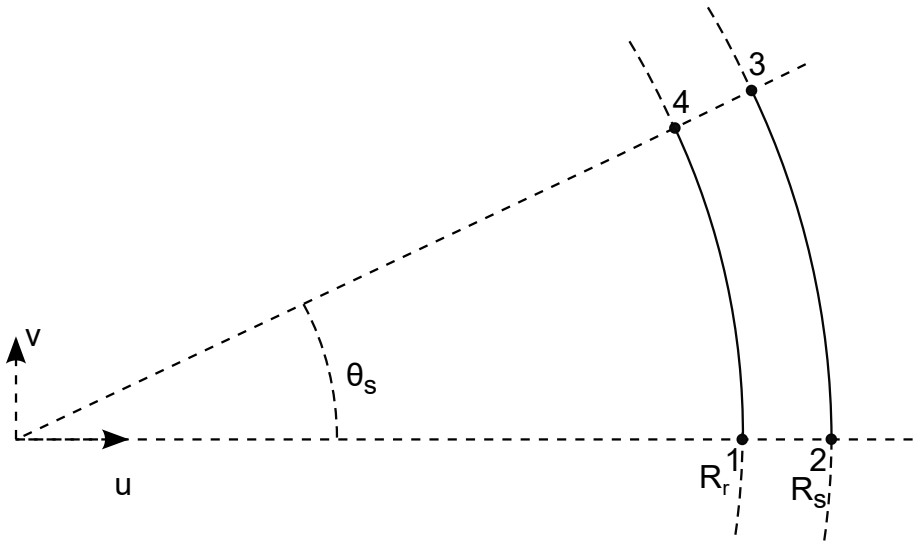

Fig. 3.13: *Slot opening in K-plane*

Thus the slotted air gap is transformed into a slotless geometry where the equations from Section 3.1 can be used to calculate the field solution. As the conformal mapping is reversible, the solution in K-plane can be mapped to S-plane as explained below.

Field solution in S-plane

The scalar potential function in S and K planes are expressed as complex numbers, where the real and imaginary parts denote radial and tangential components respectively. An analytical complex function that converts the scalar potential from S-plane

to K-plane also satisfies the Cauchy-Riemann conditions.

$$\begin{aligned}\frac{\partial u}{\partial m} &= \frac{\partial v}{\partial n} \\ \frac{\partial v}{\partial m} &= -\frac{\partial u}{\partial n}\end{aligned} \tag{3.74}$$

The complex number $\varphi(m,n)$ is the scalar potential function in the S plane and $\psi(u,v)$ is the transformed scalar potential function in the K plane.

$$\begin{aligned}\varphi(m,n) &= m + jn \\ \psi(u,v) &= u(m,n) + jv(m,n)\end{aligned} \tag{3.75}$$

The field intensity is divergence of scalar potential $H = -\nabla\varphi$, so in the S plane

$$H_s = H_m + jH_n = -\frac{\partial \varphi}{\partial m} - j\frac{\partial \varphi}{\partial n} \tag{3.76}$$

and in the K-plane

$$H_k = H_u + jH_v = -\frac{\partial \psi}{\partial u} - j\frac{\partial \psi}{\partial v} \tag{3.77}$$

Taking partial differential of scalar potential in S-plane,

$$\begin{aligned}\frac{\partial \varphi}{\partial m} &= \frac{\partial \psi}{\partial u}\frac{\partial u}{\partial m} + \frac{\partial \psi}{\partial v}\frac{\partial v}{\partial m} \\ \frac{\partial \varphi}{\partial n} &= \frac{\partial \psi}{\partial u}\frac{\partial u}{\partial n} + \frac{\partial \psi}{\partial v}\frac{\partial v}{\partial n}\end{aligned} \tag{3.78}$$

By combining 3.76, 3.77, and 3.78,

$$H_s = H_u\frac{\partial u}{\partial m} + H_v\frac{\partial v}{\partial m} + j\left(H_u\frac{\partial u}{\partial n} + H_v\frac{\partial v}{\partial n}\right) \tag{3.79}$$

After applying Cauchy-Riemann conditions,

$$H_s = (H_u + jH_v)\left(\frac{\partial u}{\partial m} - j\frac{\partial v}{\partial m}\right) = H_k\left(\frac{\partial u}{\partial m} - j\frac{\partial v}{\partial m}\right) \tag{3.80}$$

Since $k = u(m,n) + jv(m,n) = k(s(m,n))$, then

$$\frac{\partial k}{\partial m} = \frac{\partial u}{\partial m} + j\frac{\partial v}{\partial m} = \frac{\partial k}{\partial s}\frac{\partial s}{\partial m} = \frac{\partial k}{\partial s} \tag{3.81}$$

Complex conjugate of $\frac{\partial k}{\partial s}$ will be

$$\left(\frac{\partial k}{\partial s}\right)^* = \frac{\partial u}{\partial m} - \frac{\partial v}{\partial m} \tag{3.82}$$

If 3.82 is substituted into 3.80,

$$H_s = H_k\left(\frac{\partial k}{\partial s}\right)^* \tag{3.83}$$

The same equation is valid for the flux density also

$$B_s = B_k \left(\frac{\partial k}{\partial s}\right)^* \tag{3.84}$$

The partial derivative $\frac{\partial k}{\partial s}$ is expressed as

$$\frac{\partial k}{\partial s} = \frac{\partial k}{\partial t}\frac{\partial t}{\partial w}\frac{\partial w}{\partial z}\frac{\partial z}{\partial s} \tag{3.85}$$

Each partial derivatives in 3.85 is defined by conformal transformation

$$\begin{aligned}
\frac{\partial k}{\partial t} &= e^t = e^{\ln k} = k \\
\frac{\partial t}{\partial w} &= -j\frac{g'}{\pi}\frac{1}{w} \\
\frac{\partial w}{\partial z} &= j\frac{\pi}{g'}\frac{(w-1)w}{(w-a)^{\frac{1}{2}}(w-b)^{\frac{1}{2}}} \\
\frac{\partial z}{\partial s} &= \frac{1}{s}
\end{aligned} \tag{3.86}$$

Substituting 3.86 into 3.84

$$B_s = B_k \left[\frac{k}{s}\frac{(w-1)}{(w-a)^{\frac{1}{2}}(w-b)^{\frac{1}{2}}}\right] \tag{3.87}$$

As B_s is the flux density in the slotted air gap and B_k is for the slotless air gap, the remaining term in 3.87 is defined as complex relative permeance.

$$\lambda = \lambda_a + j\lambda_b = \frac{k}{s}\frac{(w-1)}{(w-a)^{\frac{1}{2}}(w-b)^{\frac{1}{2}}} \tag{3.88}$$

The radial and tangential components of λ are given in Fourier form as,

$$\begin{aligned}
\lambda_a &= \lambda_0 + \sum_{n=1}^{N_\lambda} \lambda_{an}(r,\theta)\cos(nQ_s\theta) \\
\lambda_b &= \sum_{n=1}^{N_\lambda} \lambda_{bn}(r,\theta)\sin(nQ_s\theta)
\end{aligned} \tag{3.89}$$

In the equation (3.88), s-represents the known coordinates in S-plane. The constants a and b have been defined in (3.52), (3.64). The term k is also a function of w, so λ can be considered as a non-linear function of w. The values of w are obtained by solving (3.90) using Levenberg-Marquardt optimisation algorithm [80]. The residual norm for the optimisation problem is

$$||F|| = [Re(z - z(w))]^2 + [Im(z - z(w))]^2 \tag{3.90}$$

where z represents the coordinates in the Z plane. The values of $z(w)$ are matched with z by choosing the appropriate w values that satisfy the solution of (3.42). Thus, the slotted air gap permanent magnet field solution is calculated for the reference outer rotor machine using (3.87).

3.1.4 Semi-analytical conformal mapping

In the analytical conformal mapping methods, the field solution in the air gap of the slotless geometry is calculated along the arc of a circle which is assumed to be also the circular arc in the middle of the air gap in the slotted geometry. However, during conformal transformation the circular arc in the slotted air gap of the S plane becomes distorted in the K plane as shown in Fig. 3.14 on the right-hand image. In addition, the same image shows that magnet shape having straight edges in the S plane also becomes distorted in the K plane, so equations (3.31) to (3.34) that assume the magnet shape and evaluation points as shown in Fig. 3.14 (left-hand image) cannot be used for accurate computation of the field solution in the canonical domain. The main reason for making such simplifications in the K plane and sacrificing the accuracy of the field solution is the possibility to derive closed form solutions for back-EMF, cogging torque and electromagnetic torque waveforms as explained in detail in [45], [81], [82].

The solution for taking into account the distortion of the evaluation points and magnet edges in the K plane is to utilise the SC Toolbox available in MATLAB to numerically map the original slotted air gap to a rectangular domain and then use the Hague's equation [42] to obtain the field solution. The SC Toolbox and Hague's field solution were first combined in [83, 84].

The permanent magnet is replaced with equivalent surface currents [34,85] and mapped to the rectangular domain. Thus the distortion of magnet edges and air gap evaluations points can be captured in the calculation.

The first transformation for converting the original curved motor geometry section to the Z plane is performed using logarithmic function. The coordinates of the stator coils and permanent magnet currents in the S plane are also transformed to the Z plane as given in Fig. 3.16. The slot ampere-turns are modelled using four equidistant point currents located along the centreline of the slot opening.

This geometry is simplified to a single periodic slot profile shown in Fig. 3.17 to reduce the calculation effort involved in the numerical Schwarz-Christoffel transformation without causing any inaccuracy. This is an improvement with respect to previously presented solutions for surface PM motors which combine SC Toolbox, Hague's equations and modelling of magnets with surface currents [85, 86]. The authors of those papers transformed multiple slot pitches within one repeating pattern of the magnetic

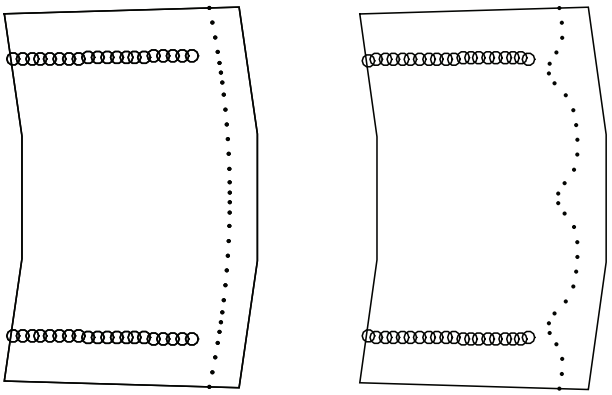

Fig. 3.14: *Distortion of evaluation points (dots) in the K plane (right-hand image) located along the circular arc in the S plane and distortion of permanent magnet edges (circles) resulting from conformal mapping. The left-hand image shows assumed evaluation points and magnet edges in the K plane*

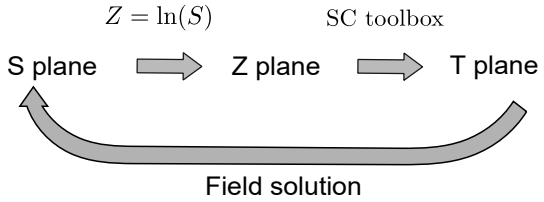

Fig. 3.15: *Steps involved in finding the field solution by converting the slotted air gap into a rectangular canonical domain*

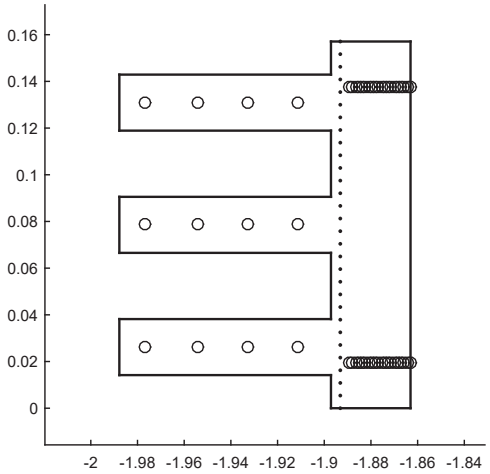

Fig. 3.16: *Pole pitch of the air-gap geometry in Z plane*

field distribution. Multiple slot pitches increase the number of vertices of the polygon that needs to be transformed into the canonical domain and thus significantly increase the time needed to perform the numerical SC transformation. In the case of surface PM motors, only one referent slot pitch can be transformed for all rotor positions to capture

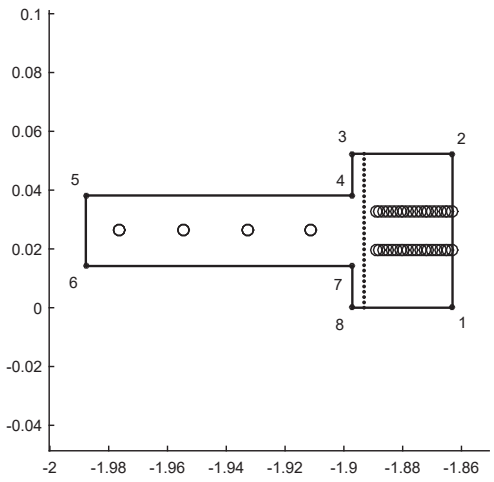

Fig. 3.17: *Transformed slot pitch of the air-gap geometry in Z plane*

the basic repetitive geometric pattern that occurs in the air gap.
A single slot pitch in the Z plane can be extracted using equations

$$z_{singleslot} = rem(imag(z), slotpitch) \tag{3.91}$$

$$z_{quotient} = floor(imag(z)/slotpitch) \tag{3.92}$$

written in the MATLAB syntax where $z_{singleslot}$ is the single periodic slot geometry in the Z plane, $z_{quotient}$ is the slot number counting from the reference position at $y = 0$, and $slotpitch$ is the angular span of one slot pitch in radians. The single slot polygon is created in the SC Toolbox using $polygon$ command by defining corner points in the counter-clockwise direction as a complex vector v [34] as shown in Fig. 3.17 and (3.93).

$$pp = polygon(v) \tag{3.93}$$

The next step is to map the polygon to a rectangle in the W plane as shown in Fig. 3.18 using MATLAB command

$$f = crrectmap(pp, alpha) \tag{3.94}$$

where $alpha$ is the single row vector which specifies the numbers of the vertices that form the corners of the rectangle in the W plane (canonical domain), in this case, 1, 2, 3 and 8. The coordinates of the air gap centre points (dotted lines in Fig. 3.18), armature currents and magnet currents in the W plane are computed as

$$w_{singleslot} = evalinv(f, z_{singleslot}) \tag{3.95}$$

where $z_{singleslot}$ is the complex vector of point coordinates.

The dimensions of the rectangular geometry in the canonical domain are given by

$$\Delta u = \frac{Qs}{p}(real[w(2)] - real[w(1)]), \tag{3.96}$$

$$\Delta v = imag[w(8)] - imag[w(1)]. \tag{3.97}$$

The complete pole pitch in the W plane, shown in Fig. 3.19, can be obtained by developing the solution from a single slot using the formulation

$$w = w_{singleslot} + z_{quotient}\Delta u. \tag{3.98}$$

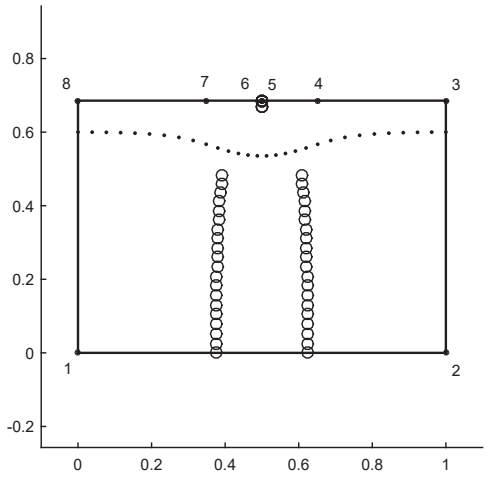

Fig. 3.18: *Transformed slot pitch of the air-gap geometry in W plane*

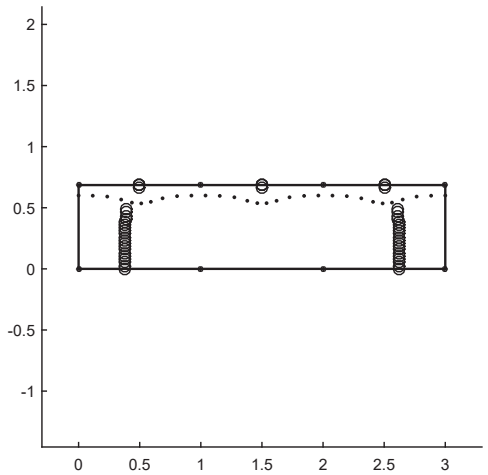

Fig. 3.19: *Pole pitch of the air-gap geometry in W plane*

Now, in the rectangular canonical domain the field solution is calculated along the line in the air gap centre by taking partial derivatives in the radial and tangential directions of magnetic potential Ω given by Hague's equation

$$\Omega = \frac{\mu_0 I}{2\pi} \sum_{k=-\infty}^{k=+\infty} (-1)^k \left(\arctan \left[\frac{\tan\left(\frac{\pi}{2\Delta v}(v+v_I)\right)}{\tanh\left(\frac{\pi}{2\Delta v}\left(u-k\Delta u-u_I\right)\right)} \right] + \arctan \left[\frac{\tan\left(\frac{\pi}{2\Delta v}(v-v_I)\right)}{\tanh\left(\frac{\pi}{2\Delta v}\left(u-k\Delta u-u_I\right)\right)} \right] \right) \tag{3.99}$$

where u_I and v_I are the coordinates of the point currents. The flux density in the W plane is given by

$$B_u = \frac{\partial \Omega}{\partial u} \tag{3.100}$$

$$B_v = \frac{\partial \Omega}{\partial v} \tag{3.101}$$

$$B_w = B_u + jB_v \tag{3.102}$$

$$B_u = -\frac{\mu_0 I}{4\Delta v} \sum_{k=-\infty}^{+\infty} (-1)^k \operatorname{csch}\left[\frac{\pi(-\Delta u k + u - u_I)}{2\Delta v}\right] \left(-\frac{\tan\left[\frac{\pi(v-v_I)}{2\Delta v}\right]}{1+\coth\left[\frac{\pi(u-k\Delta u-u_I)}{2\Delta v}\right]^2 \tan\left[\frac{\pi(v-v_I)}{2\Delta v}\right]^2} - \frac{\tan\left[\frac{\pi(v+v_I)}{2\Delta v}\right]}{1+\coth\left[\frac{\pi(u-k\Delta u-u_I)}{2\Delta v}\right]^2 \tan\left[\frac{\pi(v+v_I)}{2\Delta v}\right]^2} \right) \tag{3.103}$$

$$B_v = -\frac{\mu_0 I}{4\Delta v} \sum_{k=-\infty}^{+\infty} (-1)^k \coth\left[\frac{\pi(-\Delta u k + u - u_I)}{2\Delta v}\right] \left(\frac{2\sinh\left[\frac{\pi(\Delta u k - u + u_I)}{2\Delta v}\right]^2}{+\cosh\left[\frac{\pi(k\Delta u - u + u_I)}{\Delta v}\right] - \cos\left[\frac{\pi(v-v_I)}{\Delta v}\right]} + \frac{\sec\left[\frac{\pi(v+v_I)}{2\Delta v}\right]^2}{1+\coth\left[\frac{\pi(u-k\Delta u-u_I)}{2\Delta v}\right]^2 \tan\left[\frac{\pi(v+v_I)}{2\Delta v}\right]^2} \right) \tag{3.104}$$

The field solution in the original slotted air gap can be calculated by introducing the complex relative air gap permeance term similar to the analytical method.

$$B_s = B_m + jB_n = B_w \left(\frac{\partial w}{\partial s}\right)^* = B_w \left(\frac{\partial w}{\partial z}\frac{\partial z}{\partial s}\right)^* \tag{3.105}$$

where

$$\frac{\partial w}{\partial z} = evaldiff(f, w),$$
$$\frac{\partial z}{\partial s} = \frac{1}{R_g e^{j\theta}}.$$

The radius R_g equals

$$R_g = R_s + \frac{g}{2}. \tag{3.106}$$

The solution in (3.105) gives the field B_s in Cartesian coordinates, which are converted to cylindrical coordinates using

$$B_r = B_m \cos\theta + B_n \sin\theta$$
$$B_\theta = -B_m \sin\theta + B_n \cos\theta \tag{3.107}$$

The influence of magnet and air-gap evaluation points' distortion are evaluated separately in [87]. It was shown that the negligence of magnet shape distortions has greater influence on cogging torque shape and magnitude while neglecting the distortion of evaluation points mostly affects the average total torque.

3.1.5 Mode matching technique (MM)

This method divides the machine geometry into rectangular homogeneous regions ($\mu = \text{constant}$) and obtains the electromagnetic field solution by solving the Laplace's or Poisson's equations and imposing a set of boundary conditions [35, 74].

$$\nabla^2 A = -\mu_0(\nabla \vec{M}_0) - \mu \vec{J} \tag{3.108}$$

For the analysis performed in this study, the distribution of the magnetic field solution is computed at no load, so the $\vec{J}$ component will disappear. In addition, the number of magnets with negative and positive orientations within a pole pair is the same. Therefore, in Fourier expansion, the zero frequency component is not present. After all these simplifications, the equation for magnetic vector potential on a plane is

$$A_z = \sum_{n=1}^{\infty} \left[A_{zsn} \sin(\omega_n \xi) + A_{zcn} \cos(\omega_n \xi)\right] \tag{3.109}$$

This generic solution is applicable for different types of coordinate systems [35]. The components A_{zs} and A_{zc} are written for polar coordinate system as,

$$A_{zsn}(r) = -\frac{1}{\omega_n}\left(c_n r^{\omega_n} + d_n r^{-\omega_n} - rG_{rcn}\right) \tag{3.110}$$

$$A_{zcn}(r) = -\frac{1}{\omega_n}\left(a_n r^{\omega_n} + b_n r^{-\omega_n} - rG_{rsn}\right) \tag{3.111}$$

Similarly, the magnetic flux density can be written as

$$B_r = \sum_{n=1}^{\infty}(B_{rsn}(r)\sin(\omega_n\theta) + B_{rcn}(r)\cos(\omega_n\theta)) \tag{3.112}$$

$$B_\theta = \sum_{n=1}^{\infty}(B_{\theta sn}(\theta)\sin(\omega_n\theta) + B_{\theta cn}(r)\cos(\omega_n\theta)) \tag{3.113}$$

and

$$B_{rsn} = a_n r^{\omega_n - 1} + b_n r^{-\omega_n - 1} + G_{rsn} \tag{3.114}$$

$$B_{rcn} = -c_n r^{\omega_n - 1} - d_n r^{-\omega_n - 1} + G_{rcn} \tag{3.115}$$

$$B_{\theta sn} = c_n r^{\omega_n - 1} - d_n r^{-\omega_n - 1} + G_{\theta sn} \tag{3.116}$$

$$B_{\theta cn} = a_n r^{\omega_n - 1} - b_n r^{-\omega_n - 1} + G_{\theta cn} \tag{3.117}$$

where a_n, b_n, c_n and d_n are the unknowns which have to be solved, G_{rcn}, G_{rsn}, $G_{\theta cn}$ and $G_{\theta sn}$ are the source terms given by the following expressions

$$G_{rsn} = \mu_0\omega_n\frac{\omega_n M_{rs} - M_{\theta c}}{\omega_n^2 - 1} \tag{3.118}$$

$$G_{rcn} = \mu_0\omega_n\frac{\omega_n M_{rc} + M_{\theta s}}{\omega_n^2 - 1} \tag{3.119}$$

$$G_{\theta sn} = -\mu_0\frac{\omega_n M_{rc} + M_{\theta s}}{\omega_n^2 - 1} \tag{3.120}$$

$$G_{\theta cn} = \mu_0\frac{\omega_n M_{rs} - M_{\theta c}}{\omega_n^2 - 1} \tag{3.121}$$

where M_θ and M_r are the magnetisation in θ and r directions. When two regions are to be coupled, for instance the region with permanent magnets and the region with air gap, the following continuous boundary conditions have to be respected at their interface:

$$B_{ra} = B_{rb}|_{r=h_a} \tag{3.122}$$

$$H_{\theta a} = H_{\theta b}|_{r=h_a} \tag{3.123}$$

Considering the constitutive relation

$$\vec{B} = \mu_0\mu_r\vec{H} + \mu_0\vec{M}_0 \tag{3.124}$$

the boundary conditions can be expressed in terms of either $\vec{B}$ or $\vec{H}$.
The influence of slotting in the air-gap field is quantified by adding slots c_k to the air gap as shown in Fig. 3.20.

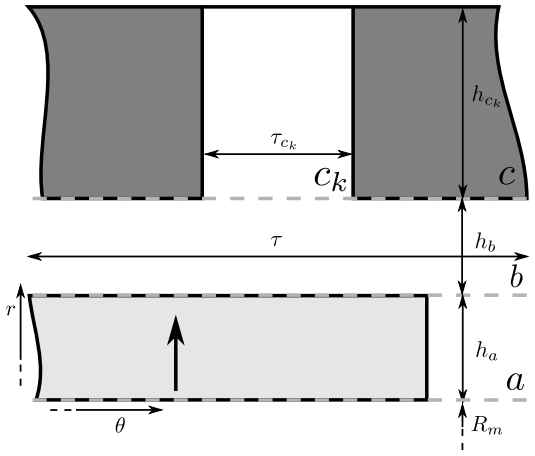

Fig. 3.20: *Mode matching technique*

There are several considerations to take into account while adding slot regions to the air gap. First of all, the regions a and b have the same length in θ direction, therefore the coefficients from equations (3.114) to (3.117) can be solved using the boundary conditions from (3.122) and (3.123). In addition, a special boundary condition between the slot and the air gap should be considered, and the same can be expressed for the no load analysis as [35]

$$B_{rc_k} = B_{rb}|_{r=ha+h_b, \quad \theta_{c_k} \leq \theta \leq \tau_{c_k}} \tag{3.125}$$

$$H_{\theta b} = \begin{cases} \sum_{k=1}^{K} H_{\theta_{c_k}}|_{r=ha+h_b, \quad \theta_{c_k} \leq \theta \leq \tau_{c_k}} \\ 0, \quad \text{else} \end{cases} \tag{3.126}$$

Moreover, considering the field solution in the region c_k is not periodic and the boundary condition that Fourier basis can take is periodic as well as pinned (zero or peak on the boundaries) [88], it is convenient to force H_r to zero and $B_\theta = |\vec{B}|$ at the boundary between lateral side of tooth and slot. These boundary conditions assign infinite permeability to the tooth region. The same boundary conditions, with $H_\theta = 0$, are applicable for the slot base interface with the stator iron and the magnet base interface with the rotor iron.
The regions with different lengths (τ and τ_{c_k}) have to be coupled to the final system of linear equations. It should be noted that the difference in domain lengths produces different spatial frequencies $\omega_i = 2\pi/\tau_i$, so the continuous boundary conditions in (3.122) and (3.123) cannot be written directly. In order to employ the boundary conditions, the

solution has to be expanded from the basis with frequencies ω into the basis of frequencies ω_{c_k} or vice versa. Therefore, the radial flux density between the regions can be equated as given in.

$$\sum_{m=1}^{\infty} B_{rscm} \sin\left(\omega_{c_k}\theta_{c_k}\right) = \sum_{n=1}^{\infty} \left(B_{rsbn} \sin(\omega_b\theta) + B_{rcbn} \cos(\omega_b\theta)\right) \tag{3.127}$$

By writing the equation in the same spacial frequencies (matching the modes),

$$B_{rscm} = \sum_{n=1}^{\infty} \left(B_{rsbn}\varepsilon_s + B_{rcbn}\varepsilon_c\right) \tag{3.128}$$

The cosine component of the magnetic flux density of the slot region c_k is zeroed because of Neuman boundary conditions along r axis. The considered regions are in the air and they are source free, so the constitutive relation (3.125) can be simplified as,

$$B_{\theta sbn} = \sum_{k=1}^{K} \sum_{m=1}^{\infty} B_{\theta cc_k}\kappa_c \tag{3.129}$$

$$B_{\theta cbn} = \sum_{k=1}^{K} \sum_{m=1}^{\infty} B_{\theta cc_k}\varsigma_c \tag{3.130}$$

where K is the number of slots within a pole pair, ε_s, ε_c, κ_c and ς_c are the constants resulting from matching the modes. The detailed description of the method can be found in [35]. The boundary value problem with the conditions defined in (3.127), (3.129), and (3.130) can be solved for the field solutions [35, 39, 40].

3.1.6 Harmonic modelling (HM)

The analytical solution obtained from MM technique is valid only for the homogeneous regions. Therefore, the slotted structure is modelled by matching the modes of different homogeneous regions. This feature allows to define the geometric shape analytically and gives a high level of convergence. On the other hand, for complex geometries, it is hard to derive the analytical expressions. HM gives a unique possibility to model the slotted structures using Fourier series. This method enables the calculation of the field in the tooth region as well as the air gap. A major downside of this approach is Gibbs phenomenon that contributes to the error and slows down the convergence.

When the electric machine geometry is periodic, it is possible to use Fourier series to describe the spatial quantities. In order to make the motor geometry periodic in polar coordinate system, a few minor corrections on the slot wall are performed without affecting the final solution. After the simplification, the periodic distributions of the machine geometry are represented using Fourier series. On the rotor side, the permanent magnet is represented in the Fourier form. Similarly, the teeth and slots regions are

modelled in the stator side. For each layer, the definition of magnetic vector potential and Ampere's circuital law are defined as

$$\mu_r H_r = \frac{1}{r}\frac{\partial A_z}{\partial \theta} \tag{3.131}$$

$$\mu_\theta H_\theta = -\frac{\partial A_z}{\partial r} \tag{3.132}$$

$$J_z = \frac{1}{r}H_\theta + \frac{\partial H_\theta}{\partial r} - \frac{1}{r}\frac{\partial H_r}{\partial \theta} \tag{3.133}$$

where H_r and H_θ are the radial and tangential field strength, A_z is the magnet vector potential in the axial direction, J_z is the current density, and μ_r and μ_θ are the iron permeability components. By replacing the spatial distribution of the permeability and current density in θ direction with the coefficients of Fourier series and leaving the radial component in the analytical form, the final equation, which is a simple second order ODE, can be obtained and solved for vector potential (A_z).

$$A_z = W r^{\lambda_m} a + W r^{-\lambda_m} b + r^2 G_1 \tag{3.134}$$

The vector potential is used to model each region of the geometry and couple the regions with each other using boundary conditions from (3.122) and (3.123). The final system is solved for the unknowns a and b. Furthermore, λ_m and W are the results of eigendecomposition and G_1 is the constant which stands for the source components in the region. If the unknowns are solved for the whole region, which includes the stator region, the field solution in the teeth can also be obtained [39].

3.1.7 Finite Element Analysis

The reference results are obtained from commercial finite element software (FLUX2D). It is well known that the accuracy of the solution in FEA is constrained by the number of mesh elements and the mesh density in the required regions such as air gap. In this case, the mesh density is increased until a limit where further refinement of the mesh will not change the field solution significantly. Second order element is used to define the mesh properties. For the iron teeth, a high value of the relative permeability is assigned ($\mu_r = 10^4$) to approximate the assumption of infinite permeability in the considered mathematical models. The computation time necessary to obtain the results from FEA is around two minutes, which is used as a reference in the performance analysis.

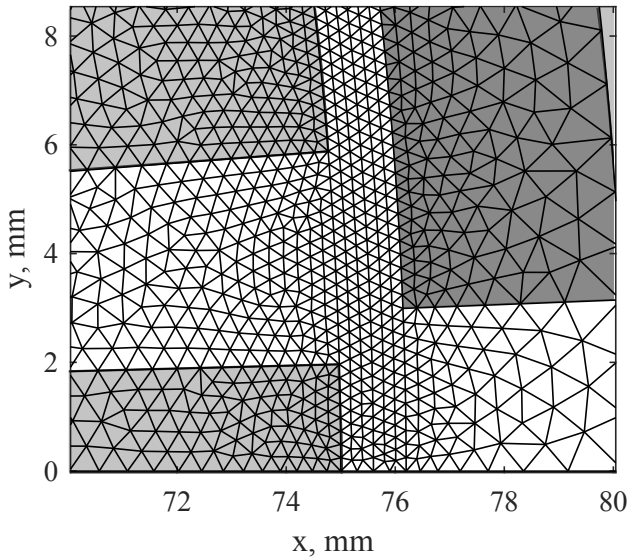

Fig. 3.21: *Finite element mesh of the motor geometry*

3.2 Comparison of the modelling techniques

3.2.1 Magnetic field solution comparison

The waveforms of radial flux density obtained from the models are compared in Fig. 3.22 (a) and all the methods except Carter factor and relative permeance model give good results. The tangential field solution, in Fig. 3.22 (b), is accurately calculated by mode matching, harmonic model, and semi-analytical conformal mapping. The complex permeance model has some deviations. The Carter factor and relative permeance models do not capture the field variations in the tangential direction.

3.2.2 Torque comparison

The Carter factor does not capture the local field distortion in the air gap due to slotting, so the cogging torque (T_c) cannot be calculated. In the relative permeance method, as the tangential field variations are not known, the lateral forces acting on the teeth sides are summed and the expression for T_c is given as in [89]

$$T_c = \sum_{k=1}^{Qs} la \int_0^{\frac{b_0}{2}} \left(\frac{B_1^2 - B_2^2}{2\mu_0} \right) r_t dy \tag{3.135}$$

where B_1 and B_2 are the flux densities along the opposite walls of the slot and r_t is $R_s - r_s$ as in Fig. 3.6.

The closed form solution of the cogging torque is derived based on Maxwell stress

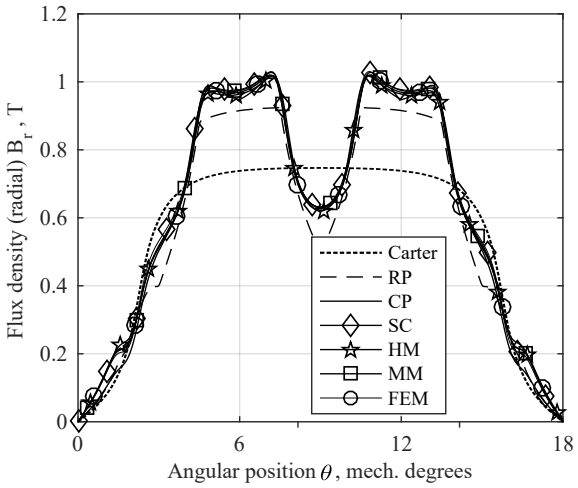

(a) Radial component

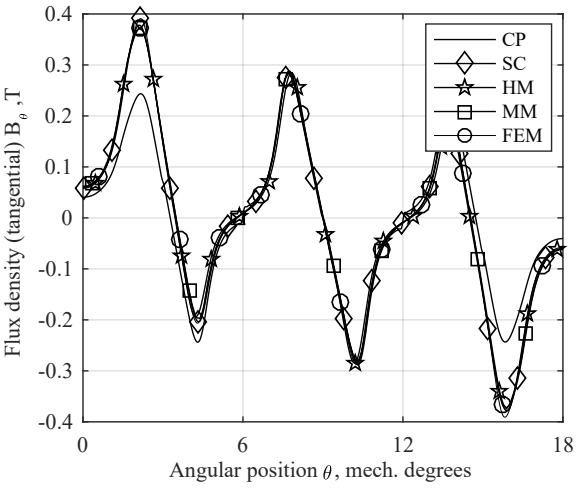

(b) Tangential component

Fig. 3.22: *Permanent Magnet field solution across single pole*

tensor in the complex permeance model.

$$T_c = \frac{1}{\mu_0} l_a R^2 \int_0^{2\pi} B_{sr} B_{s\theta} d\theta \tag{3.136}$$

In the mode matching, harmonic model and semi-analytical conformal mapping, the tangential component of Maxwell stress tensor is integrated numerically as the field solutions should be recalculated for every rotor position. The FEM software employs virtual work method to compute the torque waveform.

The electromagnetic torque is obtained from stator flux linkage in the d axis (Ψ_d) and stator current in the q axis (I_q) according to the space vector theory [90] and it is added with the cogging torque to get total torque.

$$T_{em} = \frac{3p}{2} \Psi_d I_q \tag{3.137}$$

From Fig. 3.23, it is evident that the results from mode matching, harmonic model, and semi-analytical conformal mapping are in good agreement with the FEM results. The electromagnetic torque calculated by the complex permeance model is comparable, but the cogging torque has some deviations. The inaccuracies of the field solutions in the relative permeance and Carter factor models produce the discrepancies in the cogging and total torque values.

3.2.3 Back-Emf comparison

The back-emf produced in a single phase winding is computed by differentiating the flux linkage in a coil and multiplying with the number of coils in series according to Faraday's law.

$$E_p = -N_s \frac{\mathrm{d}\phi_c}{\mathrm{dt}} \tag{3.138}$$

where

$$\phi_c = l_a R \int_{-\frac{\gamma_c}{2}}^{\frac{\gamma_c}{2}} B_{sr}(R, \theta, t) \mathrm{d}\theta$$

The flux linkage (ϕ_c) of a coil is obtained by integrating the flux density in the radial direction across one coil pitch analytically or numerically. As the back-emf can be calculated using all six methods considered in this study, the performance analysis of these methods is carried out based on this global parameter.

3.2.4 Core loss comparison

In the permanent magnet machines, the core loss is dominated by the permanent magnet flux variation in the stator iron, so the no-load field solutions from the analytical methods are used to estimate the core losses using Bertotti's equation (3.139).

$$P_c = \frac{\sigma}{6} (d\pi \hat{B} f)^2 + k_{hys} \hat{B}^{\alpha} f + k_{exc} (\hat{B} f)^{\frac{3}{2}} \tag{3.139}$$

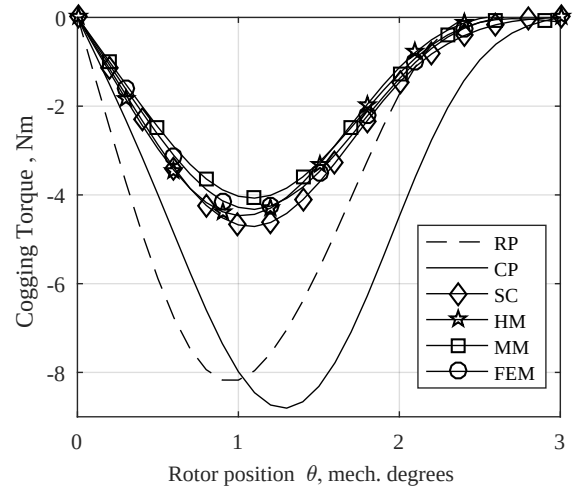

(a) Cogging torque

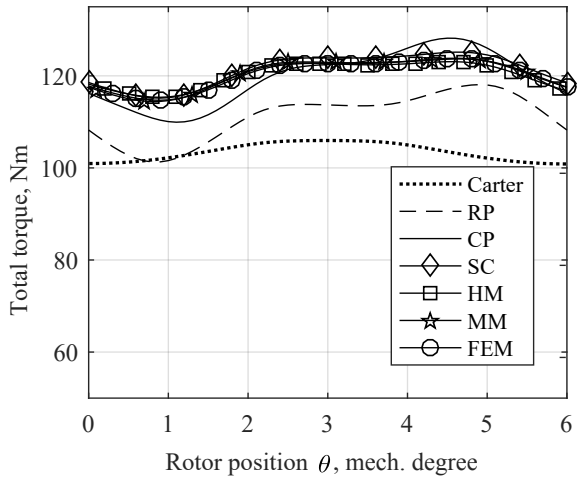

(b) Total torque

Fig. 3.23: *Torque waveforms*

where k_{hys} is the hysteresis loss coefficient, k_{exc} is the eddy current loss coefficient, f is the electrical frequency, $\hat{B}$ is the peak value of flux density waveform, d is the thickness of lamination, and σ is the electrical conductivity of the material. The coefficient α is determined by curve fitting the steel lamination data provided by manufacturers. The harmonic flux components in the stator tooth ϕ_{tsn} are obtained by integrating the harmonic components of radial flux density solution of the permanent magnet across a slot pitch (3.140).

$$\phi_{tsn} = l_a R \int_{-\frac{\pi}{Q_s}}^{+\frac{\pi}{Q_s}} B_{srn}(R, \theta, t) d\theta \tag{3.140}$$

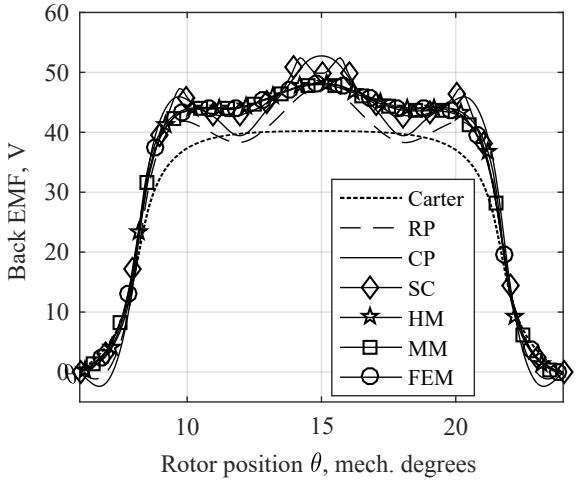

Fig. 3.24: *Back-emf waveforms of phase A*

The relationship between the tooth and yoke flux in the frequency domain is given by

$$|\phi_{tsn}| = |\phi_{tyn}| 2 \sin(np\frac{\pi}{Q_s}) \tag{3.141}$$

The tooth is divided into different segments due to the variation of its cross-sectional area (A_{ct}) and the flux density is calculated in each segment separately. The flux density in the yoke is evaluated from ϕ_{tyn} and the cross sectional area of the yoke (A_{cy}). A generic form of the flux density calculation can be expressed as

$$B_n = \frac{\phi_n}{A_c}. \tag{3.142}$$

From the Fourier coefficients, the time domain waveforms of flux density in the tooth and yoke regions are derived and the peak values are obtained.

$$\hat{B} = \max\left(\sum_n B_n \cos(n\omega t)\right) \tag{3.143}$$

A transient simulation is performed using the FE model described in section 3.1.7 at a constant speed ($2\pi f/p$) to calculate the iron losses as per Bertotti's equation. The core loss values calculated using FEA and the analytical models are compared in Table.3.2. The core loss estimation of complex relative permeance method, semi-analytical conformal mapping method, mode matching technique, and harmonic model are comparable with FEM results, since their radial field solutions are closely matching.

3.2.5 Performance analysis

The calculation time is influenced by number of harmonics and discretisation points (in the case of semi-analytical method). The number of harmonics denotes the maximum order of harmonics used in the slotless air-gap field distribution equations (3.31)

Table 3.2: *Comparison of motor modelling methods based on the accuracy core loss calculation*

Analytical methods,	Core loss estimation,	Unit
Carter factor method	13.76	W
Relative permeance method	16.92	W
Complex relative permeance method	19.84	W
Semi-analytical conformal mapping method	20.10	W
Mode matching technique	20.03	W
Harmonic modelling	19.67	W
Finite element analysis	22.98	W

to (3.34) or in the Fourier equation (3.134) of the Harmonic model. The number of discretisation points represents the number of evaluation points at the air-gap centre along the angular span of two pole pitches used in the calculation of field solution.
A parameter sweep analysis is performed by varying the number of harmonics or discretisation points to evaluate the accuracy and modelling complexity of each analytical method. The back-emf is compared with the FEA result in the frequency domain and the relative error is computed as,

$$Relative\ error = \frac{1}{N}\sum_{i=0}^{N}\left(\frac{E_{AM.i} - E_{FEA.i}}{E_{FEA.i}}\right).100 \tag{3.144}$$

where $E_{AM.i}$ and $E_{FEA.i}$ are the magnitudes of the i^{th} harmonic component obtained by analytical methods and FEA respectively.
The analytical conformal mapping techniques are computationally cheap since the closed form solutions for back-emf are available. The other mathematical models are computationally more expensive since the field solution has to be calculated for every rotor position. The semi-analytical conformal mapping, mode matching, harmonic modelling, and complex permeance methods are more accurate than Carter factor and relative permeance models. The mode matching and complex relative permeance models have the best compromise between accuracy and computation time.

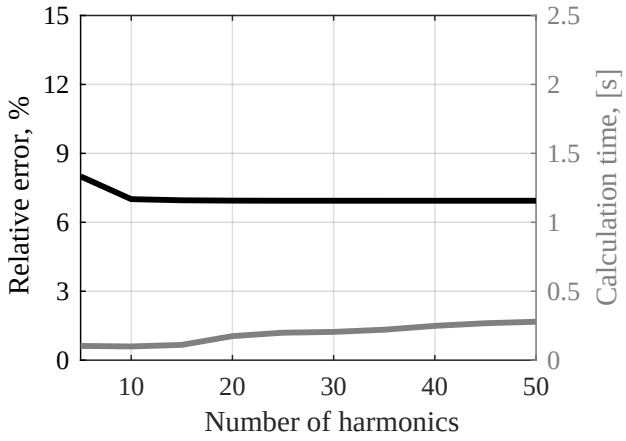

(a) Carter method based on number of harmonics

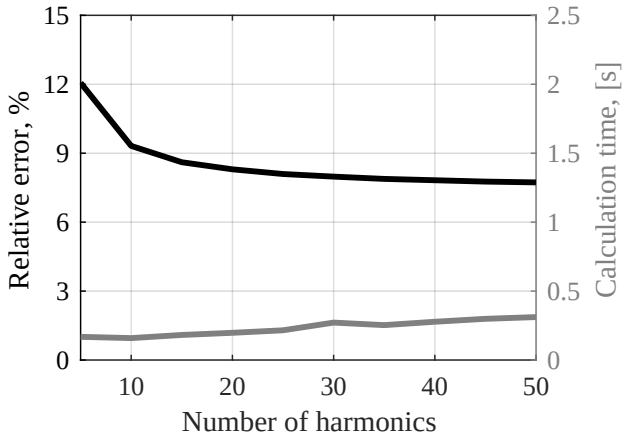

(b) Relative permeance method based on number of harmonics

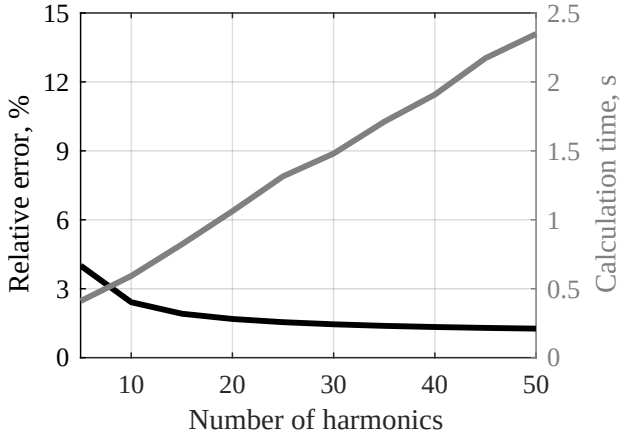

(c) Complex permeance method based on number of harmonics

Fig. 3.25: *Performance analysis results of models that have closed form solution for back-emf*

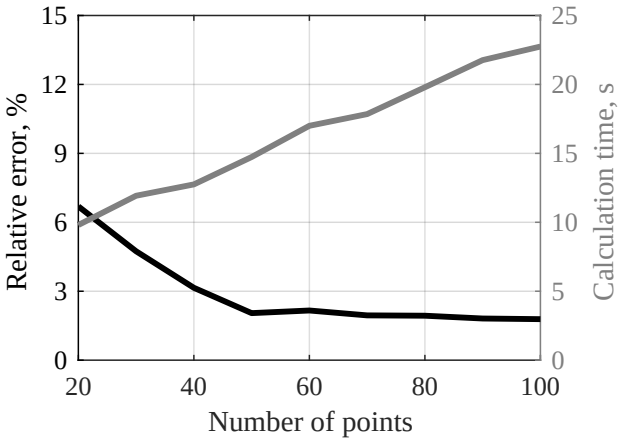

(a) Semi-analytical method based on number of discretisation points

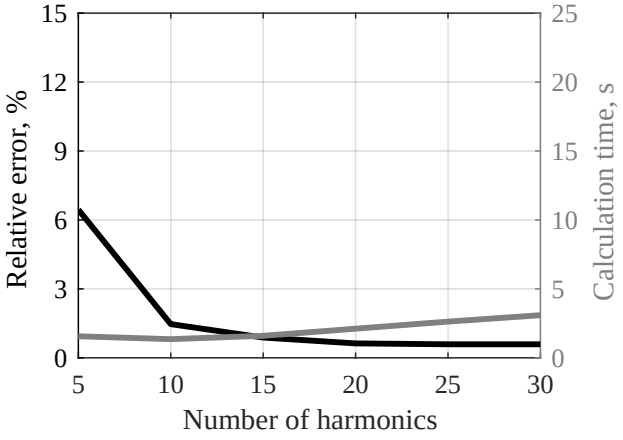

(b) Mode matching technique based on number of harmonics

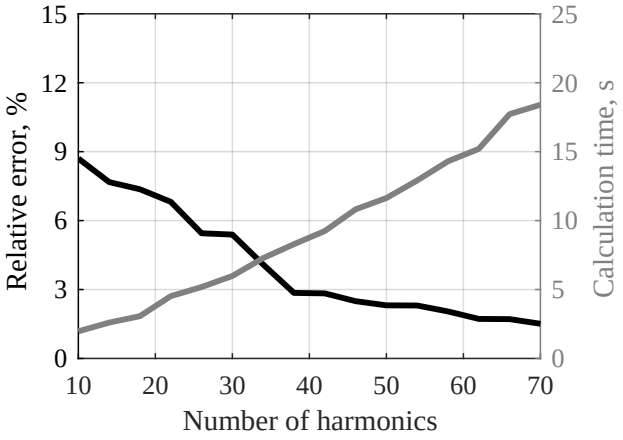

(c) Harmonic model based on number of harmonics

Fig. 3.26: *Performance analysis results of models that do not have closed form solution for back-emf*

CHAPTER 4

Comparison of electric motor scaling methods

In order to evaluate the motor design candidates during the optimisation process, an appropriate model is required. The design candidates are the scaled versions of a reference motor and their performance including operating efficiencies is estimated using the motor model. The motor operating points in the New European Driving Cycle (NEDC) are shown in Fig. 4.1. The aim of the optimisation process is to bring the maximum efficiency region closer to the operating points without violating constraints including maximum allowable inverter voltage and current. This chapter compares four

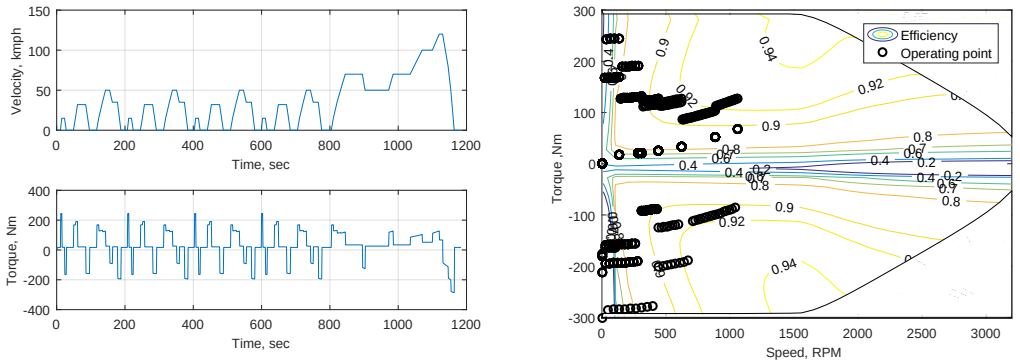

(a) NEDC Driving cycle

(b) Efficiency map

Fig. 4.1: *Electric motor operating points in the NEDC.*

such scaling methods for their accuracies and computational complexities against FEM based commercial software. The considered methods are proportional scaling of effi-

ciency map, Willans line model, scalable saturated motor model, and analytical motor model.

4.1 Proportional scaling of efficiency map

Scaling of the efficiency maps is used in many different vehicle simulation packages including Powertrain System Analysis Toolkit (PSAT) [22], ADvanced VehIcle SimulatOR (ADVISOR) [91–93], and QSS Toolbox [94]. In these tools, the reference efficiency maps are given as matrices of size $m \times n$ where m is the length of shaft speed vector (x-axis) and n is the length of shaft torque vector (y-axis).

$$\begin{aligned} x_\omega &= \{x_1, x_2 .... x_m^{ref}\} \\ y_T &= \{y_1, y_2 .... y_n^{ref}\} \end{aligned} \tag{4.1}$$

and the efficiency at each operating point is defined as,

$$\eta^{ref} = \{\eta_{1,1}, ..., \eta_{2,1}, ..., \eta_{m,n}^{ref}\} \tag{4.2}$$

The x and y axes of the torque-speed plane are scaled based on the required maximum torque (T_{max}^{req}) and speed (ω_{max}^{req}) of the scaled motor.

$$\tilde{y}_T = \frac{T_{max}^{req}}{T_{max}^{ref}} . y_T \tag{4.3}$$

$$\tilde{x}_\omega = \frac{\omega_{max}^{req}}{\omega_{max}^{ref}} . x_\omega \tag{4.4}$$

where (T_{max}^{ref}) and (ω_{max}^{ref}) are the max torque and max speed of reference motor.
It can be observed that the efficiency matrix in (4.2) is preserved in the process of scaling, but the x and y-axes values and limits are changed. The total loss map of the machine is calculated from the efficiency and corresponding shaft torque and speed.

$$P_{loss} = \left(\frac{1}{\eta} - 1\right) T\omega \tag{4.5}$$

This scaling approach does not give any geometrical information of the scaled motor and details regarding the distribution of losses which are required to perform thermal calculations. The model is also valid only in the neighbourhood of the reference motor where the efficiency map would not change drastically [22].

4.2 Willans line model

The base of Willans line model is the affine relation of the energy available for the conversion P_{in} to the output energy of the energy converter P_{out}. The model was initially used to relate the brake mean effective pressure and fuel consumption of internal combustion engines [95]. Rizzoni et al., [96] extended it to generalised energy converters such as electric motors as in

$$\begin{aligned} P_{in} &= VI \\ P_{out} &= T\omega \\ \eta &= \frac{P_{out}}{P_{in}}. \end{aligned} \tag{4.6}$$

The input and output powers of the electric motor are related as

$$P_{out} = e_{int}P_{in} - P_{loss} \tag{4.7}$$

where e_{int} represents the intrinsic energy conversion efficiency and P_{loss} represents the losses. The model can be made scalable by normalizing the torque and rotor speed in analogy to what is done for IC engines in [95]. The normalised parameters do not change while scaling the motors.

The mean effective pressure (p_{me}) of the electric motor is defined as a ratio between tangential force acting on the rotor periphery and its surface area.

$$p_{me} = \frac{T_{out}}{r2\pi rl} = \frac{T_{out}}{2V_{rotor}} = \frac{P_{out}}{2V_{rotor}\omega_{sh}} \tag{4.8}$$

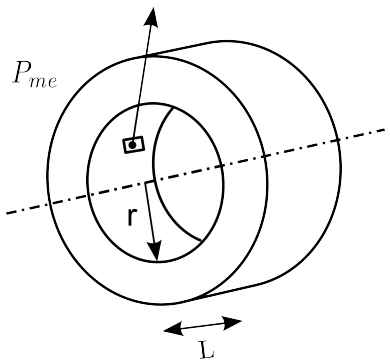

Fig. 4.2: *Physical parameters of the rotor.*

Similarly the mean available pressure (p_{ma}), mean loss pressure (p_{mloss}), and mean

tangential speed of the rotor (C_m) are defined as

$$p_{ma} = \frac{P_{in}}{2V_{rotor}\omega_{sh}} \tag{4.9}$$

$$p_{mloss} = \frac{P_{loss}}{2V_{rotor}\omega_{sh}} \tag{4.10}$$

$$C_m = r\omega_{sh}. \tag{4.11}$$

Therefore (4.6) can be rewritten in the form of normalised variables as

$$p_{me} = e_{int}p_{ma} - p_{mloss} \tag{4.12}$$

The intrinsic efficiency (e_{int}) and the mean loss pressure (p_{mloss}) which are derived by curve fitting p_{me} and p_{ma} for every speed C_m as in Fig. 4.3, are approximated as polynomial functions of C_m as expressed in (4.13) and (4.14).

$$e_{int} = \sum_{i=0}^{4} e_{inti}C_{mi} \tag{4.13}$$

$$p_{ml} = \sum_{i=0}^{4} p_{mli}C_{mi} \tag{4.14}$$

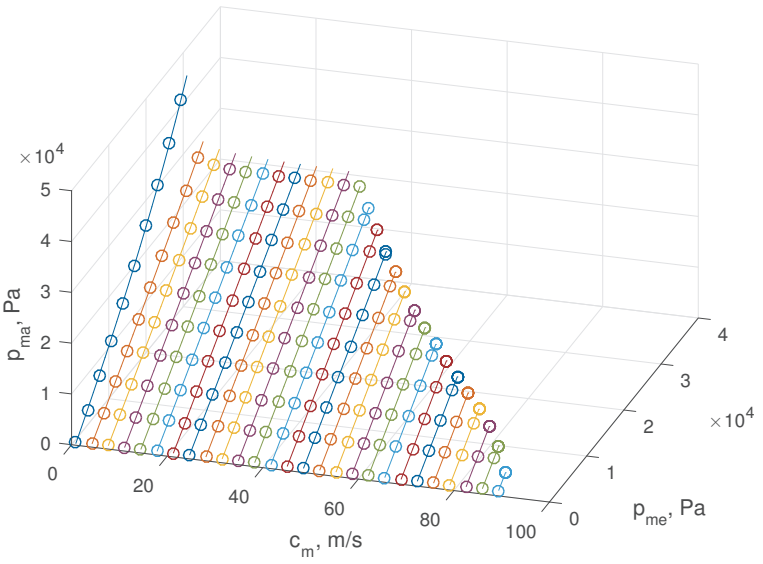

Fig. 4.3: *Willans line model (lines) created from an existing efficiency map (o markers)*

Based on the equations (4.9)-(4.11), the rotor dimensions (consequently also the stator dimensions) such as radius r and stack length l are scaled to achieve the desired output power without altering the normalised parameters. Figure 4.3 shows the Willans line model of a 20 kW electric machine (circles) scaled from a 66 kW machine (solid line).

Thus, the Willans line model can be used to scale the electric motors and to obtain the efficiency maps of the scaled motors.

Similar to the efficiency map scaling, the distribution of losses is not known even in the Willans line model as the intrinsic efficiency accounts for the energy conversion losses and P_{loss} captures the remaining losses collectively. Hence, the thermal calculations can not be performed also with this approach.

4.3 Scalable saturated motor model

The previously described models lack the physical description of the scaling process. The scalable saturated motor model [25] combines the current-dependent flux linkage and loss models (mapping functions) with the scaling laws. The mapping functions for the flux linkage, hysteresis losses in the iron, and eddy current losses in the iron and magnet are created based on transient finite element (FE) calculations. The load points are defined as equidistant points on a regular grid of current amplitude (0, I_{max}) and phase advance angle (0, $\frac{\pi}{2}$). The saturation effect of flux-linkages in dq axis are modelled as polynomial expressions of the current amplitude and phase angle as in (4.15) and (4.16). The frequency independent hysteresis loss and eddy current loss terms are modelled using cubic functions as in (4.17) and (4.18), respectively.

$$\psi_d = p_d(I, \gamma) \tag{4.15}$$

$$\psi_q = p_q(I, \gamma) \tag{4.16}$$

$$\frac{P_{c,hys}}{f} = c_{c,hys}(I, \gamma) \tag{4.17}$$

$$\frac{P_{c,eddy}}{f^2} + \frac{P_{pm}}{f^2} = c_{c,eddy}(I, \gamma) + c_{pm}(I, \gamma). \tag{4.18}$$

The mapping functions can be used to model the performances of the reference motor. The parameters including electromagnetic torque $T_{em,ref}$, shaft torque $T_{sh,ref}$, core losses $P_{c,ref}$, magnet losses $P_{pm,ref}$, mechanical losses $P_{mech,ref}$, DC component of the winding losses $P_{a,ref}$, and terminal voltage V_{ref} are modelled as:

$$T_{em,ref} = \frac{3}{2} p \left(\Psi_d I_q - \Psi_q I_d \right) \tag{4.19}$$

$$T_{sh,ref} = T_{em,ref} - \frac{P_{a,ref} + P_{pm,ref} + P_{mech,ref}}{\omega_{sh}} \tag{4.20}$$

$$P_{c,ref} + P_{pm,ref} = c_{c,hys} f + (c_{c,eddy} + c_{pm}) f^2 \tag{4.21}$$

$$P_{a,ref} = 3 R_{DC} \sqrt{I_q^2 + I_d^2} \tag{4.22}$$

$$V_{ref} = \sqrt{(R_{DC} I_d - \omega \Psi_q)^2 + (R_{DC} I_q + \omega \Psi_d)^2} \tag{4.23}$$

where I_d and I_q are dq components of the current vector and R_{DC} is the armature phase resistance.

Mechanical loss model

As the analytical prediction of the mechanical losses (P_{mech}) are complicated and inaccurate, a simplified empirical model with a speed-independent friction torque T_{fr} is employed.

$$P_{mech,ref} = T_{fr,ref} \omega_{sh,ref} \tag{4.24}$$

The experimental set-up in Fig. 4.4 is used to measure the T_{fr}. After removing the permanent magnet and armature winding from the studied in-wheel electric motor, it is driven at fixed speeds using an external motor (EM). The resistance torque is measured using a torque transducer (T).

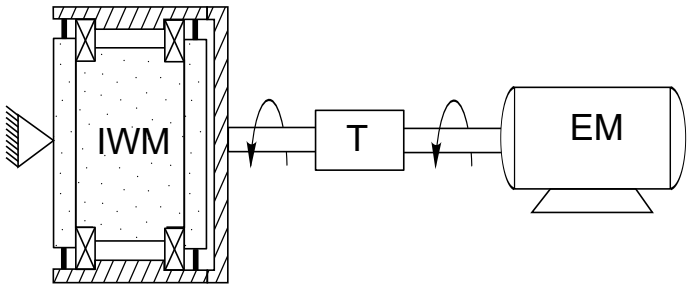

Fig. 4.4: *Experimental setup to measure the frictional loss.*

Efficiency calculation

The efficiency map is recalculated for the reference motor from the losses and shaft output power at every operating point in the torque-speed plane and compared with the

FEM results in Fig. 4.8.

$$P_{loss,ref} = P_{c,ref} + P_{pm,ref} + P_{mech,ref} + P_{a,ref} \tag{4.25}$$

$$\eta_{m,ref} = \frac{T_{sh,ref}\omega_{sh,ref}}{T_{sh,ref}\omega_{sh,ref} + P_{loss,ref}} \tag{4.26}$$

Estimation of the torque envelopes in both the motoring and generating regions of the efficiency map can also utilise these mapping functions instead of relying on constant inductance phasor diagrams.

Motor scaling

In order to scale the presented flux linkage and loss model, the analytical scaling laws described in [97] can be effectively utilised as in (4.31)-(4.38). It can be observed that the AC winding losses are not scaled using this approach.

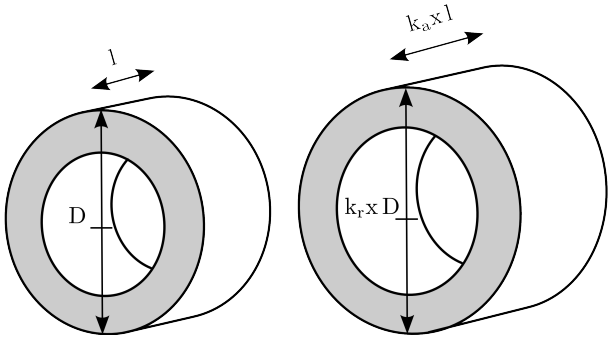

Fig. 4.5: *Geometrical scaling of the reference machine using the factors k_a and k_r*

The scaling laws are based on proportional geometrical scaling of the reference motor in the axial and radial directions as shown in Fig. 4.5 along with the winding scaling.

1. Axial scaling (lengthening / shortening of the core) using k_a
2. Radial scaling (proportional scaling of cross-section) using k_r
3. Rewinding (changing the number of turns per and parallel coil paths) using k_W

The general scaling equations of the axial and radial parameters (l and D), and the winding are written as,

$$l = k_a l_{ref} \tag{4.27}$$

$$D = k_r D_{ref} \tag{4.28}$$

$$\frac{n_c}{a_p} = k_W \frac{n_{c,ref}}{a_{p,ref}}. \tag{4.29}$$

where n_c is the number of turns per coil and a_p is the number of parallel paths. Depending on the application and motor type, either k_a or k_r can be fixed to allow scaling

in one direction. It is also possible to define bounds for the ratios to avoid tube-shaped or disc-shaped scaled motors. The winding scaling factor k_W is chosen such that the scaled motor terminal voltage at the base speed closely matches the inverter maximum voltage V_{lim}. The stator current is scaled according to:

$$I = \frac{k_r}{k_W} I_{ref} \tag{4.30}$$

Consequently, the performance parameters of the scaled and reference motors at a certain rotor speed (supply frequency) are related according to

$$\Psi_d = k_W k_r \left(k_a \Psi_{dco,ref} + k_r \Psi_{ew,ref}\right) \tag{4.31}$$

$$\Psi_q = k_W k_r \left(k_a \Psi_{qco,ref} + k_r \Psi_{ew,ref}\right) \tag{4.32}$$

$$T_{sh} = k_r^2 k_a T_{sh,ref} \tag{4.33}$$

$$P_c = k_r^2 k_a P_{c,ref} \tag{4.34}$$

$$P_{pm} = k_r^2 k_a P_{pm,ref} \tag{4.35}$$

$$P_{mech} = k_r^2 k_a P_{mech,ref} \tag{4.36}$$

$$R_{DC} = \frac{k_W^2}{k_r^2} \left(k_a R_{DCco,ref} + k_r R_{DCew,ref}\right) \tag{4.37}$$

$$P_a = k_a P_{aco,ref} + k_r P_{aew,ref}. \tag{4.38}$$

where co and ew represent the stack and end-winding regions that are scaled separately. Equation (4.35) can be expanded to take into account the 3D effects of permanent magnet losses as given in [98].

In order to calculate the efficiency maps of the scaled machines, the stator current magnitudes and phase angles (I, γ) should be determined for each torque-speed combination. A constraint minimisation algorithm, *fmincon* in Matlab, is employed to estimate stator current (I_s) which will produce the demanded output torque (T_{op}) without violating the constraint on inverter voltage (V_{lim}) [99].

$$\min_{\mathbf{x} \in (I,\gamma)} I_s(I, \gamma) \tag{4.39}$$

$$\text{subject to} \quad T_{sh} = T_{op},$$

$$V \leq V_{lim} \tag{4.40}$$

Thus, the efficiency maps of scaled machines can be calculated accurately (compared in Fig. 4.9) using computationally inexpensive scalable motor model.

4.4 Analytical motor model

The scaled machines can be analytically modelled based on their geometrical details. From the comparison study in Chapter 3, it was observed that the complex permeance method gives accurate radial field solution and has minimum calculation time for the global parameters. Hence, it is further developed to compute the efficiency map.
As a first step, the d-q axes currents need to be estimated for each load point in the torque-speed plane. In the constant torque region, the I_d current is forced to zero and I_q is derived from the required electromagnetic torque (T_{em}).

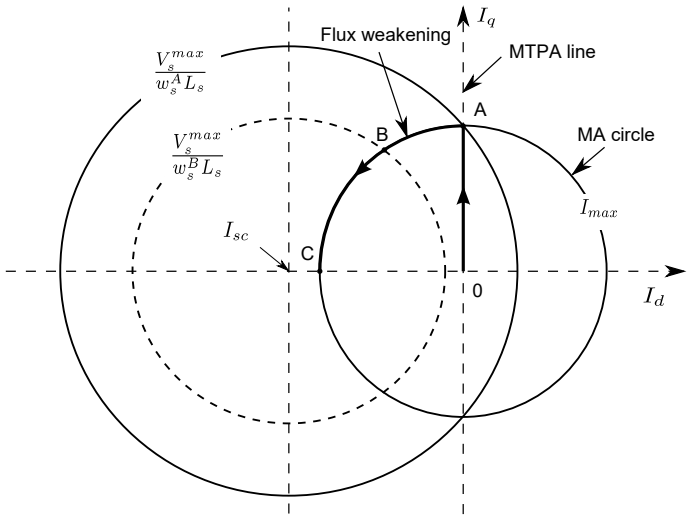

Fig. 4.6: *Current locus diagram of outer rotor surface permanent magnet machine with short-circuit current (I_{sc}) greater than maximum allowable stator current (I_{max})*

$$I_q = T_{em}\frac{2}{3p\psi_d} \tag{4.41}$$

where ψ_d is the flux linkage in d-axis and p is the number of pole pairs. The reluctance torque is ignored in (4.41) as the inductance variation between d-q axes is negligible ($L_d = L_q = L_s$). The ψ_d is the sum of permanent magnet flux linkage in d axis $\psi_{(pm-d)}$ and the contribution from the d-axis current.

$$\psi_d = \psi_{(pm-d)} + L_d I_d \tag{4.42}$$

The terms $\psi_{(pm-d)}$ and L_d are calculated as explained in Appendix A and Appendix B respectively. In the flux weakening region, ψ_d is reduced to meet the constraint on inverter voltage by supplying negative I_d current. Its magnitude is determined based on the operating speed for the motor as in (4.43) [90].

$$I_d = \frac{\psi_d^2 + L_s^2 I_{max}^2}{2L_s\psi_d}\left[\left(\frac{\omega_s^A}{\omega}\right) - 1\right] \tag{4.43}$$

where I_{max} is the maximum stator current and ω is the operating speed. The rated speed of the motor ω_s^A is derived from the rated voltage of the motor V_r.

$$w_s^A = \frac{V_r}{\sqrt{(L_s I_q)^2 + (\psi_{pm} + L_s I_d)^2}} \tag{4.44}$$

Motor losses

Based on the stator current vector and the operating speed, the motor losses are calculated. The formulation of winding losses, core losses, magnet losses, and mechanical losses are discussed individually below.

Winding Losses

The copper loss model includes AC losses due to skin effect inside conductors and additional losses due to proximity effect. It also captures the effect of winding temperature on the losses [100].

$$P_a = 3I_s^2 R_{AC} + P_{proximity} \tag{4.45}$$

The effective resistance (R_{AC}) that accounts for the skin effect in the conductor is modelled as a function of conductor dimensions, operating frequency and winding temperature. The conductors are layered in the slot as shown in Fig. 4.7. The detailed explanation of the model can be found in [100].

$$R_{AC} = K_{AC} N_s \frac{1}{\sigma_0} \frac{2(l_a + l_{ew})}{A_c} (1 + \beta_0 (T - T_0)) \tag{4.46}$$

The AC loss factor K_{AC} can be modelled as,

$$K_{AC} = \left(\frac{360 + 3\gamma^4}{360 + \gamma^4} + \left(\frac{\sum_{l-1} NI}{N_l I_0} \right)^2 \frac{2\gamma^4}{24 + \gamma^4} \right) \tag{4.47}$$

where $\sum_{l-1} NI$ and N_l are defined according to Fig. 4.7 [100], I_0 is the current in layer l, N_s is the number coils connected in series, σ_0 is the conductivity of copper at reference temperature ($T_0 = 20^o C$), l_a is the stack length, l_{ew} is the end winding length, A_c is the cross-sectional area of the wire, and T is the winding temperature. The characteristic dimension γ and the AC loss temperature coefficient β_t are defined as

$$\gamma = 0.93 \sqrt{\epsilon_l} \frac{D_c}{\delta} \tag{4.48}$$

$$\beta_t = \alpha_t - \alpha_0 \frac{1}{K_{AC}} \left(\frac{\sum_{l-1} NI}{N_l I_0} \right)^2 \frac{384\gamma^4}{(24 + \gamma^4)^2} \tag{4.49}$$

where ϵ_l is the slot fill ratio, D_c is the diameter of the conductor, and α_t is the temperature coefficient of the conductor material. The skin depth δ is defined as

$$\delta = \sqrt{\frac{2}{\sigma \omega_e \mu_0}} \tag{4.50}$$

where w_e is electrical frequency and μ_0 is permeability of free space. The induced conductor proximity loss from the enclosed ampere turns is given by

$$P_{proximity} = \frac{2l_a}{\sigma D_c^2} \left(\frac{\sum_{l-1} NI}{N_l} \right)^2 \frac{2\gamma^4}{24 + \gamma^4}. \tag{4.51}$$

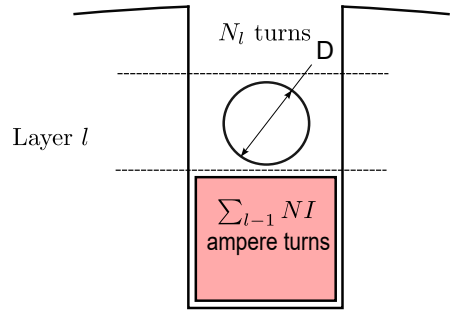

Fig. 4.7: *Winding layer arrangement with circular conductors*

Core Losses

The eddy current and hysteresis losses produced by the permanent magnet flux variation in the stator are calculated in Section. 3.2.4 using Bertotti's equation. This approach ignores the losses due to the armature flux and the reduction of permanent magnet flux in the flux-weakening region.

Magnet losses

Space harmonics in the armature winding magnetomotive force (MMF) distribution and time harmonics in the current waveform, together with the harmonics in the air gap permeance function due to slotting, create field components which do not rotate in synchronism with the rotor. Consequently, these field harmonics induce eddy currents in the rotor magnets and generate power losses.

Eddy currents induced in the rotor magnet due to nth harmonic component of the armature field satisfy the Helmholtz equation which can be written in 2-D polar coordinates

in the phasor form

$$\frac{\partial^2 \tilde{J}_{zn}}{\partial r^2} + \frac{1}{r}\frac{\partial \tilde{J}_{zn}}{\partial r} + \frac{1}{r^2}\frac{\partial^2 \tilde{J}_{zn}}{\partial \theta'^2} = k_n^2 \tilde{J}_{zn} \tag{4.52}$$
$$k_n^2 = j\omega_n \mu_{pm} \rho_{pm}$$
$$\theta' = \theta - \omega_{rm} t$$

where μ_{pm} and ρ_{pm} are the permeability and electric conductivity of the permanent magnet respectively, n is the harmonic order of the armature winding field component which induces eddy currents, ω_n is the frequency of the n^{th} harmonic, θ' and θ are the angular positions of a point on the magnet surface with respect to the rotor and stator respectively, and ω_{rm} is the rotor mechanical speed. The general solution of (4.52) is given by [101].

$$\tilde{J}_{zn}(r,\theta') = \sum_{m=0}^{\infty} \left[A_m I_m(k_n r) + B_m K_m(k_n r)\right] \left[C_m \cos(m\theta') + D_m \sin(m\theta')\right] \tag{4.53}$$

where I_m and K_m are the modified Bessel functions of the first and second kind of order m respectively, while A_m, B_m, C_m and D_m are the constants. Combining (4.53) with the relationship between radial and tangential components of the magnetic field intensity in the magnet and the induced eddy currents

$$\nabla x J_n = \frac{1}{r}\frac{\partial \tilde{J}_{zn}}{\partial \theta'}\mathbf{a}_r - \frac{\partial \tilde{J}_{zn}}{\partial r}\mathbf{a}_{\theta'} = -j\omega_n \mu_{pm} \rho_{pm} (\tilde{H}_{rn}\mathbf{a}_r \tilde{H}_{\theta' n}\mathbf{a}_{\theta'}) \tag{4.54}$$

the following equations are obtained

$$\tilde{H}_{rn}(r,\theta') = -\frac{m}{k_n^2 r}\sum_{m=0}^{\infty}[A_m I_m(k_n r) + B_m K_m(k_n r)][-C_m \sin(m\theta') + D_m \cos(m\theta')] \tag{4.55}$$

$$\tilde{H}_{\theta' n}(r,\theta') = \frac{1}{k_n}\sum_{m=0}^{\infty}[A_m I'_m(k_n r) + B_m K'_m(k_n r)][C_m \cos(m\theta') + D_m \sin(m\theta')] \tag{4.56}$$

where I_m and K'_m are the derivatives of Bessel functions. Similar relations can be written for flux density as well since

$$\tilde{B}_n = \mu_{pm}\tilde{H}_n \tag{4.57}$$

The unknown constants are determined by applying boundary conditions on the rotor and magnet surfaces, i.e.

$$\tilde{H}_{\theta' II}(R_r,\theta') = 0 \tag{4.58}$$
$$\tilde{B}_{rnI}(R_m,\theta') = \tilde{B}_{rnII}(R_m,\theta')$$

where I and II denote the air gap and magnet regions respectively, while R_r and R_m are the radii of rotor and magnet respectively. The radial component of flux density on the magnet surface produced by the armature winding currents consists of the direct component ($\tilde{B}_{rn1}$) forming a wave which rotates in the same direction as the rotor and inverse component ($\tilde{B}_{rn2}$) which rotates in the opposite direction of the rotor. The phasors of these two components are defined according to

$$\tilde{B}_{rn1}(r,\theta') = \tilde{C}_{r1n}[\cos(n\theta') - \sin(n\theta')] \tag{4.59}$$

$$\tilde{C}_{r1n} = N_c B_{arn}(R_m)\frac{1}{2} I_{max} \sum_{i=1}^{\frac{Q_s}{3}} \left[\mathrm{sgn}_{Ai} e^{jn\alpha_{Ai}} + \mathrm{sgn}_{Bi} e^{j\left(n\alpha_{Bi} - \frac{2\pi}{3}\right)} + \mathrm{sgn}_{Ci} e^{j\left(n\alpha_{Ci} + \frac{2\pi}{3}\right)}\right]$$

$$\tilde{B}_{rn2}(r,\theta') = \tilde{C}_{r2n}[\cos(n\theta') - \sin(n\theta')] \tag{4.60}$$

$$\tilde{C}_{r2n} = N_c B_{arn}(R_m)\frac{1}{2} I_{max} \sum_{i=1}^{\frac{Q_s}{3}} \left[\mathrm{sgn}_{Ai} e^{-jn\alpha_{Ai}} + \mathrm{sgn}_{Bi} e^{-j\left(n\alpha_{Bi} - \frac{2\pi}{3}\right)} + \mathrm{sgn}_{Ci} e^{-j\left(n\alpha_{Ci} + \frac{2\pi}{3}\right)}\right]$$

where B_{arn} are the Fourier coefficients of the radial component of flux density on the magnet surface ($r = R_m$) produced by a single coil of the armature winding with one turn ($Nc = 1$), I_{max} is the peak value of the current waveform (the phase current is assumed to be sinusoidal), sgnAi, sgnBi, sgnCi are the signs (+ or -) considering the referent orientation of the coil turns in phases A, B and C around the perimeter of the stator, α_{Ai}, α_{Bi}, α_{Ci} are the phase shifts of the field distributions of individual coils considering their position around the stator perimeter with respect to the referent coil ($\alpha_{A1} = 0$). Details about armature winding field solution used in (4.59) and (4.59) are provided in [82]. By combining the terms (4.55), (4.57), (4.58), (4.59) and (4.60) separately for direct and inverse field components, the unknown constants are obtained.

$$m = n$$

$$C_m = \begin{cases} j, & \text{for direct component} \\ -j, & \text{for inverse component} \end{cases}$$

$$D_m = 1$$

$$A_{nl} = -\frac{\tilde{C}_{rln}\frac{k_{nl}^2 R_m}{n\mu_{PM}} K_n'(k_{nl}R_r)}{K_n'(k_{nl}R_r) I_n(k_{nl}R_m) - K_n(k_{nl}R_m) I_n'(k_{nl}R_r)} \tag{4.61}$$

$$B_{nl} = \frac{\tilde{C}_{rln}\frac{k_{nl}^2 R_m}{n\mu_{pm}} I_n'(k_{nl}R_r)}{K_n'(k_{nl}R_r) I_n(k_{nl}R_m) - K_n(k_{nl}R_m) I_n'(k_{nl}R_r)} \tag{4.62}$$

In (4.61) and (4.62) the subscript $l = 1$ is used for direct component and $l = 2$ is used

for inverse component. The following is also valid

$$k_{n1}^2 = j(\omega - n\omega_{rm})\mu_{pm}\rho_{pm} \tag{4.63}$$

$$k_{n2}^2 = j(\omega + n\omega_{rm})\mu_{pm}\rho_{pm} \tag{4.64}$$

The power dissipated inside the magnet volume is equal to the real part of the integral of average Poynting vector across magnet surface, i.e.

$$\begin{aligned} P_{pm} &= Re\left\{\int_S \frac{1}{2}\left(\frac{\tilde{\mathbf{J}}}{\rho_{pm}} \times \tilde{\mathbf{H}}^*\right).ndS\right\} \\ &= 2p\sum_{l=1}^{2}\sum_{n=1}^{N_a} Re\left\{\int_{-\alpha_p\frac{\pi}{2p}}^{\alpha_p\frac{\pi}{2p}} \frac{1}{2}\frac{J_{znl}}{\rho_{pm}}\tilde{H}^*_{\theta' nl} R_m l_a d\theta'\right\} \end{aligned} \tag{4.65}$$

where N_a is the maximum order of Fourier coefficients in the armature winding field solution. After substituting (4.53) and (4.56) into (4.65) and performing integration, the final expression for magnet losses is

$$P_{pm} = 2p\sum_{l=1}^{2}\sum_{n=1}^{Na} Re\left\{\frac{1}{2\rho_{pm}}[A_{nl}I_n(k_{nl}R_m) + B_{nl}K_n(k_{nl}R_m)]\right. \tag{4.66}$$

$$\left.\cdot\left[\frac{1}{k_{nl}}A_{nl}I'_n(k_{nl}R_m) + B_{nl}K'_n(k_{nl}R_m)\right]^* R_m l_a \alpha_p \frac{\pi}{p}\right\} \tag{4.67}$$

Mechanical losses

The mechanical losses include frictional losses in the bearing P_{fr} and windage losses. The frictional losses can be quantified using the formula [102]

$$P_{fr} = k_{fb} m_r n_r 10^{-3} \tag{4.68}$$

where k_{fb} is the empirical constant, and m_r is the mass of the rotor, and n_r is the speed in rpm.

The windage losses are mainly governed by the motor operating speed [102] and an approximation can be made as follows.

$$P_{win} = 2D_{ro}^3 l_a n_r^3 10^{-6} \tag{4.69}$$

where D_{ro} is the rotor outer diameter, l_a is the stack length, and n_r is the speed in rpm. In order to estimate the k_{fb}, the in-wheel motor is made to run at different speeds without any active parts (magnet and armature winding) using an external motor and the mechanical resistance torque is measured using a torque transducer as shown in Fig. 4.4. As the motor parameters in (4.68) and (4.69) except k_{fb} are known, the experimental results can be used to back calculate the k_{fb}.

Efficiency

The efficiency is defined as output power at the shaft P_{out} divided by the input electrical power P_{in} as in (4.70).

$$\eta = \frac{P_{out}}{P_{in}} \tag{4.70}$$

The output power is calculated by subtracting the losses from the electromagnetic power P_{em},

$$P_{out} = P_{em} - P_c - P_{pm} - P_{fr} - P_{wind} \tag{4.71}$$

where P_c are the core losses, P_{pm} are the permanent magnet losses, P_{fr} are the friction losses, and P_{wind} are the windage losses.
The input power is calculated as in (4.72)

$$P_{in} = P_{em} + P_a \tag{4.72}$$

where P_a are the winding losses.

4.5 Comparison study

A comparison study is conducted between the motor scaling approaches based on the categories mentioned in Table 4.1. A brief explanation of the categories are given below:

- **Initial efficiency map**: The requirement of a reference efficiency map, which is obtained from experimental measurements or FEM calculations, to estimate the scaled motor performances is checked.
- **Dimensional scaling**: The possibility of obtaining the geometrical information of the scaled motor is assessed.
- **Accuracy.** A subjective measure on the accuracy of the models in creating the efficiency maps (in Fig. 4.8 and Fig. 4.9) is discussed with respect to FEM-based Motor-CAD models.
- **Calculation time.** The time required to create the efficiency map of a scaled motor is studied. A model with reasonable accuracy and minimum calculation will be considered for the optimisation.

The reference machine in Table 3.1 that produces 47.5 kW is scaled-up to give 52.2 kW. The efficiency maps of the reference and scaled machines are created using FEM based Motor-CAD software [103] and compared with that of the considered methods in Fig. 4.8 and Fig. 4.9. From the comparison made in Table 4.1, it can be observed

Table 4.1: *Comparison of motor scaling approaches*

Motor model	Initial efficiency map	Dimensional scaling	Accuracy	Calculation time
Proportional scaling of efficiency map	Yes	No	Reasonably accurate only in the vicinity of the reference motor	0.2 sec
Willans line model	Yes	Yes, axial and radial scaling	Limited accuracy	0.5 sec
Scalable saturated motor model	No	Yes, axial, radial, and winding scaling	High accuracy related to FEA calculations	1.5 sec
Analytical motor model	No	Yes	Limited accuracy due to exclusion of iron saturation in linear modelling	0.55 sec

that the analytical motor model allows dimensional scaling without requiring the initial efficiency map and provides reasonable accuracy with acceptable calculation time. The air-gap field solutions of the scaled motors, calculated by the analytical model, can also be used for the acoustic performance estimation. Hence, the analytical motor model is considered for the in-wheel motor electric vehicle optimisation in Chapter 8.

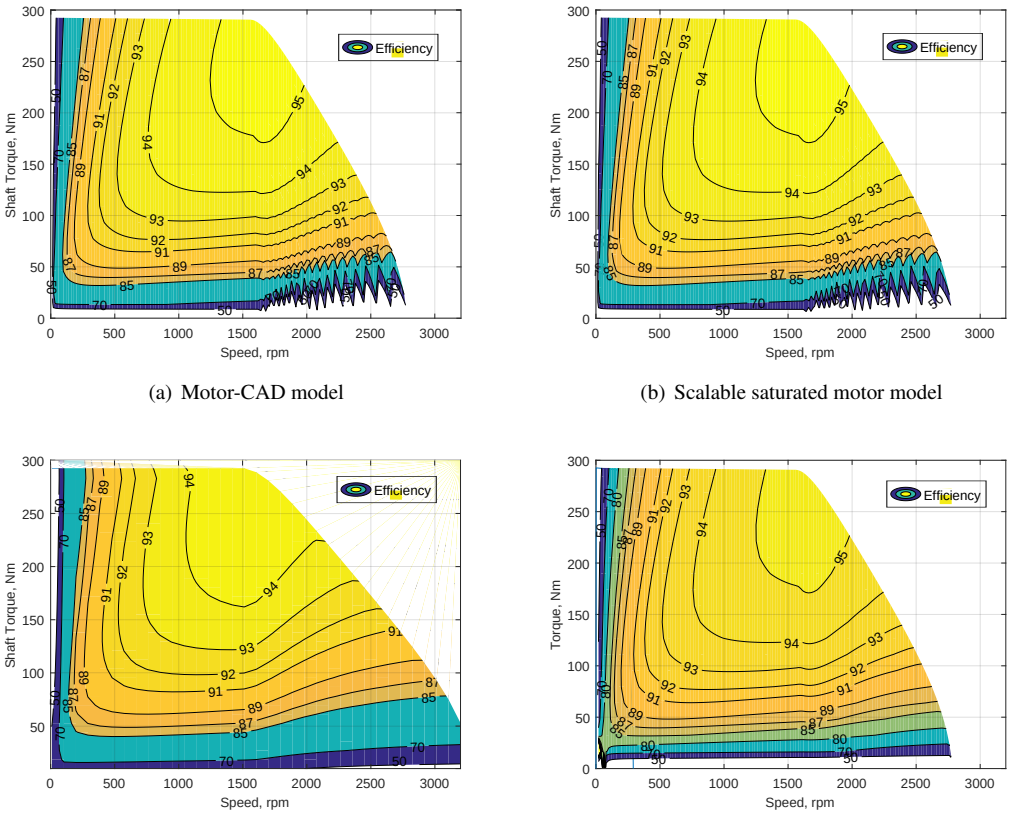

(a) Motor-CAD model

(b) Scalable saturated motor model

(c) Analytical motor model

(d) Willans line model

Fig. 4.8: *Comparison of reference motor efficiency maps.*

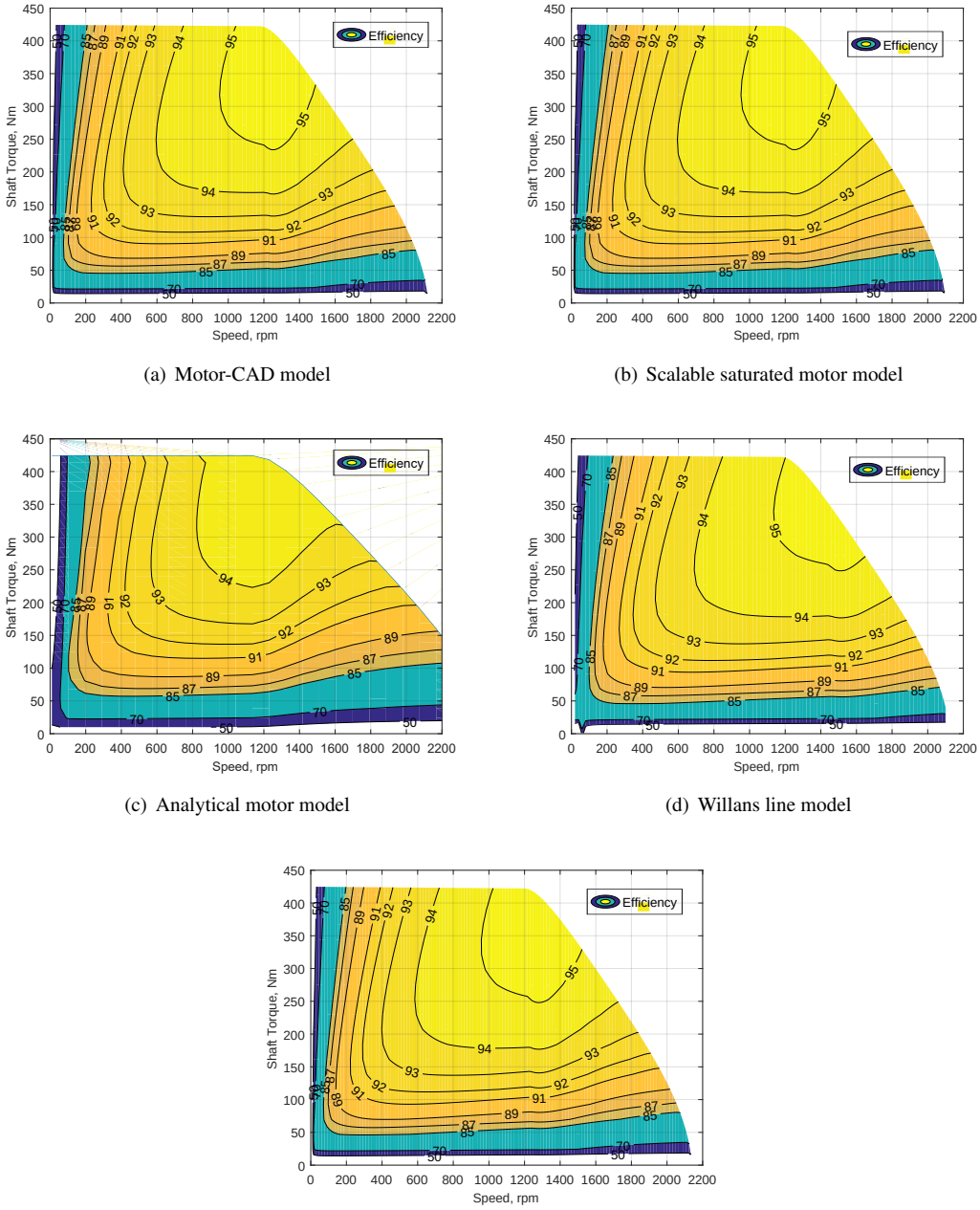

(a) Motor-CAD model

(b) Scalable saturated motor model

(c) Analytical motor model

(d) Willans line model

(e) Proportional scaling of efficiency map

Fig. 4.9: *Comparison of scaled motor efficiency maps.*

CHAPTER 5

Thermal model

In this chapter, the influence of magnet and winding temperatures on the efficiency calculation of an outer rotor SPM machine is analysed using a coupled electromagnetic-thermal model. A thermal model based on lumped parameter thermal networks is built using the distributed loss and capacitance (DLC) element as proposed in [52]. The network is solved by introducing the losses obtained from the electromagnetic model and considering the effect of rotational speed on some of the boundary conditions. The temperature affects the properties of the magnet and winding in the machine. The radially magnetised neodymium magnet is used in the SPM machine, and its remanence reduces with increasing temperature until a maximum allowable point, above which demagnetisation of the magnet occurs. On the other hand, the temperature rise increases the contribution of DC losses in the total winding losses but reduces the AC losses. The coupled electromagnetic-thermal model discussed in this chapter accounts for these effects allowing efficient, due to the reduced computational effort, and improved estimation of the machine losses and performance.

The study is extended to driving cycle analysis where the energy consumption calculation in the NEDC is performed. The benefit of having the thermal model is quantified in percentage difference between the calculated energy consumptions. The coupled model is also used to evaluate the over loading capabilities of the motors.

5.1 Lumped parameter thermal network

Thermal modelling of an electric machine is usually performed by solving the heat equation (5.1) with desired boundary conditions [104].

$$c\dot{T} = k\nabla^2 T + \dot{q} \tag{5.1}$$

where T refers to temperature, c is the product ($c = c_p\eta$) of specific heat capacity (c_p) and mass density (η), k is the thermal conductivity $\left(\frac{\mathrm{W}}{\mathrm{mK}}\right)$, and $\dot{q}$ is the specific heat generation $\left(\frac{\mathrm{W}}{\mathrm{m}^3}\right)$. The thermal model is built based on a lumped parameter thermal network (LPTN) to have reduced computation effort. The LPTN is created by discretising each component of the SPM machine into small elements that are further divided into nodes. The nodes are connected to each other through thermal resistors which simulate heat conduction, convection, and radiation as in Fig. 5.1. Hence, the equation (5.1) can be rewritten (5.2) as

$$C\dot{T} = \frac{\triangle T}{R_{cond}} + \dot{Q} \tag{5.2}$$

where R_{cond} is the conductive thermal resistance [52] and $\triangle T$ is the temperature gradient between the neighbouring nodes. The temperature of each node is estimated using (5.2) and the central node, in Fig. 5.1, provides the average temperature of the element when the Biot number ($Bi = (l_{ref}h)/k$, where h is the heat transfer coefficient and l_{ref} is the reference length associated with the element) is less than 0.1.

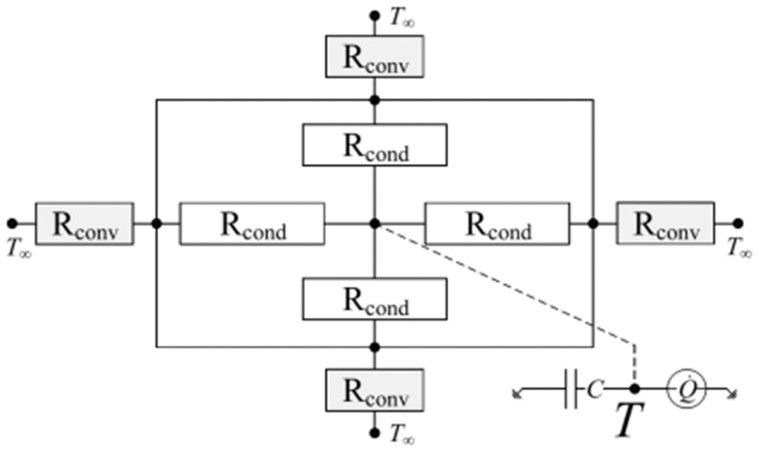

Fig. 5.1: *Classic element discretisation using a lumped parameter thermal network (LPTN)*

Since this condition is not satisfied in all the elements, e.g. the end winding where the convective heat transfer changes with the rotor speed, the machine should be discretised

using the DLC element [105]. As shown in Fig. 5.2, the element is divided into five nodes where the losses and the capacitance are injected according to the ratios given in (5.3) and (5.4) respectively.

$$\dot{Q}_c = 0.6\dot{Q}, \quad \dot{Q}_i = 0.4\frac{A_i}{A_{ext}}\dot{Q} \tag{5.3}$$

$$C_c = 0.6C, \quad C_i = 0.4\frac{A_i}{A_{ext}}C \tag{5.4}$$

where the subscripts c and i represent the central node and i^{th} node on the edge of the element respectively, and A_i is the area exposed to convection that is captured by the i^{th} node. As explained in [52], this discretisation approach estimates the central element temperature directly and accurately. Moreover, the accuracy of this estimation is good over a large range of Bi, up to $Bi = 2$ [106].

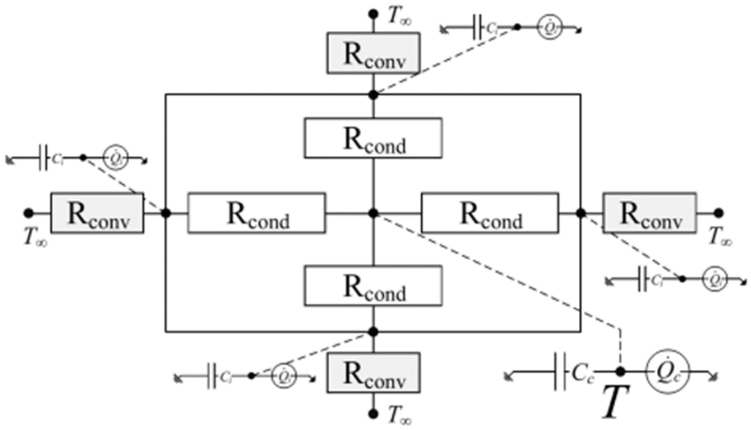

Fig. 5.2: *The distributed loss and capacitance (DLC) element*

Following this discretisation approach, the LPTN of the SPM machine is created as depicted in Fig. 5.3, where a single slot of the machine is shown. The figure indicates how the machine is discretised using rectangular elements in the r-θ plane, and axisymmetric cylindrical elements in the r-z plane. The machine is cooled with a peripheral water jacket where the water is running tangentially to the stator inner surface. The coolant is a 50% water-glycol mixture flowing in four parallel channels of the water jacket. The windings are potted with high thermal conductive epoxy for the improved thermal performance of the machine, and they are homogenised following the method presented in [107]. The thermal resistors in the network are calculated from the motor geometry and material properties. Further details regarding the thermal resistors and modelling of conduction and convection heat transfers are provided in [52].
There are various approaches for solving the LPTN network presented. Object-oriented software such as Matlab Simulink and Modelica [108, 109] is normally preferred, since

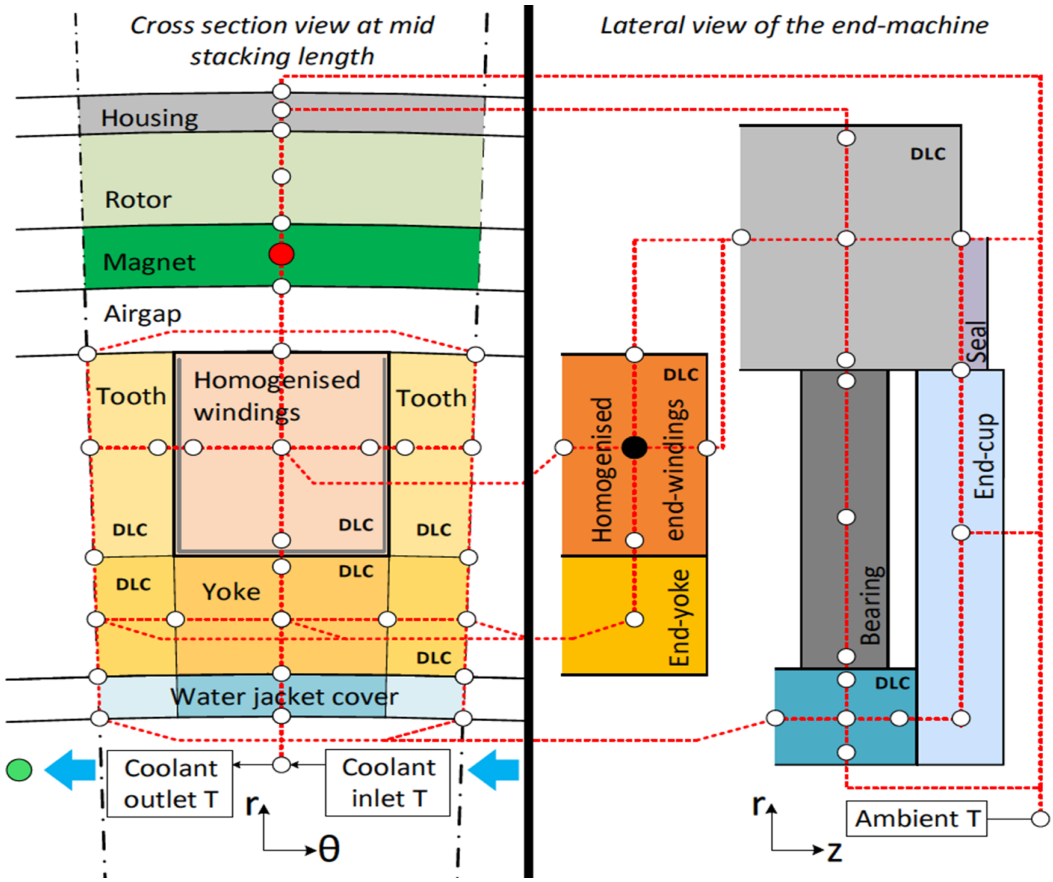

Fig. 5.3: *SPM machine nodal discretisation using the DLC element*

the network can be built using the available elements in their libraries. However, in order to reduce the computation time as much as possible, the linear system of equations can be written directly in Matlab to avoid the pre-calculations required by the object-oriented software. The steady-state temperatures of the machine can be obtained by solving the system in (5.5), which is derived from (5.2),

$$[G][T] = -[\dot{Q}] \tag{5.5}$$

where $[\dot{Q}]$ is the heat input vector including all the nodal losses and boundary conditions, $[T]$ is the temperature vector with m unknowns (number of nodes), and $[G]$ is the symmetric conductance matrix ($m \times m$) containing the diagonal elements $G_{i,i} = \sum_j 1/R_{i,j}$ and the remaining elements $G_{i,j} = -1/R_{i,j}$. The term $R_{i,j}$ represents the thermal resistance between the i^{th} and j^{th} nodes. In order to integrate the system in time, the backward Euler method is implemented to ensure numerical stability. The capacitance matrix $[C]$ is built with the nodal thermal capacitances along the diagonal; the time integration is performed with a fixed time step δ (e.g. 1 sec) as

$$[C]\frac{[T]^{\tau}-[T]^{\tau-1}}{\delta}=[G][T]^{\tau}+[\dot{Q}] \tag{5.6}$$

where τ generic time instant. At each time step the vector $[Q]$ is updated depending on the nodal temperatures, e.g., the winding losses that changes conductor resistance. The same effects can be included in (5.5) with a few iterations of the solution.

5.2 Model validation

The experimental validation is based on DC excitation of the phases in locked rotor condition. Due to the presence of the water jacket, the heat flow occurs mainly from the windings to the coolant, which also implies that the winding temperature is not significantly influenced by the rotational speed of the motor. The accuracy of the model is confirmed for different coolant flow rates and current values, so the model can be used to estimate the winding temperature in the quasi-static analysis of a driving cycle. As an example, the results for the case of $11\,\mathrm{l/min}$ are presented in Fig. 5.4 and Fig.5.5. In Fig. 5.5, the measured and simulated temperatures of the end-windings are compared. The thermistors (NTC sensors with the accuracy $0.1^{o}\mathrm{C}$) are embedded between the end-winding wires before the epoxy resin cures. Whereas in the simulations, the node is selected in the middle of the end-winding; highlighted with a black dot in Fig. 5.3. The comparison was performed at two different mechanical angles: one at the coolant inlet (0^{o}) and the second one at 270^{o} along the coolant flow path. In order to estimate the temperatures at different mechanical angles, the network in Fig. 5.3 was solved by considering appropriate coolant inlet temperature. From the heat flux ($\dot{Q}_{w}$) removed by the coolant at the 0^{o} slot, the coolant temperature rise can be obtained using (5.7), where $\dot{m}$ and $c_{p.w}$ are the coolant mass flow rate and specific heat capacity respectively.

$$\triangle T_{slot}=\frac{\dot{Q}_{w}}{\dot{m}c_{p.w}} \tag{5.7}$$

Assuming that the temperature increases linearly along the water jacket, the coolant inlet temperature at slot s is obtained from the expression $T^{s}_{w,inlet}=s\triangle T_{slot}+T_{w,inlet}$. The coolant temperature at the water jacket outlet is calculated by setting s=120, which is the number of stator slots as given in Table 3.1. The simulated and measured coolant temperatures, at the inlet and outlet, are shown in Fig.5.5. It can be observed that the inlet coolant temperature is assumed to be constant in the simulation. The comparisons presented in Fig. 5.4 shows a good correspondence between the simulation and measurement results in transient and steady-state. The error in the steady state end-winding temperature estimation lies within 5%. The error observed in the estimated

outlet coolant temperature, in Fig.5.5, is mainly due to the assumption of the constant inlet temperature instead of using the measurement data in the calculation. The magnet temperature estimation is not validated in this analysis.

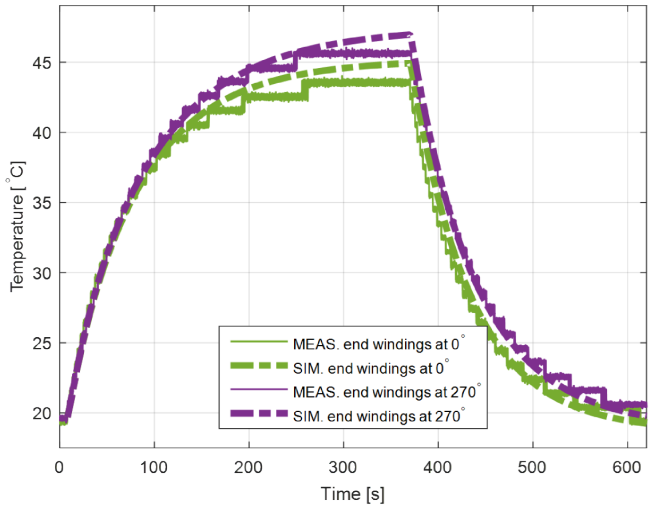

Fig. 5.4: *Comparison between measured and simulated temperatures for the 140 A DC test with coolant flow at* $11\,\mathrm{l/min}$ *in end windings at* θ^o *and* 270^o *mechanical degrees.*

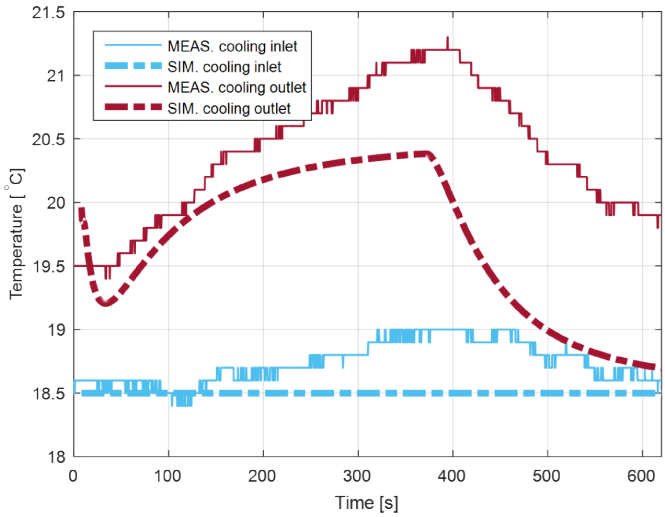

Fig. 5.5: *Comparison between measured and simulated temperatures for the 140 A DC test with coolant flow at* $11\,\mathrm{l/min}$ *at inlet-outlet sections of the cooling water jacket.*

5.3 Improved Efficiency Map and Loss calculations

The efficiency map is developed by calculating the losses at every torque T and speed Ω combination in the torque-speed plane. The iron losses, friction losses and windage losses can be calculated from the operating speed of the motor, but the magnet and copper losses are also functions of stator current which should be derived based on the electromagnetic torque. As the electromagnetic torque is also derived from the losses, the problem is formulated as a minimisation problem given in (4.40) and solved using MATLAB's fmincon function.

The thermal model captures the changes in magnet remanence and conductor resistance that affects the accuracy of efficiency calculation. The efficiency map in Fig. 5.6 is obtained considering the constant temperature of $20^o\mathrm{C}$ for all the operating points. On the other hand, the efficiency map in Fig. 5.7 is calculated after achieving the steady-state temperatures for magnet and winding at every operating point. The reasons for the mismatch is analysed in detailed by performing a comparison study of losses.

The armature resistance increases with speed due to skin effect at low temperature, so the copper losses also increase with speed as shown in Fig. 5.8. At high temperatures the contribution of AC losses reduces, but overall the copper losses throughout the torque-speed plane in Fig. 5.9 increase as the permanent magnet flux linkage reduces in the d axis.

The hysteresis loss component in iron loss calculation is modelled as a function of speed while the eddy current loss component varies with the square of speed. The same trend is observed in both Figs. 5.10 and 5.11, but the increased magnet temperature at high speeds decreases the flux in the stator as well as the iron losses.

5.4 Driving cycle analysis

As the efficiency maps computed in the previous section show some differences, the influence of temperature on the real world operation of the motor should be understood. Therefore, the dynamic change of magnet and winding temperatures in the New European Driving Cycle (NEDC) and its impact on the energy consumption are analysed. The vehicle parameters considered in the analysis are defined in Table 5.1. The torque demand at the wheel (T_{DC}) is computed using (5.8) as a sum of aerodynamic resistance, gradient force, rolling resistance and inertial force. The required output torque of the motor is half of the torque demand since there are two motors in the vehicle.

$$T_{DC} = \left(m_v a + m_v g \sin\alpha + m_v g C_r \cos\alpha + \frac{1}{2} C_d \rho_0 A v^2 \right) R_w \tag{5.8}$$

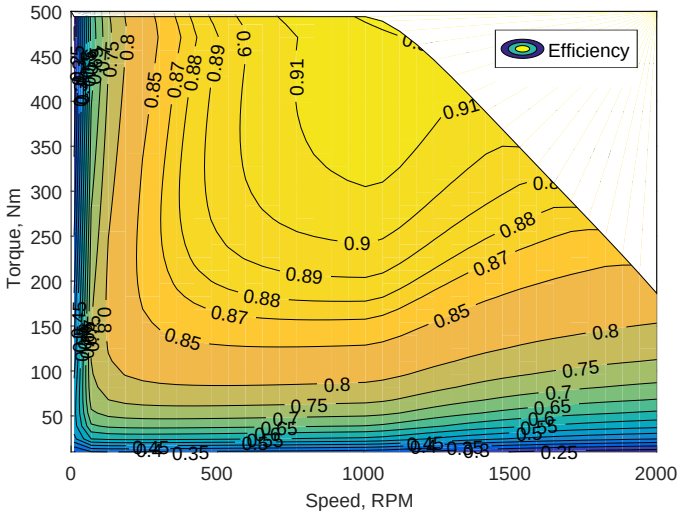

Fig. 5.6: *Efficiency map calculated with a fixed temperature* (20^{o}C) *for magnet and winding on the complete torque-speed plane*

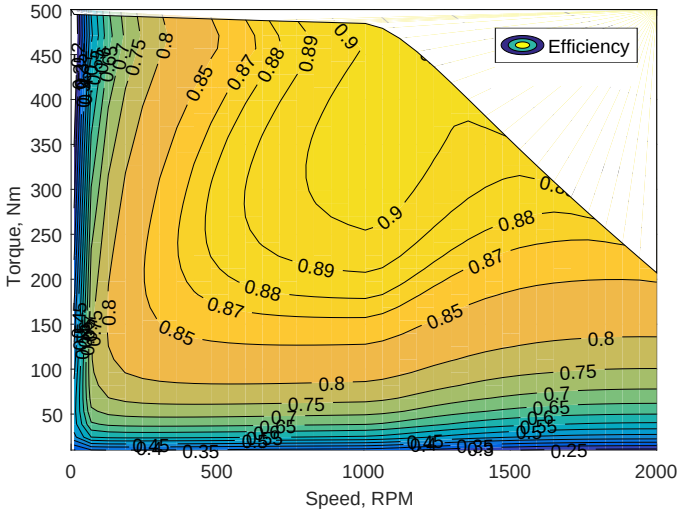

Fig. 5.7: *Efficiency map calculated with steady state temperature for magnet and winding at every operating point*

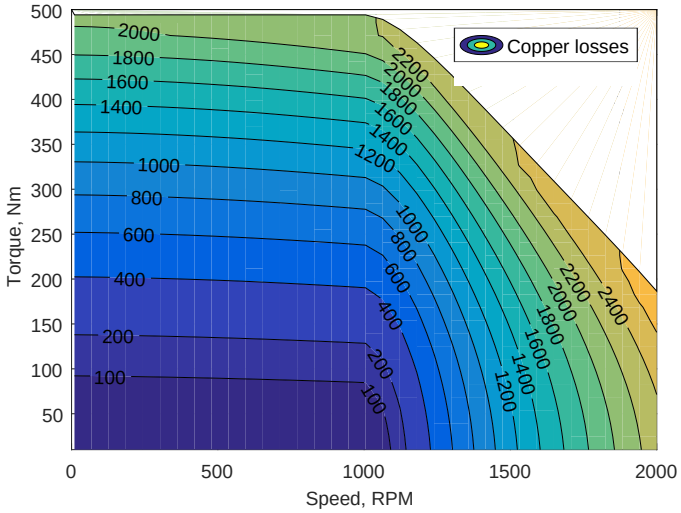

Fig. 5.8: *Copper losses (W) calculated with a fixed temperature* (20^{o}C) *for magnet and winding on the complete torque-speed plane*

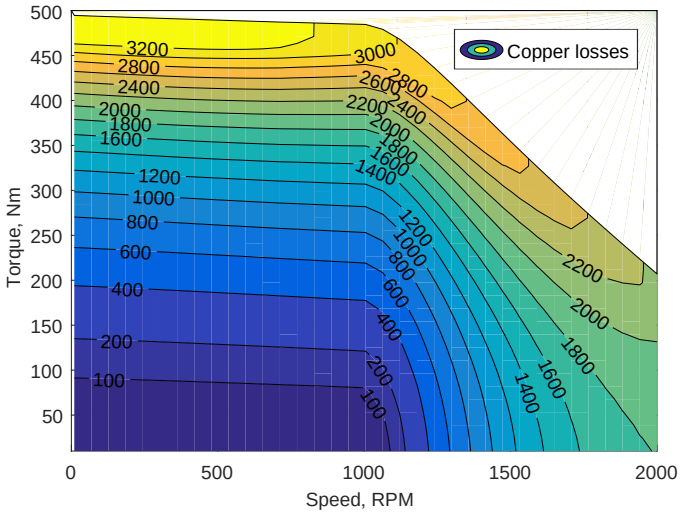

Fig. 5.9: *Copper losses (W) calculated with steady state temperature for magnet and winding at every operating point*

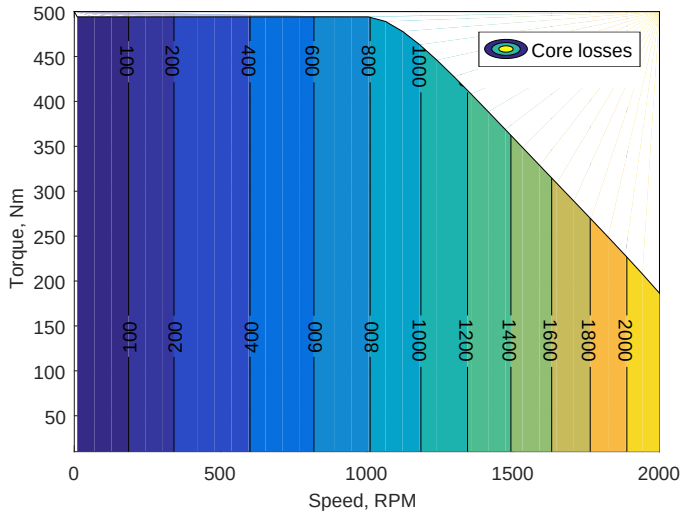

Fig. 5.10: *Iron losses (W) calculated with a fixed temperature (20^{o}C) for magnet on the complete torque-speed plane*

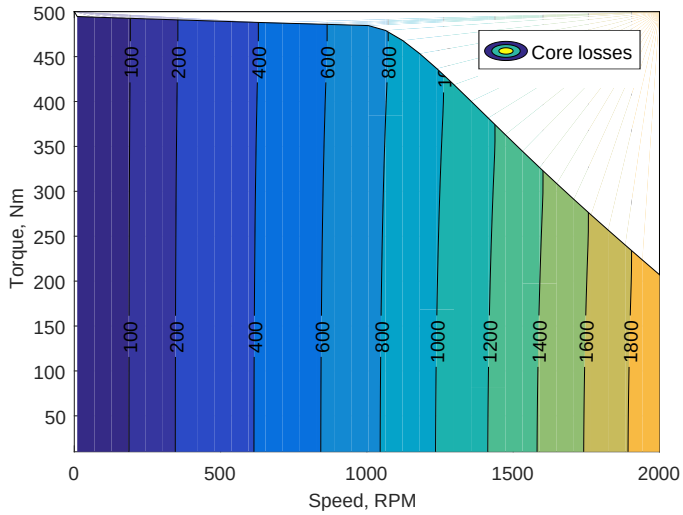

Fig. 5.11: *Iron losses (W) calculated with steady state temperature for magnet at every operating point*

The motor speed (Ω) is obtained from the reference speed of the vehicle in the driving cycle.

$$\Omega = \frac{v}{R_w} \tag{5.9}$$

Table 5.1: *Vehicle Parameters*

Parameters,	Symbol,	Value,	Unit
Vehicle curb weight + driver	m_v	2000+75	kg
Frontal area	A	2	m^2
Wheel radius	R_w	0.32	m
Rolling resistance coefficient	C_r	0.01	-
Drag coefficient coefficient	C_d	0.4	-
No of in-wheel motors	-	2	-
Gradient	α	0	degrees
Air density	ρ_0	1.29	$\mathrm{kg/m}^3$

In the generating mode, the electrical machine input power (P_{in}) is defined by subtracting the machine losses from the traction power available at the wheel as in (5.10).

$$P_{in} = T_{sh}\Omega - (P_a + P_c + P_{PM} + P_{ml}) \tag{5.10}$$

The regeneration boundary can be obtained as shown in Fig. 5.12 by assigning $P_{in} = 0$ and by finding the maximum and minimum torque values at each speed numerically using the MATLAB fmincon function [110].

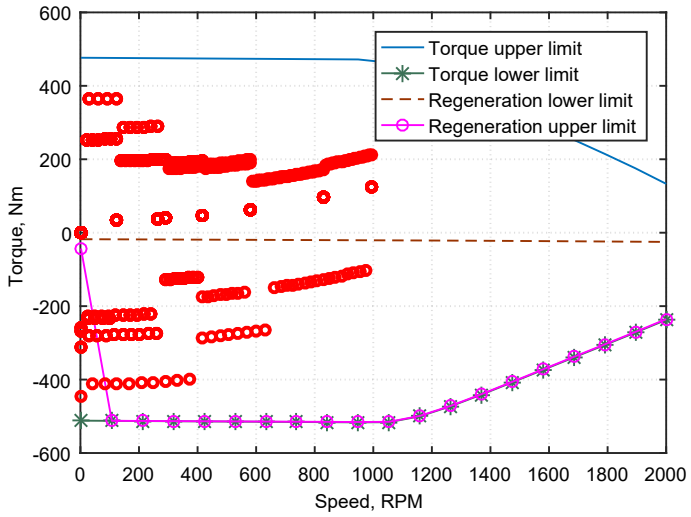

Fig. 5.12: *NEDC operating points in different regions of motor operation*

When the motor operating points (T_{DC}, Ω) in NEDC, marked with red circles in Fig. 5.12, are in the region between the upper limit of regeneration and the torque axis, the required braking torque is given by mechanical brakes. Brake blending is not considered in this region. On the other hand, when the operating points are between upper and lower limits of the regeneration, the required braking torque is given by the electric motor itself. The battery is assumed to absorb all the recuperated energy from the motor.

Electric power at the motor input terminal is summed over the NEDC to get the net energy consumption. The analysis was repeated with and without the thermal model, and the results are given in Table 5.1. The difference in the calculated values of energy consumption can be minimised by considering average temperature in the driving cycle for magnet and winding without the thermal model. Considering that the tractive power is same in these analyses, the difference is caused only due to the variations in the motor losses. The study is repeated with different vehicle parameters as shown in Table 5.2. Therefore, it is safe to use the average magnet and winding temperature values for the energy consumption calculations during optimisation process [46].

Table 5.2: *Energy consumption in New European Driving Cycle with two different vehicle weights*

Vehicle weight	$m_v = 2075kg$	$m_v = 1875kg$
Energy consumption without thermal model	6.33 MJ	6.01MJ
Energy consumption along with thermal model	6.46 MJ	6.12MJ
Energy consumption considering average temperature in driving cycle without thermal model	6.43 MJ	6.08MJ

5.5 Overloading capability study

Using the coupled electromagnetic-thermal model, it is also possible to study the overloading capability of the electric motor for a short period. For the considered SPM machine, the temperature evolution on a particular operating condition (Torque 300Nm and speed 1000 RPM) is plotted for 20 sec in Fig. 5.13. The temperatures at the centre of the end-winding and magnet (black and red nodes in Fig. 5.3 respectively) are studied. During this transient analysis, the properties of the magnet and winding are updated at every time step. A heat exchanger in the thermal management system is used as an ideal component to reject a fixed amount of heat (2 kW) from the coolant. Based on the results of this model, the motor performance can be limited when the temperatures go beyond the acceptable limit.

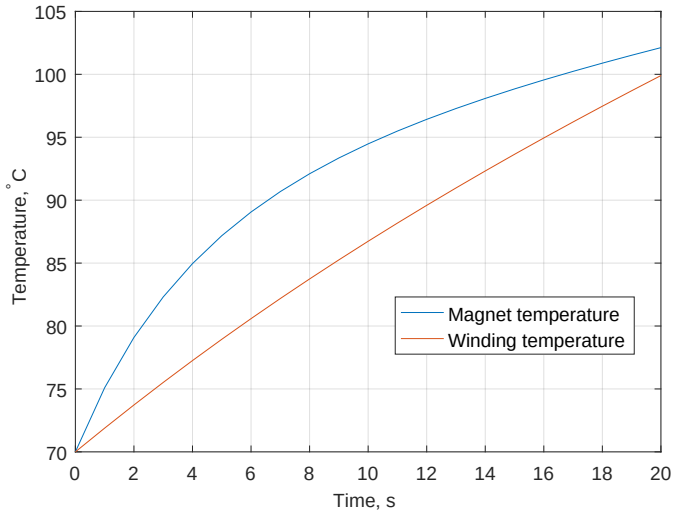

Fig. 5.13: *Evolution of magnet and winding temperatures of the motor operating at Torque 300Nm and speed 1000 RPM*

This model is used to evaluate the gradability of vehicles in the optimisation of in-wheel motor electric vehicles in Chapter 8.

CHAPTER 6

Acoustic model

The permanent magnet machines exhibit low noise compared to their counterparts used in similar applications. Although the noise is a subjective measure, an understanding of the machine's acoustic performance can be useful in the early optimisation process. In this chapter, the radial electromagnetic force, which is one of the main sources of the noise, is considered for estimation of the sound pressure level (SPL). The mechanical bearing forces are not considered here. In the case of external rotor in-wheel motors, the noise source (rotor) is rotating. However, the maximum rotation frequencies in these machines ($\leq$ 25 Hz) are considerably lower than the structural frequencies ($\geq$ 400 Hz). Therefore, the rotor can be assumed as a stationary member [53]. The standard acoustic models of inner rotor machines can be adapted here.

6.1 Radial electromagnetic force calculation

The air-gap field solution under load condition is calculated by adding the contributions from the permanent magnet in (A.5)-(A.6) and the armature winding in (B.26)-(B.27).

$$B = B_r + jB_\theta = (B_{sr} + B_{ar}) + j(B_{s\theta} + B_{a\theta}) \tag{6.1}$$

which can be written in the form

$$\vec{B} = B_r\vec{a_r} + B_\theta\vec{a_\theta}. \tag{6.2}$$

The radial forces distribution along the air-gap centre can be calculated from the Maxwell stress tensor [111] given in (6.3).

$$\vec{t_m} = \left(\vec{n}\frac{\vec{B}}{\mu_0}\right)\vec{B} - \vec{n}\frac{1}{2}\frac{|\vec{B}|^2}{\mu_0} \tag{6.3}$$

By substituting (6.2) in (6.3), the radial and tangential components of the stress tensor can be derived.

$$\vec{t_m} = \frac{1}{\mu_0}\left(B_r^2 - \frac{1}{2}|\vec{B}|^2\right)\vec{a_r} + \frac{1}{\mu_0}B_r B_\theta \vec{a_\theta} \tag{6.4}$$

The radial component of the stress tensor is multiplied with stack length l_a, air-gap centre radius $(R_{mag}+R_s)/2$, and discretisation angle $d\theta$ to get the radial force distribution. Figure 6.1 gives the radial force distribution in a single pole pitch over a time period.

$$F_r = \frac{l_a(R_{mag}+R_s)d\theta}{2\mu_0}\left(B_r^2 - \frac{1}{2}|\vec{B}|^2\right) \tag{6.5}$$

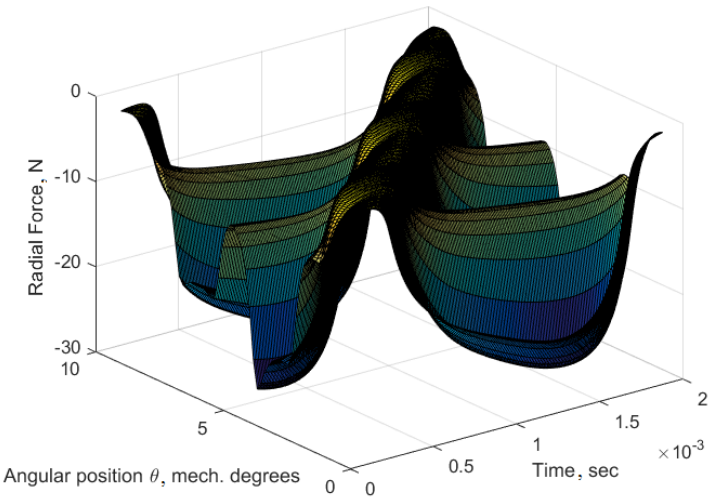

Fig. 6.1: *Radial force distribution in space and time domain calculated at 800 RPM with I_d=0 and I_q=150 A.*

6.2 Vibro-acoustic modelling

Modal characteristics of the radiating outer rotor is calculated analytically using a ring model [54] that defines the natural frequencies f_n as,

$$f_n = \begin{cases} f_0 = \frac{1}{2\pi R_m}\sqrt{\frac{E}{\Delta\rho}} & \text{for } n = 0 \\ f_1 = f_0\sqrt{\frac{2}{1+k^2}} & \text{for } n = 1 \\ f_0 k\frac{n(n^2-1)}{\sqrt{n^2+1}}\frac{1}{\sqrt{1+k^2\left(\frac{n^2-1}{n^2+1}\right)[3+5n^2]}} & \text{for } n \geq 2 \end{cases} \tag{6.6}$$

where n represent the circumferential bending modes of the rotor, E is Young's modulus of the core and ρ is the mass density. The parameter k related to the machine geometry is described as follows,

$$k = \frac{1}{2\sqrt{3}} \frac{h}{R_m} \tag{6.7}$$

where h is the rotor yoke height and R_m is the rotor mean radius.

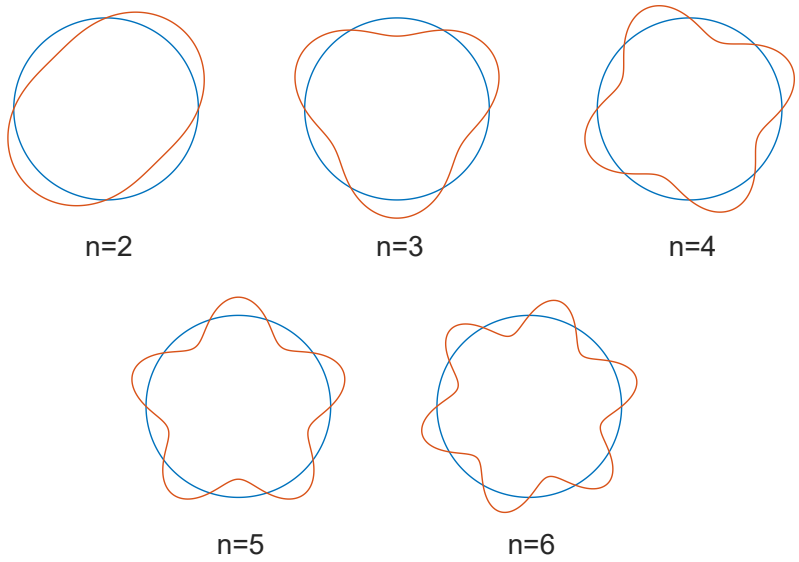

Fig. 6.2: *Illustration of cylindrical modes*

In the considered motor, the rotor is press-fitted to the housing. Hence, the proposed study emulates this interaction using proper equivalent parameters which are estimated from a two-step process summarised in Fig. 6.3. Firstly, the machine geometry in Fig. 6.3 (a) with complex details of the rotor and housing is simplified to an equivalent two cylinder model as in Fig. 6.3 (b). Then it is further simplified to an equivalent ring model in Fig. 6.3 (c) using weighted average method combined with model and physical insights. Considering only the radial bending, the rotor and housing thicknesses determine the equivalent Young's modulus E_{eq} as

$$E_{eq} = \frac{(R_{outer,r} - R_{inner,r})E_r + (R_{outer,h} - R_{outer,r})E_h}{(R_{outer,h} - R_{inner,r})}. \tag{6.8}$$

The equivalent outer radius $R_{outer,eq}$ is kept same as the outer radius of the housing $R_{outer,h}$ since it corresponds to the radiating surface. The equivalent mean radius $R_{eq} = (R_{inner,eq} + R_{outer,eq})/2$ which contributes to the ring stiffness in equation (6.6), can be derived as

$$R_{eq} = \frac{1}{2}\frac{(R_{inner,r} + R_{outer,r})E_r + (R_{outer,r} + R_{outer,h})E_h}{(E_r + E_h)}. \tag{6.9}$$

The ring length influences the system dynamics only through the change in mass. Therefore it is defined as a simple average of the rotor and housing lengths: $l_{eq} = (l_a + l_h)/2$. The equivalent mass density is derived logically from the fact that the total system mass should be equal in both cases.

$$\rho_{eq} = \frac{\rho_r l_a (R^2_{outer,r} - R^2_{inner,r}) + \rho_h l_h (R^2_{outer,h} - R^2_{outer,r})}{l_{eq}(R^2_{outer,eq} - R^2_{inner,eq})} \tag{6.10}$$

Finally, it is important to mention that the Poisson ratio for the equivalent system is not parametrised since no shear is involved in the model. The parameters of the simplified model, given in Table 6.1, E_i, ρ_i, ν_i, l_i, $R_{inner,i}$, $R_{outer,i}$ represent the Young's modulus (MPa), the mass density (kg/m^3), the Poisson ratio, the axial length (m), the inner and outer radii (m) respectively. The subscript r, h and eq stand for the rotor, housing and equivalent ring.

Table 6.1: *Equivalent parameter estimation process*

Model	Material	Geometry	N_{ip}
A	$E_r, \rho_r, \nu_r, E_h, \rho_h, \nu_h$	Rotor mesh, Housing mesh	thousands
B	$E_r, \rho_r, \nu_r, E_h, \rho_h, \nu_h$	$l_a, R_{inner,r}, R_{outer,r}, l_h, R_{inner,h}, R_{outer,h}$	11*
C	E_{eq}, ρ_{eq}	$l_{eq}, R_{inner,eq}, R_{outer,eq}$	5

The three first natural frequencies f_n resulted from the ring model are compared with the results of detailed FEM model (Fig. 6.3 (a)) in Table 6.2. Despite the significant assumptions made in the ring model, it gives comparable results.

Table 6.2: *Natural frequencies of the outer rotor*

	Mass [kg]	n^{th} Mode's Frequency [Hz]		
		$n = 2$	$n = 3$	$n = 4$
FE (A)	11.85	444	1229	2300
Analytical (C)	11.57	392	1095	2068
Rel. error (%)	2.36	11.71	10.90	10.09

The radial force distribution F_r is calculated at all the rotational speeds $\Omega_n = \frac{60 f_n}{np}$ (RPM) corresponding to the resonance frequencies that are below the considered maximum speed of the motor. The sound pressure level is computed at all the resonant speeds and averaged.

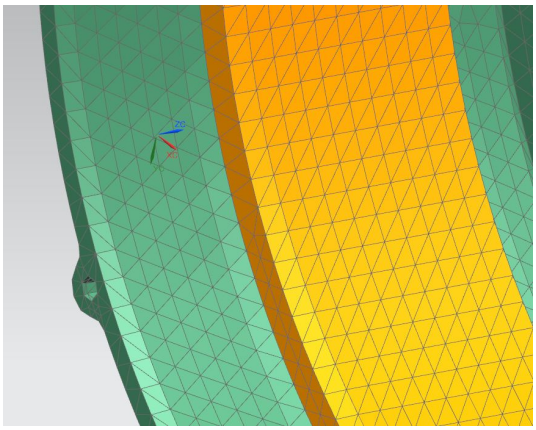

(a) Model A - Detailed FE model

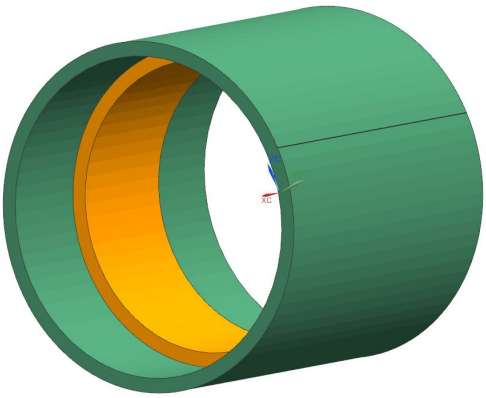

(b) Model B - Equivalent two-cylinder model

(c) Model C - Equivalent ring model

Fig. 6.3: *Equivalent parameter estimation process*

From the natural frequencies of the ring model, one can calculate the vibration displacement amplitude Y_n at each mode n considering the excitation force in (6.5) [54, 55].

$$Y_n = \begin{cases} \frac{R_{inner,eq}R_{eq}}{E_{eq}h}\frac{F_{r,n}}{2\pi R_{eq}leq}\eta_n & \text{for } 0 \leq n \leq 1 \\ \frac{R_{inner,eq}R_{eq}}{E_{eq}h}\left[\frac{1+3k^2(k^2-1)}{k^2(k^2-1)^2}\right]\frac{F_{r,n}}{2\pi R_{eq}leq}\eta_n & \text{for } n \geq 2 \end{cases} \tag{6.11}$$

$F_{r,n}(\omega)$ is the n^{th} spatial-harmonic amplitude of the radial force F_r and η_n is the resonance factor for the same harmonic,

$$\eta_n = \frac{1}{\sqrt{\left(1-\left(\frac{\omega n,F}{\omega_n}\right)^2\right)^2 + \left(\frac{2\xi\omega_{n,F}}{\omega_n}\right)^2}} \tag{6.12}$$

where $\omega_{n,F}$ is the time-harmonic frequency and ξ_n is the damping factor i.e. 1%. It can be noticed that when the force and mode shape meet the same spatial distribution at the same frequency with no damping i.e. $\omega_{n,F} = \omega_n$ and $\xi_n = 0$, η_n goes to infinity which gives an infinite displacement; a resonance effect.

The sound radiator considered in the acoustic model is an infinite cylinder. The sound pressure p at a distance r and an angle θ from the radiating surface is determined in the time domain by the summation of negative and positive rotating vibration waves coming from each mode n [112].

$$p(r,\theta,t) = \sum_{n=-\infty}^{+\infty} p_n(r,\omega)\exp(jn\theta)\exp(j\omega t) \tag{6.13}$$

where $p_n(r,\omega)$ is given for an infinite cylinder radiator as,

$$p_n(r,\omega) = -\frac{j\rho_0 c}{\frac{dH_n^{(2)}(k_0 r_0)}{d(k_0 r_0)}} H_n^{(2)}(k_0 r) v_n(\omega) \tag{6.14}$$

In the above equation, ρ_0 is the air mass density, c is the sound velocity in the air, $H_n^{(2)}$ is the Hankel function of the second kind and $k_0 = \omega/c$ is the acoustic wave number. The n^{th} spatial-harmonic velocity amplitude v_n contributing to the total particle velocity corresponds to the radial velocity of the radiating surface.

$$v_n(\omega) = j\omega Y_n \tag{6.15}$$

Finally, the sound pressure level (SPL) L_p can be calculated at the operating speed of Ω_n using the well-known formula

$$L_{p,\Omega_n} = 20log_{10}\left[\frac{p_{RMS}}{2.10^{-7}}\right] \quad \text{in dB.} \tag{6.16}$$

and the logarithmic average of SPLs at different resonant speeds is considered for evaluating the acoustic performance of the machine.

$$L_p = 10log_{10}\left(\frac{\sum_{i=1}^{N_n} 10^{\left(\frac{L_{p,\Omega_i}}{10}\right)}}{N_n}\right) \quad \text{in dB} \tag{6.17}$$

where N_n is the total number of excited modal frequencies within the operating speed range of the machine. The reference machine geometry, given in Table 3.1, is scaled in axial and radial directions (maximum of 20%), and the SPL is calculated for each motor candidate. Figure 6.4 presents the SPL as a function of the scaling ratios.

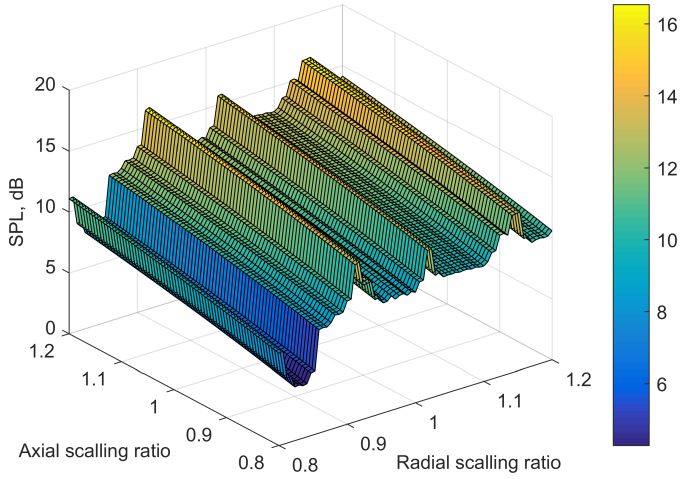

Fig. 6.4: *Sound pressure level in dB*

This approach will be adopted for evaluating the acoustic performance of the motors while optimising the in-wheel motor electric vehicle in Chapter 8.

CHAPTER 7

Suspension model

The increased unsprung mass of the in-wheel motor electric vehicles has a negative impact on the ride performance. Passive suspension components such as inerter and relaxation spring can be taken into account to improve the dynamic behaviour of the conventional spring-damper suspension. This chapter presents a theoretical evaluation of six suspension architectures which have the spring, damper, inerter, and relaxation spring in different configurations. It is important to understand their performance differences to consider an appropriate design for the vehicle level optimisation. A linear quarter-car model is used to model the vehicle corner considering a random irregular road profile. Three suspension performance indices, namely, discomfort, road holding, and working space are derived analytically. The multi-objective optimisation techniques introduced in Chapter 2 can be used to handle the objective functions simultaneously and to compute of the Pareto-optimal sets. The suspension architectures featuring inerter and/or relaxation spring are compared with conventional passive suspension architecture in the objective functions domain of the Pareto-optimal solutions. In the first part of the chapter, a general approach for deriving the suspension performance indices is explained, and the analytical expressions of the objective functions are presented for all six suspension architectures. In the second part, the multi-objective optimisation is carried out, and the results are compared.

7.1 Mathematical modelling of vehicle suspension system

The simplified quarter-car model, shown in Fig. 7.1, is used for describing the vertical motion of the suspension system due to the road irregularity.

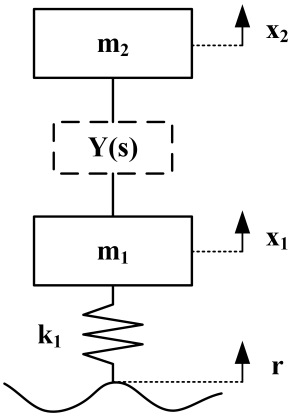

Fig. 7.1: *Quarter car model*

The model contains unsprung mass (m_1), sprung mass (m_2), tire stiffness (k_1), and the suspension. The mechanical admittance ($Y(s)$), i.e. the transfer function between force and relative velocity of m_2 with respect to m_1, depends on the configuration of the suspension.

$$Y(s) = \frac{F_y}{(X_2 - X_1)s} \tag{7.1}$$

Considering the mechanical admittance for the suspension, the general equation of motion for the quarter-car model is written as

$$\begin{aligned} &m_1 s^2 x_1 + k_1(x_1 - r) - sY(s)(x_2 - x_1) = 0 \\ &m_2 s^2 x_2 + sY(s)(x_2 - x_1) = 0 \end{aligned} \tag{7.2}$$

where r is the road irregularity which can be defined using a single slope power spectral density [113].

7.1.1 Suspension architectures

In this study, the suspension architectures, which were introduced in [50], are optimised for the objective functions: discomfort, road holding, and working space. The suspensions consist of spring with stiffness k_2, damper with damping ratio r_2, inerter with equivalent mass m_e, and one additional spring with stiffness k_3 [114]. The architecture S1, shown in Fig. 7.2, represents the conventional parallel spring-damper system and the S2 contains an additional spring in series with the damper. The other architectures have inerter also connected in series or parallel.

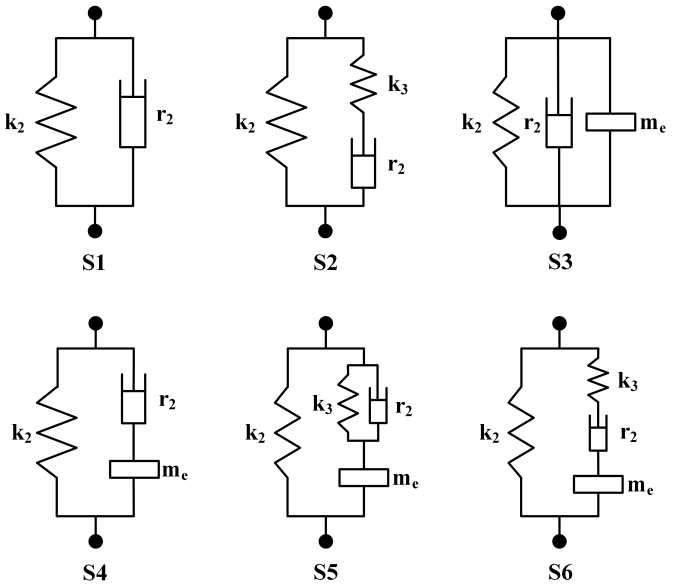

Fig. 7.2: *Suspension architectures.*

The mechanical admittance of these suspension architectures are given below.

$$
\begin{aligned}
\text{S1}: Y(s) &= \frac{k_2}{s} + r_2 \\
\text{S2}: Y(s) &= \frac{k_2}{s} + \left(\frac{s}{k_3} + \frac{1}{r_2}\right)^{-1} \\
\text{S3}: Y(s) &= \frac{k_2}{s} + r_2 + m_e s \\
\text{S4}: Y(s) &= \frac{k_2}{s} + \left(\frac{1}{r_2} + \frac{1}{m_e s}\right)^{-1} \\
\text{S5}: Y(s) &= \frac{k_2}{s} + \left(\frac{s}{k_3 + s r_2} + \frac{1}{m_e s}\right)^{-1} \\
\text{S6}: Y(s) &= \frac{k_2}{s} + \left(\frac{s}{k_3} + \frac{1}{r_2} + \frac{1}{m_e s}\right)^{-1}
\end{aligned}
$$

The equivalent mass m_e of the inerter is derived from its disk mass, radius, and screw lead. An inerter, shown in Fig. 7.3, has a rotating flywheel and a fixed nut [115] where the flywheel consists of a screw and a disk. The energy stored in the rotating flywheel is equal to the energy stored in an equivalent mass moving in a linear direction

$$\frac{1}{2} m_e v^2 = \frac{1}{2} J \omega_f^2 \tag{7.3}$$

where v is the linear velocity of the equivalent inerter mass, $J(= 1/2 m_f r_f^2)$ and $\omega_f(= 2\pi v/p)$ are the rotational inertia and angular velocity of the flywheel respectively.

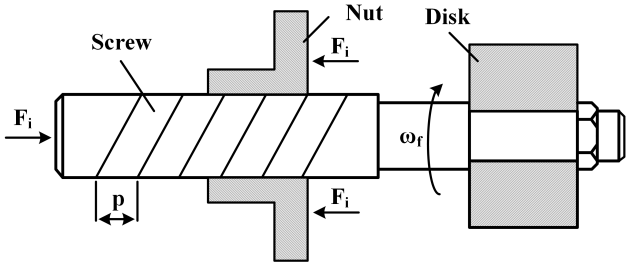

Fig. 7.3: *Configuration of ball-screw inerter.*

Substituting the expression of J and ω in (7.3),

$$\frac{1}{2}m_e v^2 = \left(\frac{1}{2}\right)\left(\frac{1}{2}\right) m_f r_f^2 v^2 \left(\frac{2\pi}{p}\right)^2 \tag{7.4}$$

where m_f is the mass of the flywheel, r_f is the effective radius of the flywheel, and p is the screw pitch.

$$m_e = 2m_f \left(\frac{\pi r_f}{p}\right)^2 \tag{7.5}$$

Thus, the inerter allows to achieve a high inerter equivalent mass with a low disk mass. An inerter with 0.2 kg disc mass, 25 mm radius, and 3 mm screw lead can represent an equivalent mass of 302 kg. The force generated by the inerter is proportional to the relative acceleration between its attachment points [116] [117].

$$F_i = m_e(\ddot{x_2} - \ddot{x_1}) \tag{7.6}$$

7.1.2 Derivation of the objective functions

The objective function discomfort is defined as the standard deviation of the vertical acceleration ($\ddot{x_2}$) of the vehicle body (m_2). The road holding is defined as the standard deviation of the force applied between road and wheel ($k_1(x_1 - r)$). The working space is defined as the standard deviation of the relative displacement between the wheel and the vehicle body ($x_2 - x_1$).

The transfer function between the input road signal and unsprung mass displacement is given by,

$$X_1(s) = \frac{k_1(Y(s) + m_2 s)}{k_1 Y(s) + (m_1 + m_2)Y(s)s^2 + m_2 k_1 s + m_1 m_2 s^3} \tag{7.7}$$

Similarly, the transfer function between the input road signal and sprung mass displacement is given by,

$$X_2(s) = \frac{k_1 Y(s)}{k_1 Y(s) + (m_1 + m_2)Y(s)s^2 + m_2 k_1 s + m_1 m_2 s^3} \tag{7.8}$$

Using the displacements of m_1 and m_2, the vertical acceleration ($\ddot{x}_2$), tyre vertical load (F_z), and working space($x_2 - x_1$) can be derived. The transfer function between r and $\ddot{x}_2$ is calculated as

$$H_1(s) = s^2 X_2(s) \tag{7.9}$$

The transfer function between r and F_z is

$$H_2(s) = k_1(1 - X_1(s)) \tag{7.10}$$

The transfer function between r and $x_2 - x_1$ is

$$H_3(s) = X_2(s) - X_1(s) \tag{7.11}$$

The road irregularity can be modelled using a random variable defined by a stationary and ergodic stochastic process with zero mean value. In this study, a single slope power spectral density has been considered [118].

$$S_r(s) = \frac{A_b V}{s^2} \tag{7.12}$$

where A_b accounts for the road profile. The power spectral density of the output signal for an asymptotically stable system can be computed as [119, 120]

$$S_l(s) = |H_l(s)|^2 S_r(s) = A_b V \left| s^{-1} H_l(s) \right|^2 \tag{7.13}$$

where $l = 1, 2, 3$. The standard deviation of a random variable described by the stationary and ergodic stochastic process [119] is

$$\sigma_l = \left(\frac{1}{2} \int_{-\infty}^{+\infty} S_l(\omega) d\omega \right)^{\frac{1}{2}} \tag{7.14}$$

which can be rewritten [121] as,

$$\sigma_l = (A_b V)^{\frac{1}{2}} \| s^{-1} H_l(s) \|_2 \tag{7.15}$$

The analytical expression for H2 norm of the generic transfer function $s^{-1}H_l(s)$, given in (7.16), can be derived from its state space form.

$$s^{-1} H_l(s) = \frac{b_1 s^{n-1} + ... + b_{n-1} s + b_n}{a_0 s^n + a_1 s^{n-1} + ... + a_{n-1} s + a_n} \tag{7.16}$$

The state space form is

$$\dot{x} = \begin{bmatrix} 0 & 1 & 0 & \cdots & 0 \\ 0 & 0 & 1 & \cdots & 0 \\ \vdots & \vdots & \vdots & \vdots & \vdots \\ -a_n & -a_{n-1} & -a_{n-2} & \cdots & -a_1 \end{bmatrix} x + \begin{bmatrix} 0 \\ 0 \\ \vdots \\ 1 \end{bmatrix} u,$$
$$y = \begin{bmatrix} b_n & b_{n-1} & b_{n-2} \cdots & b_1 \end{bmatrix} x. \tag{7.17}$$

The H2 norm of the transfer function is formulated as a function of the output matrix C in (7.17),

$$\|s^{-1}H_l(s)\|_2 = (CLC^T)^{\frac{1}{2}} \tag{7.18}$$

where the matrix L is the unique solution of the Lyapunov equation as explained in Appendix-A.

$$AL + LA^T + BB^T = 0 \tag{7.19}$$

By substituting the H2 norm of the transfer functions from (7.9) to (7.11) in (7.13) the expression for the objective functions can be derived.

7.1.3 Expressions of the objective functions

The analytical expressions of the discomfort, road holding, and working space are given for all the architectures in this section.

Analytical expression of discomfort

The input parameters m_1, m_2, k_1, A_b, and v are fixed for all the architectures. The generic expression of discomfort for all the architectures is,

$$\sigma_{\ddot{x}_2,Si} = \sqrt{A_b v \overline{\sigma}^2_{\ddot{x}_2,Si}} \tag{7.20}$$

where term $\overline{\sigma}^2_{\ddot{x}_2,Si}$ is expressed for the architecture S1 as:

$$\overline{\sigma}^2_{\ddot{x}_2,S1} = a_1 r_2 + a_2 r_2^{-1}$$

where

$$\begin{aligned} a_1 &= \frac{k_1}{2m_2^2} \\ a_2 &= \frac{(m_1+m_2)k_2^2}{2m_2^2}. \end{aligned}$$

The term $\overline{\sigma}^2_{\ddot{x}_2,S2}$ for the architecture S2 is given as:

$$\overline{\sigma}^2_{\ddot{x}_2,S2} = \sigma^2_{\ddot{x}_2,S1} + (a_3 k_3^{-1} + a_4 k_3^{-2}) r_2$$

where

$$\begin{aligned} a_3 &= \frac{k_1 k_2}{m_2^2} \\ a_4 &= \frac{k_1 k_2^2}{2m_2^2} \end{aligned}$$

The term $\overline{\sigma}^2_{\ddot{x}_2,S3}$ for the architecture S3 is given as:

$$\overline{\sigma}^2_{\ddot{x}_2,S3} = a_1 r_2 + (\frac{a_8 m_e^3 + a_7 m_e^2 + a_6 m_e + a_5}{a_{10} + a_9}) r_2^{-2} \tag{7.21}$$

where

$$\begin{aligned} a_5 &= m_1 m_2 (m_1 + m_2) k_2^2 \\ a_6 &= (m_1 + m_2)^2 k_2^2 - 2 m_1 m_2 k_1 k_2 \\ a_7 &= -2 k_1 (m_1 + m_2) k_2 + m_2 k_1^2 \\ a_8 &= k_1^2 \\ a_9 &= 2 m_1 m_2^3 \\ a_{10} &= 2(m_1 + m_2) m_2^2 \end{aligned}$$

The term $\overline{\sigma}^2_{\ddot{x}_2,S4}$ for the architecture S4 is given as:

$$\overline{\sigma}^2_{\ddot{x}_2,S4} = (a_1 + a_6 m_e^{-1} + a_7 m_e^{-2}) r_2 + a_2 r_2^{-1} \tag{7.22}$$

where

$$\begin{aligned} a_5 &= \frac{(m_1 + m_2) k_2}{m_2^2} \\ a_6 &= \frac{(m_1 + m_2)^2 k_2^2 + k_1 m_2^2 k_2}{2 m_2^2 k_1} \end{aligned}$$

The term $\overline{\sigma}^2_{\ddot{x}_2,S5}$ for the architecture S5 is given as:

$$\overline{\sigma}^2_{\ddot{x}_2,S5} = \overline{\sigma}^2_{\ddot{x}_2,S1} + (a_5 m_e^{-1} + a_6 m_e^{-2}) r_2 + \left((a_7 + a_8 m_e^{-1} + a_9 m_e^{-2}) k_3^{-2} - (a_5 + 2 a_6 m_e^{-1}) k_3\right) r_2^{-1} \tag{7.23}$$

where

$$\begin{aligned} a_7 &= \frac{(m_1 + m_2)}{m_2^2} \\ a_8 &= -\frac{2(m_1 + m_2)^2 k_2 + m_2^2 k_1}{2 m_2^2 k_1} \\ a_9 &= \frac{(m_1 + m_2)^3 k_2^2 + 2 m_2^2 (m_1 + m_2) k_1 k_2 + m_2^3 k_1^2}{2 (m_2 k_1)^2} \end{aligned}$$

The term $\overline{\sigma}^2_{\ddot{x}_2,S6}$ for the architecture S6 is given as:

$$\overline{\sigma}^2_{\ddot{x}_2,S6} = \overline{\sigma}^2_{\ddot{x}_2,S2} + (a_5 m_e^{-1} + a_6 m_e^{-2} - 2 a_2 m_e^{-1} k_3^{-1}) r_2 \tag{7.24}$$

Analytical expression of road holding

The input parameters m_1, m_2, k_1, A_b, and v are fixed for all the architectures. The generic expression of road holding for all the architectures is,

$$\sigma_{F_z,Si} = \sqrt{A_b v \overline{\sigma}^2_{F_z,Si}} \tag{7.25}$$

where $\overline{\sigma}^2_{F_z,Si}$ is expressed for the architecture S1 as:

$$\overline{\sigma}^2_{F_z,S1} = b_1 r_2 + \frac{b_2}{r_2} \tag{7.26}$$

where

$$\begin{aligned} b_1 &= \frac{(m_1+m_2)^2 k_1}{2m_2^2} \\ b_2 &= \frac{(m_1+m_2)^3 k_2^2 - 2m_1 m_2 (m_1+m_2) k_1 k_2 + m_1 (m_2 k_1)^2}{2m_2^2} \end{aligned}$$

The term $\overline{\sigma}^2_{F_z,S2}$ for the architecture S2 is given as:

$$\overline{\sigma}^2_{F_z,S2} = \sigma^2_{F_z,S1} + (\frac{b_3}{k_3} + \frac{b_4}{k_3^2}) r_2 \tag{7.27}$$

where

$$\begin{aligned} b_3 &= \frac{2(m_1+m_2)^2 k_1 k_2 - m_2 (m_2+2m_1) k_1^2}{2m_2^2} \\ b_4 &= \frac{(m_1+m_2)^2 k_1 k_2^2 - m_2 (m_2+2m_1) k_1^2 k_2 + m_2^2 k_1^3}{2m_2^2} \end{aligned}$$

The term $\overline{\sigma}^2_{F_z,S3}$ for the architecture S3 is given as:

$$\overline{\sigma}^2_{F_z,S3} = b_1 r_2 + (b_2 - b_3 m_e + b_5 m_e^2) r_2^{-1} \tag{7.28}$$

where

$$b_5 = \frac{(m_1+m_2) k_1^2}{2m_2^2}$$

The term $\overline{\sigma}^2_{F_z,S4}$ for the architecture S4 is given as:

$$\overline{\sigma}^2_{F_z,S4} = (b_1 + b_6 m_e^{-1} + b_7 m_e^{-2}) r_2 + b_2 r_2^{-1} \tag{7.29}$$

where

$$\begin{aligned} b_5 &= \frac{-(m_1+m_2)^3 k_2 + m_1 m_2 (m_1+m_2) k_1}{m_2^2} \\ b_6 &= \frac{(m_1+m_2)^4 k_2^2 + (m_1+m_2)^2 (m_2-2m_1) m_2 k_1 k_2 + (m_1 m_2 k_1)^2}{2m_2^2 k_1} \end{aligned}$$

The term $\overline{\sigma}^2_{F_z,S5}$ for the architecture S5 is given as:

$$\overline{\sigma}^2_{F_z,S5} = \overline{\sigma}^2_{F_z,S1} + (b_5 m_e^{-1} + b_6 m_e^{-2}) r_2 + ((b_7 + b_8 m_e^{-1} + b_9 m_e^{-2}) k_3^2 - (b_5 + 2b_6 m_e^{-1}) k_3) r_2^{-1} \tag{7.30}$$

where

$$\begin{aligned} b_7 &= \frac{(m_1+m_2)^3}{2m_2^2} \\ b_8 &= \frac{-(m_1+m_2)^4 k_2 + m_2(m_1+m_2)^2(2m_1-m_2)k_1}{2m_2^2 k_1} \\ b_9 &= \frac{m_1+m_2}{2m_2^2 k_1^2}((m_1+m_2)^4 k_2 + 2m_2(m_1+m_2)^2(m_2-m_1)k_1 k_2 + (m_1^2 - m_1 m_2 + m_2^2)(m_2 k_1)^2) \end{aligned}$$

The term $\overline{\sigma}^2_{F_z,S6}$ for the architecture S6 is given as:

$$\overline{\sigma}^2_{F_z,S6} = \overline{\sigma}^2_{F_z,S2} + (b_5 m_e^{-1} + b_6 m_e^{-2} - 2b_2 m_e^{-1} k_3^{-1}) r_2 \tag{7.31}$$

Analytical expression of working space

The input parameters m_1, m_2, k_1, A_b, and v are fixed for all the architectures. The generic expression of working space for all the architectures is,

$$\sigma_{x_2-x_1,Si} = \sqrt{A_b v \overline{\sigma}^2_{x_2-x_1,Si}} \tag{7.32}$$

where $\overline{\sigma}^2_{x_2-x_1,S1}$ is expressed for S1 as:

$$\overline{\sigma}^2_{x_2-x_1,S1} = c_2 r_2^{-1} \tag{7.33}$$

where

$$c_2 = \frac{m_1+m_2}{2}$$

The term $\overline{\sigma}^2_{x_2-x_1,S2}$ for the architecture S2 is given as:

$$\overline{\sigma}^2_{x_2-x_1,S2} = \sigma^2_{x_2-x_1,S1} + c_4 k_3^{-2} r_2 \tag{7.34}$$

where

$$c_4 = \frac{k_1}{2}$$

The term $\overline{\sigma}^2_{x_2-x_1,S3}$ for the architecture S3 is given as:

$$\overline{\sigma}^2_{x_2-x_1,S3} = \overline{\sigma}^2_{x_2-x_1,S1} \tag{7.35}$$

The term $\overline{\sigma}^2_{x_2-x_1,S4}$ for the architecture S4 is given as:

$$\overline{\sigma}^2_{x_2-x_1,S4} = c_7 m_e^{-2} r_2 + c_2 r_2^{-2} \tag{7.36}$$

where

$$c_7 = \frac{(m_1+m_2)^2}{2k_1} + \frac{m_2^2}{2k_2}$$

The term $\overline{\sigma}^2_{x_2-x_1,S5}$ for the architecture S5 is given as:

$$\overline{\sigma}^2_{x_2-x_1,S5} = \frac{N1}{2D} + \frac{N2}{D} \tag{7.37}$$

where

$$\begin{aligned}
D =& r_2(-k_1k_2^2k_3^2D_1 + k_3(k_1^3k_2m_2^2m_e^4 + m_e^3D_2 + m_e^2D_3) + k_1^3k_2^2m_2^2m_e^4)\\
D_1 =& (m_1+m_2)^3m_e^3 + 3m_1m_2(m_1+m_2)^2m_e^2 + 3m_1^2m_2^2(m_1+m_2)m_e + m_1^3m_2^3\\
D_2 =& k_1^2k_2^2m_2^2(m_1+m_2) - k_1k_2^3(m_1+m_2)^3 + 2k_1^3k_2m_2^3\\
D_3 =& k_1^3k_2m_2^4 + k_1^2k_2^2m_2^3(m_1+3m_2) + k_1k_2^3m_2(-m_1^3+m_1^2m_2+5m_1m_2^2+3m_2^3)\\
&+ k_2^4(m_1+m_2)^4\\
N_1 =& k_1^3k_2^2m_2^2m_e^2N_{11} + k_1^3k_2m_2^2m_e^2N_{12} + k_1k_2^2k_3^2m_2^2m_e^2N_{13} + k_1^2k_2k_3m_2^2r_2^2N_{14}\\
&+ k_1^2k_2^2m_2^2m_e^2N_{15}\\
N_{11} =& m_2m_e^2 + m_2^2m_e + m_2^3 + m_1m_e^2\\
N_{12} =& k_3m_2m_e^2 - k_3m_2^2m_e + m_2^2r_2^2 + k_3m_1m_e^2 + k_3m_1m_2^2\\
N_{13} =& (m_1+m_2)^3\\
N_{14} =& m_1m_2^2 + m_2^2m_e^2 + m_1^2m_e^2\\
N_{15} =& -k_3m_2^2m_e + m_2^2r_2^2 - k_3m_1^2m_e + k_3m_1^2m_2 + m_1^2r_2^2 + k_3m_1m_2^2\\
N_2 =& k_1^3k_2k_3m_1m_2^2m_e^3 + k_1^2k_2k_3m_2^2m_eN_{21} + k_1^2k_2^2m_1m_2^3m_e^2N_{22}\\
N_{21} =& k_3m_2(m_2^2m_e - 2m_1^2m_e - m_1m_2m_e) - k_3m_1^2m_2^2 - k_3m_e^2(m_1+m_2)^2\\
&+ m_1m_2r_2^2(m_1+m_2+m_e)\\
N_{22} =& r_2^2 - k_3m_e
\end{aligned}$$

The term $\overline{\sigma}^2_{x_2-x_1,S6}$ for the architecture S6 is given as:

$$\overline{\sigma}^2_{x_2-x_1,S6} = \overline{\sigma}^2_{x_2-x_1,S2} + (c_7m_e^{-2} - 2c_2m_e^{-1}k_3^{-1})r_2 \tag{7.38}$$

7.2 Multi-objective optimisation

The optimisation problem of each suspension architecture is formulated as (2.1). Table 7.1 gives the parameters of the quarter-car model, road roughness coefficient (A_b), and the vehicle reference velocity used in the simulation. The bounds of the design variables such as suspension spring stiffness (k_2), damping coefficient (r_2), additional spring stiffness (k_3), and the equivalent mass of the inerter (m_e) are defined based on their feasible limits as given in Tab. 7.2.

As the numerically sorting, discussed in Section 2.1.2, requires high number functional evaluations, the preliminary solutions are obtained using the Sobol sequence. The Pareto-optimal set can be improved using the constraint method or analytical method.

Table 7.1: *Quarter-car model fixed parameters, vehicle velocity, and road roughness.*

Parameter	Unit	Value
m_1	kg	50
m_2	kg	250
k_1	N/m	120000
v	m/s	20
A_b	m	1.4e-5

Table 7.2: *Bounds of the suspension design variables*

Design variable	Unit	Lower bound	Upper bound
k_2	N/m	0	30000
k_3	N/m	0	300000
r_2	N s/m	0	4000
m_e	kg	0	300

7.3 Comparison of Pareto-optimal sets

Pareto-optimal sets of all the suspension architectures obtained using the constrained method are compared in the three objective functions domain in Fig. 7.4. The performance of architectures S2, S5 and S6 dominate the other architectures. The S2 and S6 have the same discomfort and road holding performances when the discomfort is below 0.7 $\mathrm{m/s^2}$, otherwise the architecture S6 is marginally better than S2 which does not have any practical significance. The discontinuity in the Pareto-front of S6 is due to numerical differences in the calculated values. For better clarity, the comparison is repeated by considering two objective functions each time and the solutions in design variables domain are also presented.

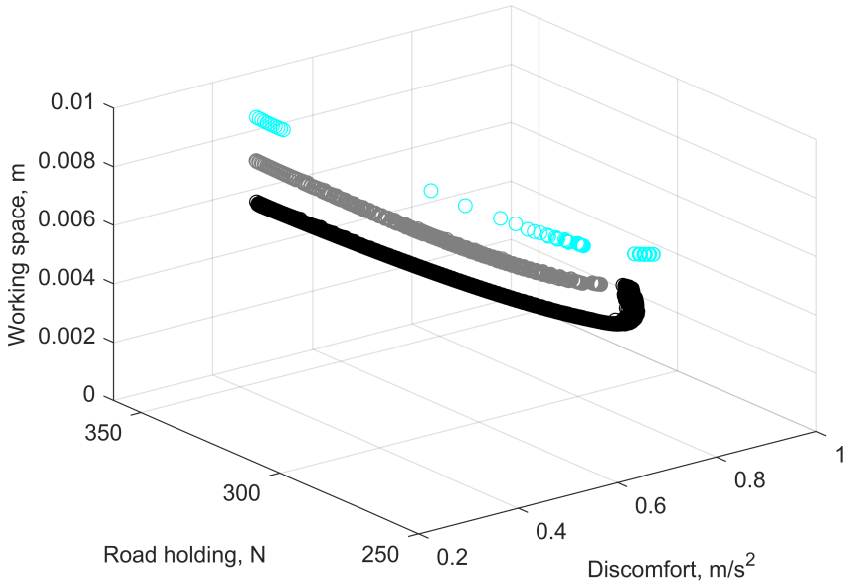

Fig. 7.4: *Pareto-optimal set of architectures S1-S6 in all three objective functions domain*

7.3.1 Comparison of Pareto-optimal sets in the two objective functions domain

The Pareto-optimal set of a two objective functions problem is on the border of the projection of the surface that represents the three objective functions' Pareto-optimal set [113]. The results of architectures S3, S4, and S5 are compared against S1, as they are equivalent when the inerter is neglected. Similarly, S6 is compared against S2. Comparison of S2 and S1 explains the benefit of the relaxation spring k_3.

Comparison of Pareto-optimal sets in discomfort-road holding domain

Pareto-optimal sets of all the architectures are compared in the discomfort-road holding domain in Fig. 7.5.The points marked on the Pareto frontiers hold minimum distance from their individual utopia points [4]. The values of the design variables and objective functions that correspond to these points are compared in Table 7.3.

It can be observed from Fig. 7.5 that the S5 is better than S1, S3, and S4 on both discomfort and road holding. The architectures with additional spring in series to damper (S2 and S6) are giving the best performance among the other considered architectures. The architecture S6 is marginally better than S2 when the discomfort is greater than 0.7 $\mathrm{m/s^2}$. The inerter in S3 does not give any improvement over S1.

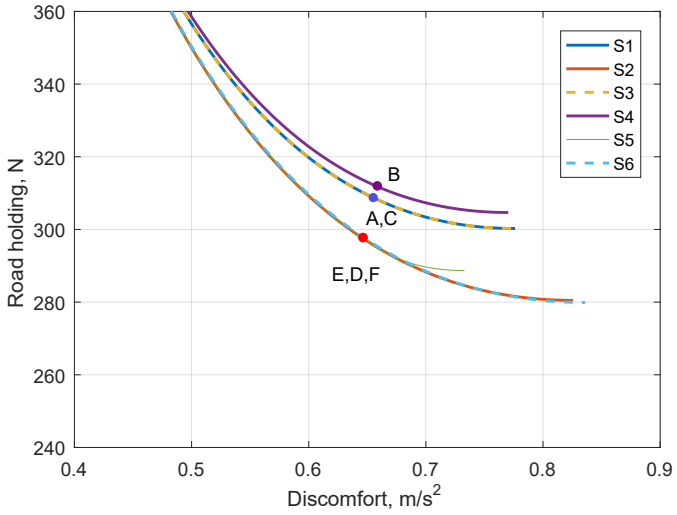

Fig. 7.5: *Pareto-optimal sets in the discomfort-road holding domain for architectures s1-s6 when all design variables are varied.*

Table 7.3: *Evaluation points marked in FIG. 7.5.*

Point	DC	RH	k_2	r_2	k_3	m_e
	$\mathrm{m/s^2}$	N	N/m	N s/m	N/m	kg
A (S1)	0.65	310	3498	880		
B (S2)	0.66	312	1780	921	207880	
C (S3)	0.65	310	3498	880		≈ 0
D (S4)	0.64	298	5237	886		≈ 300
E (S5)	0.64	298	12427	877	4164	88
F (S6)	0.64	298	3515	912	169525	≈ 300

Comparison of Pareto-optimal sets in discomfort-working space domain

Figure 7.6 compares the Pareto-optimal sets of the architectures in the discomfort-working space objective functions domain. The architectures S3, S4, S6 do not have any considerable benefits compared to their equivalent architectures without inerter. But the architecture S5 has better performance in both discomfort and working space domains for the reasonable values of design variables shown in Table. 7.4. The relaxation spring in architecture S2 does not give any significant improvement on discomfort and working space.

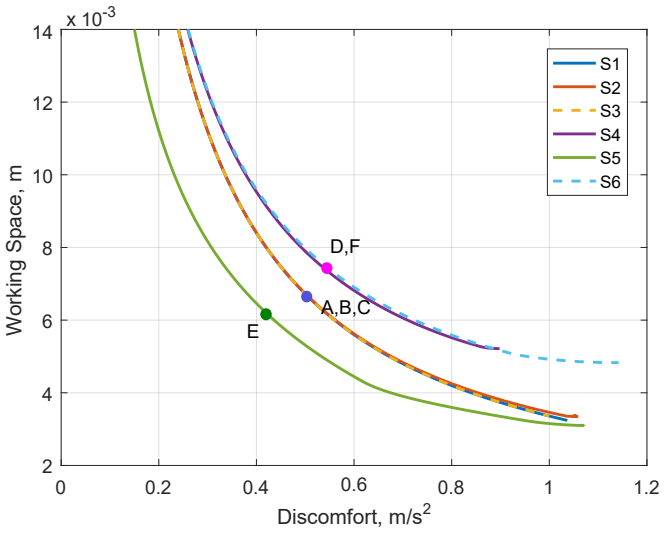

Fig. 7.6: *Pareto-optimal sets in the discomfort-working space domain for architectures s1-s6 when all design variables are varied.*

Table 7.4: *Evaluation points marked in FIG. 7.6.*

Point	DC	WS	k_2	r_2	k_3	m_e
	$\mathrm{m/s^2}$	mm	N/m	N s/m	N/m	kg
A (S1)	0.51	6.6	≈ 0	841		
B (S2)	0.51	6.6	≈ 0	525	≈ 300000	
C (S3)	0.51	6.6	≈ 0	524		≈ 0
D (S4)	0.55	7.4	3336	491		≈ 300
E (S5)	0.42	6.2	9516	380	2387	40
F (S6)	0.55	7.4	3239	487	≈ 300000	≈ 300

Comparison of Pareto-optimal sets in working space-road holding domain

Figure 7.7 compares the Pareto-optimal sets of the architectures in the working space-road holding domain. The architecture S2 and S6 have better performances when the aim is to seek the lowest road holding. Though the inerter in S6 gives a marginal improvement over S2 on road holding, it worsens working space significantly. The architecture S5 is a compromised solution in both objective functions.

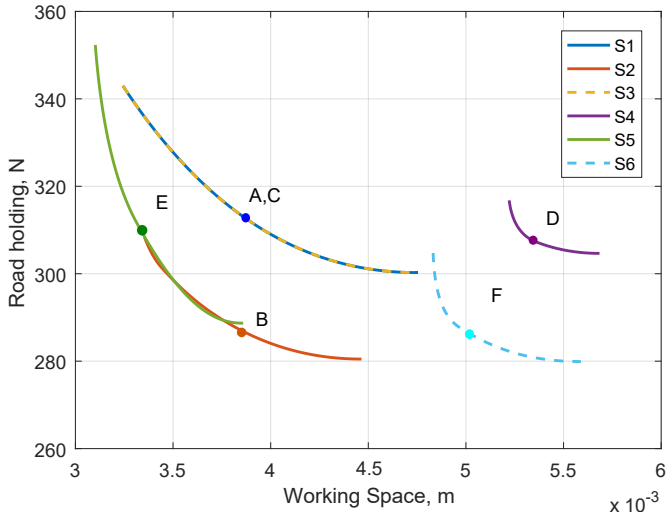

Fig. 7.7: *Pareto-optimal sets in the working space-road holding domain for architectures s1-s6 when all design variables are varied.*

Table 7.5: *Evaluation points marked in Fig. 7.7.*

Point	WS	RH	k_2	r_2	k_3	m_e
	mm	N	N/m	N s/m	N/m	kg
A (S1)	3.8	314	12602	2659		
B (S2)	3.8	287	0	3252	227400	
C (S3)	3.8	314	12602	2659		≈ 0
D (S4)	5.4	307	30635	2287		≈ 300
E (S5)	3.3	309	≈ 50000	2806	33048	194
F (S6)	5	287	32750	2773	197320	≈ 300

7.3.2 Comparison of Pareto-optimal sets in the design variables domain

The Pareto-optimal sets in the design variable domain corresponding to the results in objective function domain Section 7.3.1 are discussed here.

For the S1, the Pareto-optimal sets in the design variables domain are shown in Fig. 7.8. The intersection of DC-RH and DC-WS is the minimum of discomfort, where r_2 and k_2 are equal to zero. Similarly, the intersection of DC-RH and WS-RH is the minimum of road holding, where r_2 and k_2 are equal to 1863 Ns/m and 16680 N/m respectively. It is evident from (7.33) that the working space of S1 is not affected by k_2 and its minimum is achieved when r_2 reaches its upper bound.

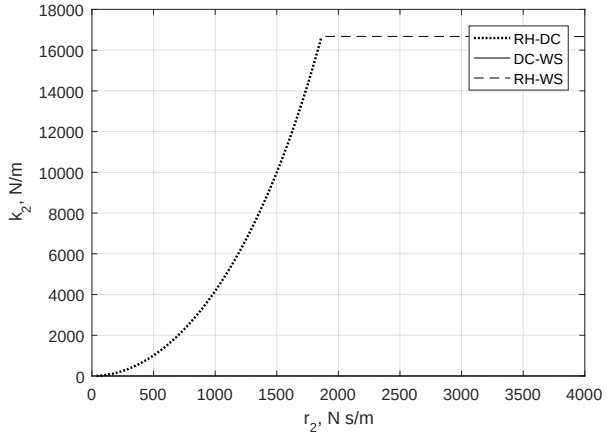

Fig. 7.8: *Pareto-optimal solutions of the architecture S1 in the design variables domain*

The Pareto-fronts of S2 are plotted in the design variables domain in Fig. 7.9 and Fig. 7.10. When k_2 and r_2 are zero, the minimum of discomfort does not depend on k_3. The minimum of road holding is achieved when $k_2 = 8700\,\mathrm{N/m}$, $r_2 = 2250\,\mathrm{Ns/m}$, and $k_3 = 182000\,\mathrm{N/m}$. But the minimum working space is limited by the bounds of the design variables ($k_2 = 0\,\mathrm{N/m}$, $r_2 = 4000\,\mathrm{Ns/m}$, and $k_3 = 300000\,\mathrm{N/m}$)

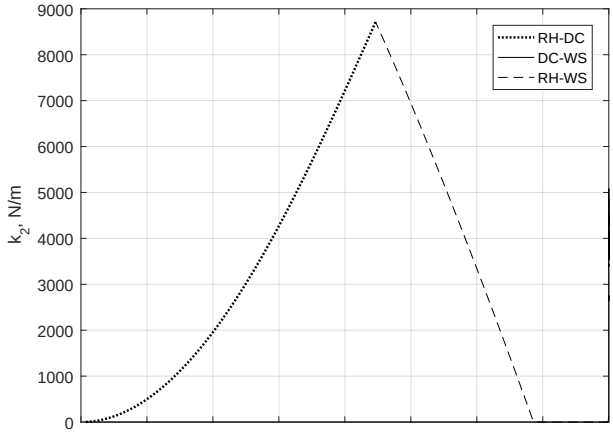

Fig. 7.9: *Pareto-optimal solutions of the architecture S2 in the design variables domain*

As shown in Figs.7.5,7.6, and 7.7, the architecture S3 is completely dominated by S1. Hence, the Pareto-optimal sets in the design variables domain are exactly same as that of S1 in Fig. 7.8 and the value of inerter equivalent mass $m_e = 0$. On the other hand, the inerter mass is always on the upper bound for all the Pareto-optimal sets of S4. So, the results are plotted between r_2 and k_2 in Fig. 7.11. The minimum of discomfort is achieved when both r_2 and k_2 are zero. As shown in the plot, the intersection of Pareto-fronts RH-DC and RH-WS gives the values of design variables $r_2 = 1873\mathrm{Ns/m}$

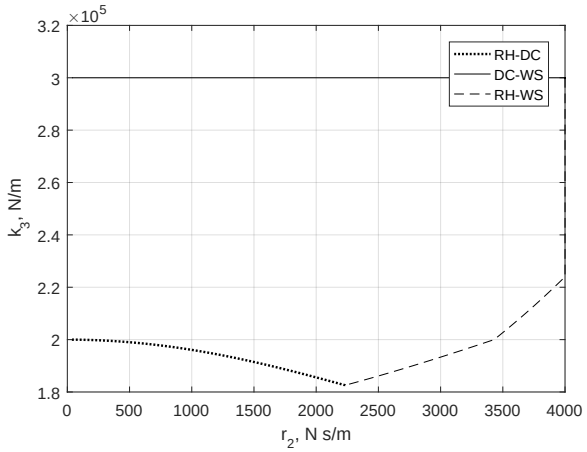

Fig. 7.10: *Pareto-optimal solutions of the architecture S2 in the design variables domain*

and $k_2 = 23590\mathrm{N/m}$ corresponding to the minimum of road holding. The minimum of working space is limited by the upper bounds of the design variables.

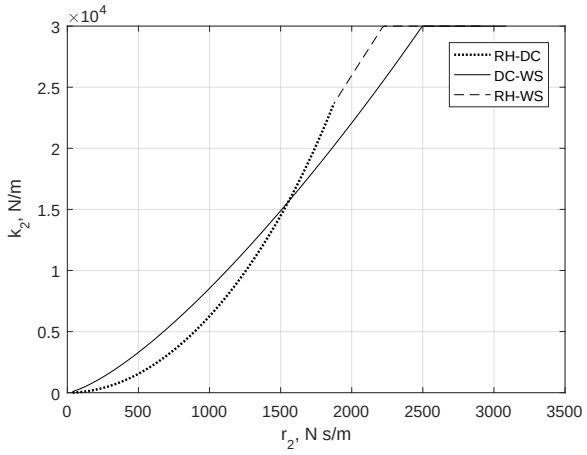

Fig. 7.11: *Pareto-optimal solutions of the architecture S4 in the design variables domain*

The architecture S5 performs better than the other considered architectures. The Pareto-optimal sets in the design variables domains are plotted by considering two variable at a time. Similar to the architecture S4, the Pareto-solutions of inerter equivalent mass in the architecture S6 is always on the upper bound. Therefore, the results are plotted between k_2, k_3, and r_2 in Figs. 7.15 and 7.16

The study shows that the architecture S5 gives improvements in all the objective functions compared to the others. Hence, in order to achieve the maximum benefit on the ride performance for in-wheel motor electric vehicles, the architecture S5 is considered for the optimisation.

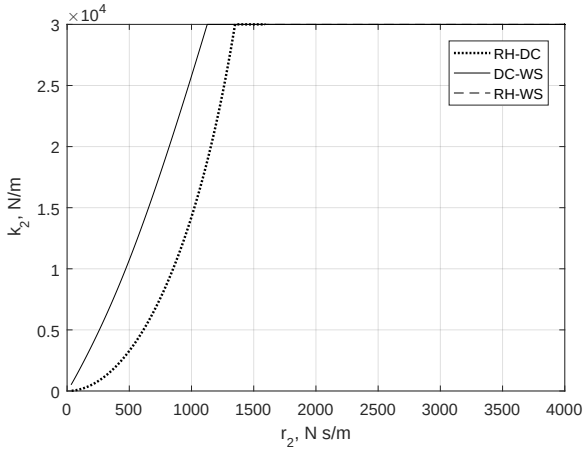

Fig. 7.12: *Pareto-optimal solutions of the architecture S5 in the design variables domain*

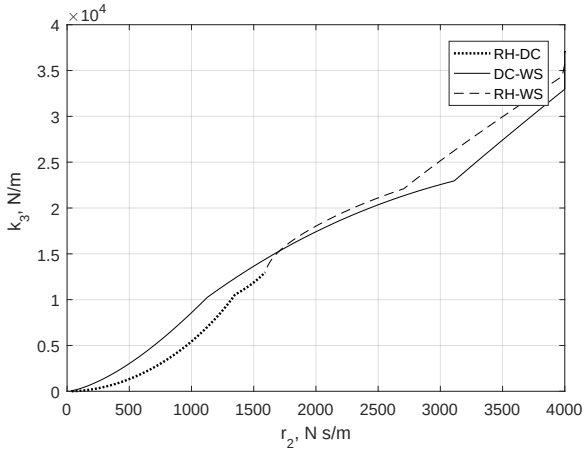

Fig. 7.13: *Pareto-optimal solutions of the architecture S5 in the design variables domain*

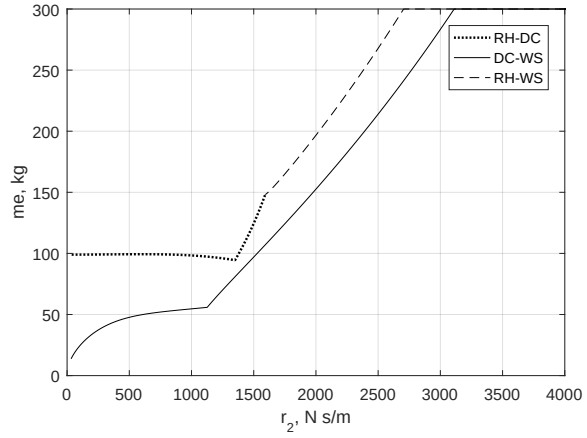

Fig. 7.14: *Pareto-optimal solutions of the architecture S5 in the design variables domain*

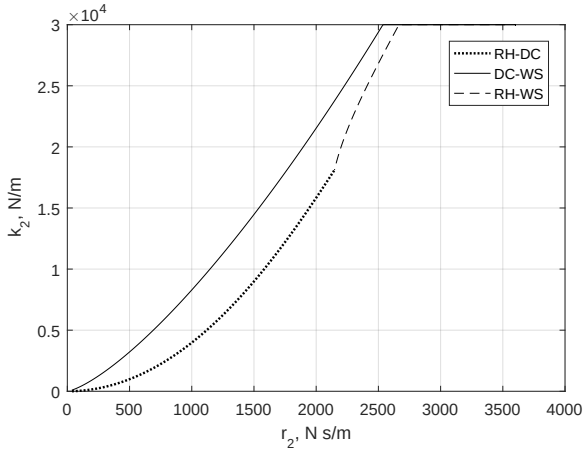

Fig. 7.15: *Pareto-optimal solutions of the architecture S6 in the design variables domain*

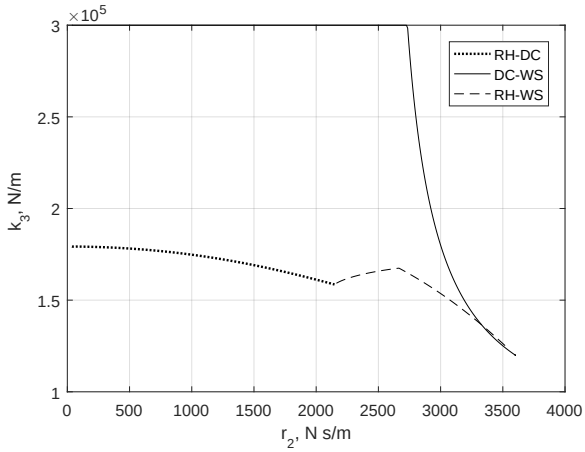

Fig. 7.16: *Pareto-optimal solutions of the architecture S6 in the design variables domain*

CHAPTER 8

In-wheel motor electric vehicle optimisation

A method for the optimal design of electric vehicles with in-wheel motors is developed by effectively combining the Multi-objective optimisation (MOO) techniques with Analytical target cascading (ATC) approach. The complex problem is partitioned into manageable subsystems and the objective functions that belong to each subsystem are treated together. The interactions between subsystems are achieved using the feedback based coordination strategy (ATC). This iterative algorithm ensures convergence that meets the system level targets while complying with the subsystem level constraints and requirements. In the proposed ATC based hierarchical optimisation method, the analytical motor model (in Chapter 4) which uses complex relative permeance model (in Chapter 3) is adopted to estimate the in-wheel motor performance. The suspension architecture S5 that was observed to give better results compared to the other architectures in Chapter 7 is used to mitigate the negative impacts of increased unsprung mass. The thermal and NVH models discussed in Chapter 5 and 6, respectively, evaluate the motor candidates on thermal and acoustic behaviours. In addition, the battery and power electronics models are included to represent the power supply of the motor.

The electric vehicle optimisation problem is partitioned into two levels where the top level consists of vehicle model along with the electric motor and the power electronics models. The bottom level contains battery and suspension models. Pareto-optimal solutions are calculated for each subsystem considering the influences of the other subsystems. The generic layout of the methodology is discussed in the Section 2.3.1.

8.1 Optimisation problem formulation

A schematic layout of the in-wheel motor electric vehicle is shown in Fig.8.1. The vehicle has two outer rotor electric motors mounted in the wheels of rear axle and a Li-ion battery back. The suspension architecture S5 is considered here. Table 8.1 gives the compilation of all the objective functions, design variables, and constraints of the optimisation problem.

Table 8.1: *Optimisation problem of the complete vehicle*

Objective functions	Energy consumption (kWh)	E_c	(8.1)
	Gradeability	GL	(8.15)
	Discomfort ($\mathrm{m/s^2}$)	$\sigma_{\ddot{x}_2}$	(7.20)
	Road holding (N)	σ_{F_z}	(7.25)
	Working space (m)	$\sigma_{x_2-x_1}$	(7.32)
Design variables	Axial scaling ratio	k_a	
	Radial scaling ratio	k_r	
	Rated voltage (V)	V_r	
	Maximum current of motor (A)	I_{max}	
	Number of motors	N_{EM}	
	Number battery cells in series	N_{sc}	
	Number battery cells in parallel	N_{pc}	
	Spring stiffness ($\mathrm{N/m}$)	k_2	
	Damping ratio ($\mathrm{Ns/m}$)	r_2	
	Relaxation spring stiffness ($\mathrm{N/m}$)	k_3	
	Inerter equivalent mass (kg)	m_e	
Constraints	Energy consumption (kWh)≤Battery capacity (kWh)	$E_c \leq E_{batt}$	
	Motor input power (kW)≤Battery output power (kW)	$P_{in} \leq \frac{P_{batt}}{N_{EM}}$	
	Minimum required discomfort ($\mathrm{m/s^2}$)	$\sigma_{\ddot{x}_2} \leq L_1$	
	Minimum required working space (m)	$\sigma_{x_2-x_1} \leq L_2$	
	Minimum required road holding (N)	$\sigma_{F_z} \leq L_3$	

The design optimization having five objective functions is difficult to be solve using AiO method, so it can be partitioned into subsystems and solved as per the proposed method based on ATC coordination strategy. The design targets of the complete vehicle are either handled at the system level and cascaded down or passed directly to the lower levels. For example, in the two-level proposed ATC model, the targets on vehicle

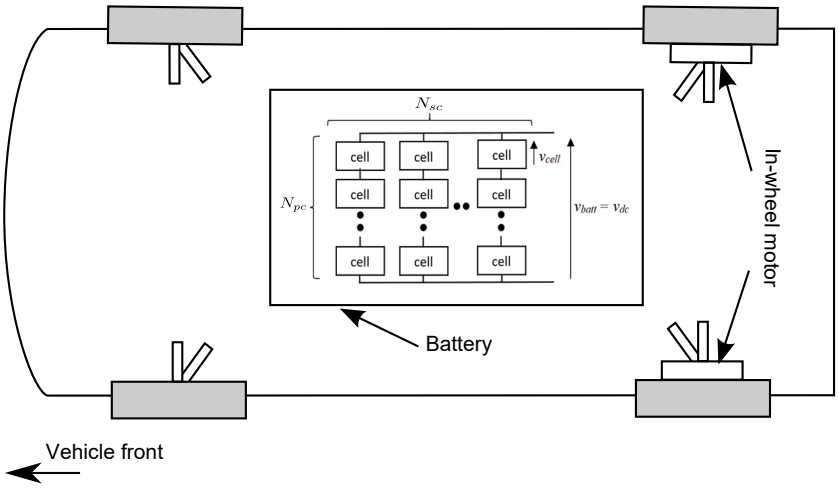

Fig. 8.1: *In-wheel motor electric vehicle layout*

performance are handled at the top level, whereas the ride performance targets (L_{1-3}) are given to the suspension model at the bottom level as constraints. The objective functions are derived in the following sections.

8.1.1 System model: In-wheel motor electric vehicle

At the system level, the objective functions are the energy consumption of the vehicle in a given range target as per NEDC (E_c) and driving performance. Gradeability limit (GL), which is directly related to acceleration and fun-to-drive, is considered to quantify the driving performance. The design variables are axial and radial scaling ratios (k_a and k_r) of the electric motor as in Fig. 4.5, the rated voltage (V_r), and the total number of battery cells (N_{bc}). The optimum value of N_{bc} is cascaded to the battery model as a target. Similarly, the m_1 and m_2 are given to the suspension model. The motor input power requirement P_{in} is treated as a shared variable. The constraints are defined on the acoustic performance of the machine, energy content of the battery and the maximum allowable motor power (P_{in}). As discussed in Chapter 6, the acoustic performance is a subjective measure. The simplified model, which considers only the vibrations due to electromagnetic forces, gives an indication that a set of design candidates can be preferred over the others. Hence, a constraint on the acoustic performance of the motor is defined in such a way that the worst performing 20% of the total design candidates are eliminated. Before defining the limiting value of the acoustic sound pressure level (SPL), the variation of SPL is studied in the complete range of motor design candidates as in Fig. 6.4.

The objective functions, design variables, and constraints of the top-level system model are listed in Table 8.2. The considered vehicle parameters and requirements are given

in Table 8.3.

Table 8.2: *Optimisation problem of the system model*

Objective functions	E_c , GL
Design variables	k_a , k_r , N_{bc} , V_r
Linking variables	N_{bc} , m_2 , m_1
Shared variable	P_{in}
Constraints	$E_c \leq E_{batt}$; $N_{EM}P_{in} \leq P_{batt}$; $SPL \leq L_4$

Table 8.3: *Vehicle parameters and requirements used in the optimisation*

Total vehicle mass $\mathrm{m_v}$, kg	Depends on motor and battery sizes
Vehicle body mass $\mathrm{m_{body}}$, kg	800
Motor mass $\mathrm{m_{motor}}$, kg	Depends on $\mathrm{k_a}$, $\mathrm{k_r}$
Battery mass $\mathrm{m_{batt}}$, kg	Depends on $\mathrm{N_{bc}}$
Battery cell mass $\mathrm{m_{cell}}$, kg	0.787
Frontal Area A, $\mathrm{m^2}$	2
Co-efficient of drag $\mathrm{C_d}$	0.25
Number of motors N_{EM}	2
Rolling resistance coefficient $\mathrm{C_r}$	0.01
Wheel radius $\mathrm{R_w}$, m	0.32
Required range, km	250
L_1, m/s^2	0.8
L_2, m	20e-3
L_3, N	400
L_4, dB	20

Energy consumption (E_c) calculation

The total energy consumption of the vehicle E_c is the summation of energy consumption in the electric motors (E_{EM}) and the power electronics (E_{PE}) within the targeted range (R_t).

$$E_c = \frac{R_t}{D_{DC}} \frac{N_{EM}(E_{EM} + E_{PE})}{3600 \,\mathrm{x}\, 1000} \tag{8.1}$$

where D_{DC} is the distance travelled in a single driving cycle. The electric motor input power, which is the sum of tractive power (P_{DC}) and motor losses such as copper

losses (P_a), core losses (P_c), magnet losses (P_{PM}), and mechanical losses (P_{mech}), is integrated over the driving cycle to get E_{EM}.

$$E_{EM} = \int_0^{t_{DC}} (P_{DC} + P_c + P_{mech} + P_{PM} + P_a)dt \tag{8.2}$$

where P_{DC} is defined as tractive torque at the wheel (T_{DC}) times the angular speed (Ω). The tractive torque in a driving cycle is calculated by multiplying the sum of aerodynamic resistance, gradient force, rolling resistance and inertial force with the wheel radius (R_w) as in (5.8) [122]. Based on the analytical motor model described in Section. 4.4, the in-wheel motor losses are calculated at every operating point.

For the Power electronics model, the most widely used space vector pulse width modulation (SVPWM) scheme is adopted due its effective dc bus utilization and reduced harmonics [123]. The circuit model of a typical three-phase voltage source inverter (VSI) is shown in Fig. 8.2. The three legs (A,B,and C) have six power switches (S_1 to S_6) which are composed of insulated-gate bipolar transistors (IGBT) and diodes.

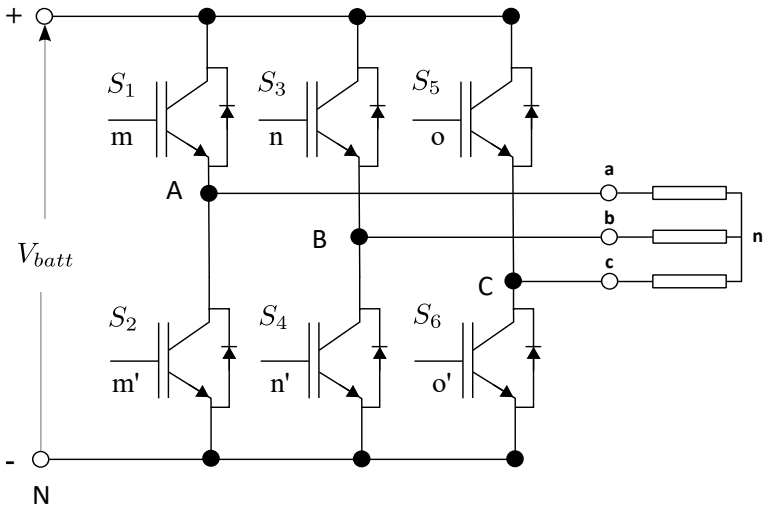

Fig. 8.2: *Circuit model of a typical three-phase voltage source inverter.*

The relationship between the switching variable vector $[m, n, o]^t$ and the phase voltage vector $[\vec{V}_{an}\vec{V}_{bn}\vec{V}_{cn}]^t$ is given in (8.3) [124].

$$\begin{bmatrix} \vec{V}_{an} \\ \vec{V}_{bn} \\ \vec{V}_{cn} \end{bmatrix} = \frac{V_{batt}}{3} \begin{bmatrix} 2 & -1 & -1 \\ -1 & 2 & -1 \\ -1 & -1 & 2 \end{bmatrix} \begin{bmatrix} m \\ n \\ o \end{bmatrix} \tag{8.3}$$

The switching variable vector has binary digits, e.g. 101, which indicate the switch state of inverter legs. The digits 1 and 0 imply the ON state of the upper and lower switches, respectively. The two switches of the same leg are not switched ON or OFF

simultaneously to avoid short-circuiting. The most significant bit of the switching variable vector represent the leg A, the least significant bit is related to leg C and the middle is for leg B.

There are eight possible combinations ($\vec{V}_{1-8}$) of switching patterns for the three upper switches. The phase vector voltage corresponding to each switching pattern is defined in Table. 8.4.

Table 8.4: *Phase voltages for different switching states.*

State	Switching vector	Switches ON	$\vec{V}_{an}$	$\vec{V}_{bn}$	$\vec{V}_{cn}$
1	100	1,4,6	$(2/3)V_{batt}$	$-(1/3)V_{batt}$	$-(1/3)V_{batt}$
2	110	1,3,6	$(1/3)V_{batt}$	$(1/3)V_{batt}$	$-(2/3)V_{batt}$
3	010	2,3,6	$-(1/3)V_{batt}$	$(2/3)V_{batt}$	$-(1/3)V_{batt}$
4	011	2,3,5	$-(2/3)V_{batt}$	$(1/3)V_{batt}$	$(1/3)V_{batt}$
5	001	2,4,5	$-(1/3)V_{batt}$	$-(1/3)V_{batt}$	$(2/3)V_{batt}$
6	101	1,4,5	$(1/3)V_{batt}$	$-(2/3)V_{batt}$	$(1/3)V_{batt}$
7	111	1,3.5	0	0	0
8	000	2,4,6	0	0	0

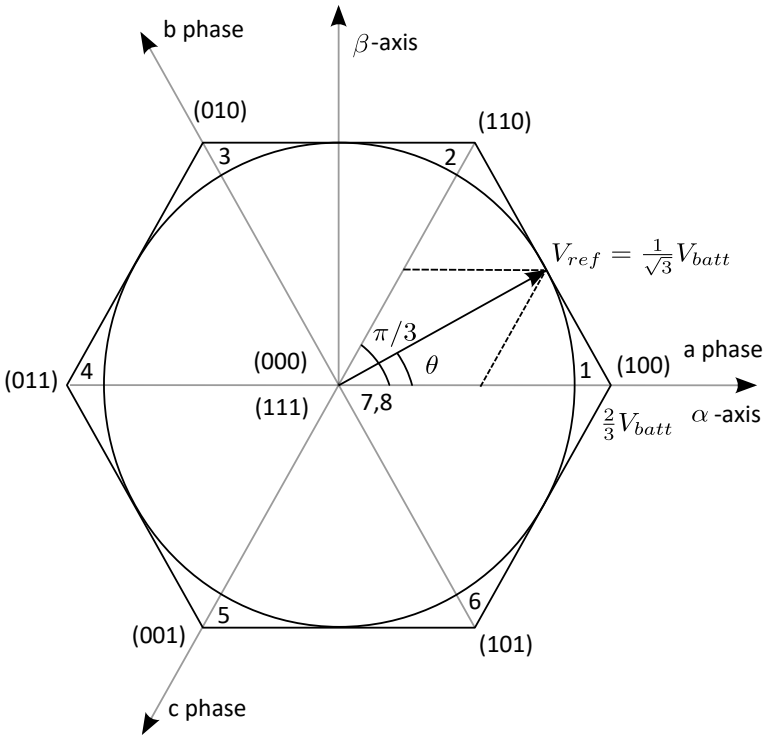

Fig. 8.3: *Switching vectors and space vector trajectory*

It is possible to transform the three-phase voltage vectors to equivalent two-phase vector, because one of the phase voltages is redundant from mathematical point of view [125]. The components of space vector in $\alpha - \beta$ plane are written as a complex number.

$$\vec{V}_\alpha + j\vec{V}_\beta = V_{batt}\frac{2}{3}\left(\vec{V}_a + \bar{a}\vec{V}_b + \bar{a^2}\vec{V}_c\right) \tag{8.4}$$

where $\bar{a} = \exp(j2\pi/3)$, $\bar{a}^2 = \exp(j4\pi/3)$. The coefficient 2/3 is chosen to ensure the magnitude of the two-phase voltages will be equal to that of the three-phase voltages after the transformation. The space vectors are represented in vector form in (8.5) and their corresponding switching states are given in Table. 8.5.

$$\begin{bmatrix}\vec{V}_\alpha \\ \vec{V}_\beta\end{bmatrix} = \frac{2}{3}\begin{bmatrix} 1 & \frac{-1}{2} & \frac{-1}{2} \\ 0 & \frac{\sqrt{3}}{2} & \frac{\sqrt{3}}{2}\end{bmatrix}\begin{bmatrix}\vec{V}_{an} \\ \vec{V}_{bn} \\ \vec{V}_{cn}\end{bmatrix} \tag{8.5}$$

Table 8.5: *Phase voltage space vector*

State	Phase voltage space vectors	V_α	V_β
1	$(2/3)V_{batt}$	$(2/3)V_{batt}$	0
2	$(2/3)V_{batt}\exp(j\pi/3)$	$(1/3)V_{batt}$	$(1/3)V_{batt}$
3	$(2/3)V_{batt}\exp(j2\pi/3)$	$-(1/3)V_{batt}$	$(1/3)V_{batt}$
4	$(2/3)V_{batt}\exp(j\pi)$	$-(2/3)V_{batt}$	0
5	$(2/3)V_{batt}\exp(j4\pi/3)$	$-(1/3)V_{batt}$	$-(1/3)V_{batt}$
6	$(2/3)V_{batt}\exp(j5\pi/3)$	$(1/3)V_{batt}$	$-(1/3)V_{batt}$
7	0	0	0
8	0	0	0

The reference vector, V_{ref} in Fig.8.3, rotates in the $\alpha - \beta$ plane and occupies one of six sectors as the different sets of switches are turned on or off. The magnitude of reference voltage vector is calculated from $\vec{V}_\alpha$ and $\vec{V}_\beta$.

$$V_{ref} = \sqrt{\vec{V}_\alpha^2 + \vec{V}_\beta^2} \tag{8.6}$$

The angular displacement between $\vec{V}_{ref}$ and the α-axis is obtained by integrating the electrical frequency $\omega(t)$.

$$\theta(t) = \int_0^t \omega(t)dt + \theta_0 \tag{8.7}$$

The maximum of reference voltage that corresponds to the radius of the largest possible circle that can be inscribed within the hexagon, shown in Fig. 8.3, is defined in (8.8).

$$V_{ref,max} = \frac{2}{3} V_{batt} \cos(\pi/6) = \frac{1}{\sqrt{3}} V_{batt} \tag{8.8}$$

Similarly, the maximum fundamental line-to-line rms voltage is calculated as,

$$V_{LL,max} = \frac{\sqrt{3} V_{ref,max}}{\sqrt{2}} = \frac{V_{batt}}{\sqrt{2}} = 0.707 V_{batt}. \tag{8.9}$$

Modulation index is the ratio of the fundamental component amplitude of the line-to-line inverter output voltage (V_{LL}) to the available dc bus voltage (V_{batt}). Thus,

$$M = \frac{V_{LL}}{V_{batt}} = \frac{\sqrt{3} V_{ref}}{V_{batt}} \tag{8.10}$$

Thus, the maximum modulation index in the case of SVPWM is derived as 1.

$$M_{max} = \frac{\sqrt{3} V_{ref,max}}{V_{batt}} = \frac{\sqrt{3}(V_{batt}/\sqrt{3})}{V_{batt}} = 1 \tag{8.11}$$

In order to estimate the losses in the inverter, the conduction losses, switching losses and off-state blocking losses are considered as in [126]. The analytical expression of the switching loss P_{ls} in IGBT devices is given by

$$P_{ls} = \frac{6}{\pi} f_s (E_{on,I} + E_{off,I} + E_{off,D}) \frac{V_{batt}}{V_r} \frac{I_L}{I_r}. \tag{8.12}$$

where f_s is the switching frequency, V_{batt} is the dc link voltage, I_L is the peak value of the sinusoidal line current, $E_{on,I}$ and $E_{off,I}$ are the turn-on and turn-off energies of the IGBT, respectively, $E_{off,D}$ is the turn-off energy of the power diode due to reverse recovery current. The properties of IGBT and diode are defined in Table. 8.6.
The conduction losses depend directly on the load current (I_L) modulation index (M) and the displacement angle (ϕ) between the fundamental of modulation function and the load current [126]. The conduction losses in the IGBT and the diode are expressed as

$$P_{lc,I} = \frac{V_{CE,0}}{2\pi} I_L \left(1 + \frac{M\pi}{4} \cos\phi\right) + \frac{r_{CE,0}}{2\pi} I_L^2 \left(\frac{\pi}{4} + \frac{2M}{3} \cos\phi\right) \tag{8.13}$$

$$P_{lc,D} = \frac{V_{F,0}}{2\pi} I_L \left(1 - \frac{M\pi}{4} \cos\phi\right) + \frac{r_{F,0}}{2\pi} I_L^2 \left(\frac{\pi}{4} - \frac{2M}{3} \cos\phi\right). \tag{8.14}$$

The total inverter losses are summed over the driving to calculate the energy consumption in power electronics (E_{PE}).
In the optimisation routine, when the reference motor geometry is scaled down, the current rating of the machine should be increased accordingly to achieve the required

Table 8.6: *Parameters of semiconductor devices*

State	Parameters	Values
IGBT	I_{ref}, A	400
	V_{ref}, V	300
	$E_{on,mJ}, A$	13
	$E_{off,mJ}, A$	7
	$V_{CE,0}, V$	1.6
Diode	$r_{CE,0}, m\Omega$	3.8
	$r_{F,0}, m\Omega$	3.9
	$V_{F,0}, V$	1.55
	$E_{off,D}, mJ$	7

output torque. The armature losses, magnet losses, and inverter losses increase with the current rating of the machine. On the other hand, the core losses decrease when the machine size is reduced. Since the NEDC is less demanding, the share of core loses is significant in the total losses. Hence, a careful evaluation of motor parameters should be made in the optimisation to achieve minimum overall energy consumption of the vehicle.

Gradeability limit estimation

The gradability (GR) limit is defined as the grade (θ) at which the vehicle can start and climb for 20 s [127]. On a flat road, it can represent the available tractive force at the given speed (v) for further acceleration. As the GR is more demanding due to higher duration (up to 20 sec) of the peak torque T_{peak} and thus the current requirement, it is preferred to quantify the driving performance of the vehicle over acceleration.

$$\begin{aligned} GR = \sin(\theta) &= \frac{d - C_r^2\sqrt{1 - d^2 + C_r^2}}{1 + C_r^2} \\ d &= \left(\frac{T_{peak}\omega_B}{v} - \frac{1}{2}C_d\rho_0 A v^2\right)\frac{1}{m_v g} \end{aligned} \tag{8.15}$$

This objective function is converted into a constraint as per the constraint MOO method in Section 2.1.2. The gradability limit requirement is translated to an inequality constraint $\Delta T_w \leq 60$ where ΔT_w is the winding temperature. This constraint enables the optimisation algorithm to consider only the motor candidates that can climb the targeted grade for 20s without violating the constraint on the winding temperature. A

thermal model based on lumped parameter thermal networks using the distributed loss and capacitance (DLC) element described in Section 5.5 is used here to estimate the winding temperature [52].

8.1.2 Subsystem model: Battery

In the battery model, the cells are arranged in a balanced scheme as shown Fig.8.4 to enable uniform utilization of the cells. The number of cells in series (N_{sc}) and parallel (N_{pc}) are taken as the design variables, and they are optimised for the consistency constraints on the linking variable battery size (N_{bc}). The battery output power (P_{in}) is considered as the shared variables. The bounds of N_{sc} and N_{pc} are defined in such a way that the maximum voltage and current ratings of the battery are restricted.

Table 8.7: *Optimisation problem of the battery model*

Design variables	N_{sc} , N_{pc}
Linking variables	N_{bc}
Shared variable	P_{batt}
Constraints	$N_{EM}P_{in} \leq P_{batt}$, $E_c \leq E_{batt}$

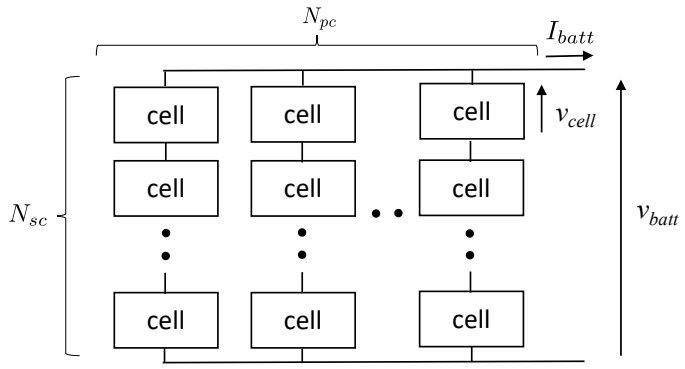

Fig. 8.4: *Arrangement of battery cells*

The battery size estimated by the battery model in (8.16) should be greater than or equal to the value of target linking variable from the system model.

$$N_{bc} = N_{sc}N_{pc} \tag{8.16}$$

The expressions of battery voltage, current, power, and available energy are given in (8.17). The maximum discharge pulse current rate of the Li-ion cell is taken as 3C, where C is the capacity of the cell in Ah. The available energy in the battery E_{batt} is

estimated considering 70% C as the useful capacity in each cell.

$$
\begin{aligned}
V_{batt} &= N_{sc}\, V_{cell} \\
I_{batt} &= N_{pc}\, 3C \qquad (8.17) \\
P_{batt} &= V_{batt} I_{batt} \qquad (8.18) \\
E_{batt} &= 0.7 N_{sc} N_{pc} C
\end{aligned}
$$

8.1.3 Subsystem model: Suspension

The comparison study in Chapter 7 shows that the architecture S5 performs better than the remaining considered architectures. The simplified quarter-car model, shown in Fig. 8.5, is used to describe the vertical dynamics of the in-wheel motor electric vehicle.

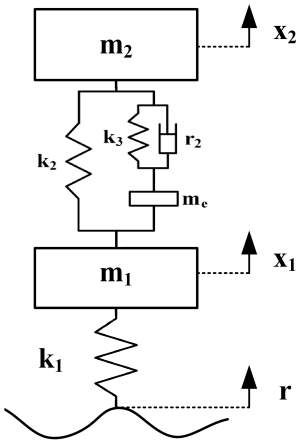

Fig. 8.5: *Quarter car suspension model*

In the suspension model, the objective functions are discomfort ($\sigma_{\ddot{x_2}}$), road holding (σ_{Fz}), and working space ($\sigma_{x_2-x_1}$) and their analytical expressions are given in (7.20), (7.25), and (7.32) respectively. The spring stiffness (k_2), additional spring stiffness (k_3), damping ratio (r_2), and inerter equivalent mass (m_e) are considered as the design variables and the remaining variables are fixed as in Table 8.9. The bounds of design variables are given in Table 8.20. The constraints are user defined minimum requirements for the objective functions. The sprung and unsprung masses (m_2 and m_1) of the quarter-car model are taken from the vehicle model as the target linking variables.
The weighted sum method discussed in Section 2.1.2 is used for solving the suspension optimisation problem. The convexity of each objective function is ensured by checking if the Hessian is positive semi-definite [128]. The weights (λ_i) in (8.19) are varied based on the desired characteristics of the vehicle, for example a sport car can have more weightage for road holding than discomfort.

Table 8.8: *Optimisation problem of the suspension model*

Objective functions	$\sigma_{\ddot{x_2}}$, $\sigma_{x_2-x_1}$, σ_{F_z}
Design variables	k_2 , k_3 , r_2 , m_e
Linking variables	m_1 , m_2
Constraints	$\sigma_{\ddot{x_2}} \leq L_1$; $\sigma_{x_2-x_1} \leq L_2$; $\sigma_{F_z} \leq L_3$

Table 8.9: *Data of quarter-car model, velocity, and road roughness*

Parameter	Unit	Value
k_1	N/m	120000
v	m/s	20
A_b	m	1.4e-5

$$\min_{x} \quad \lambda_1 \, \bar{\sigma}_{\ddot{x_2}} + \lambda_2 \, \bar{\sigma}_{Fz} + \lambda_3 \, \bar{\sigma}_{x_2-x_1} \tag{8.19}$$

where

$$0 \leq \lambda_i \leq 1 \, ; \quad \sum_{i=1}^{n_{of}} \lambda_i = 1$$

8.2 Subsystem optimisation

In the vehicle model, the N_{bc} is an integer valued design variable, and the calculations of E_c and ΔT_w are computationally expensive. Hence, an optimisation algorithm that can handle integer design variables and requires a minimum number of functional evaluations for the convergence is suitable. Genetic algorithm and a modified simplex algorithm (MSA) are considered as potential candidates. In the MSA, similar to the conventional simplex method, (n+1) points are selected in the simplex of an n design variable problem as shown in Fig.8.6 and ranked based on the values of the objective function calculated at each point. After performing reflection, expansion, and contraction operations on the design candidates, the position of the new point (R) is updated to the closest integer value (R') of the required design variable. Figure 8.7 compares the convergence performance of the MSA and GA in terms of the final value and the required number of functional evaluations. Though the GA works reasonably well for this problem, it is observed to be slower than the MSA. Hence, the MSA is chosen as the appropriate method to solve the system level optimisation problem.

The MATLAB implementation of $fminsearch$ employs the conventional simplex method,

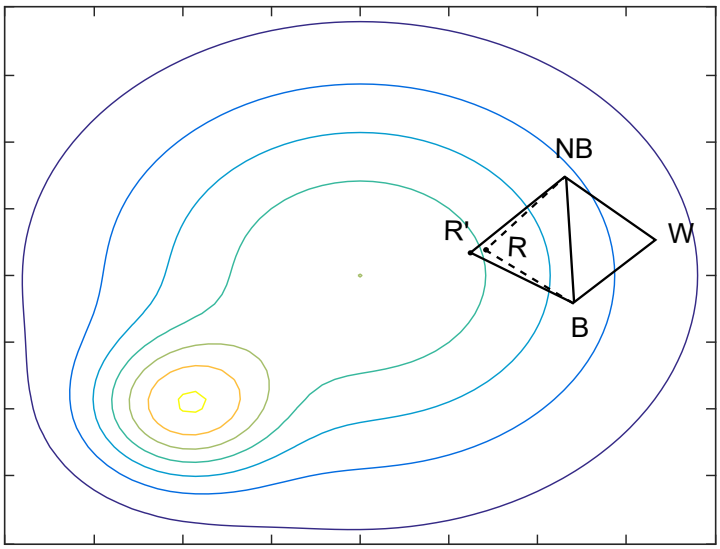

Fig. 8.6: *Modified simplex algorithm.*

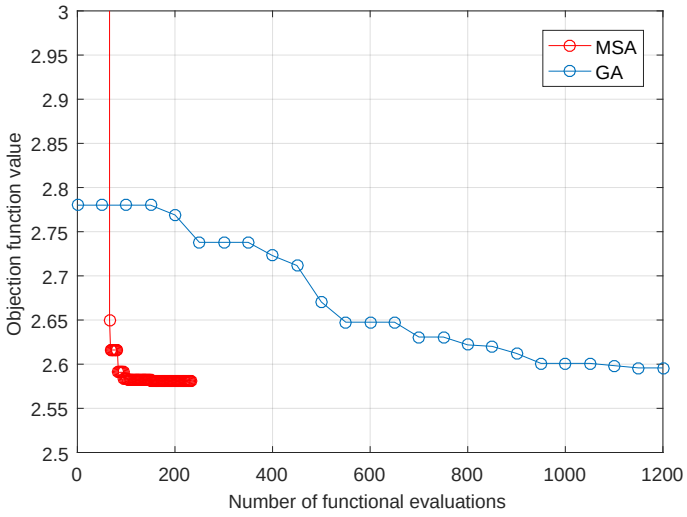

Fig. 8.7: *Comparison of convergence performance of modified simplex algorithm (MSA) and genetic algorithm (GA).*

which is an unbounded and unconstrained optimization algorithm. In order to include the bounds, the design variables are updated as per the expression given in (8.20) [129] in each iteration of $fminsearch$. Then the required design variables are updated to the closest integer value using $round$ function in MATLAB.

$$x = LB + (UB - LB) * (sin(z) + 1)/2 \tag{8.20}$$

$$x(*) = round(x(*)) \tag{8.21}$$

where LB and UB correspond to the lower bounds and upper bounds of the design vari-

ables, z is the fully unconstrained design variables vector, and x is the design variables vector within the bounds. The symbol * denotes the position of the integer-valued design variable. The inequality constraints (g) are converted into penalty functions (exterior) as in (8.22) and added to the objective function (E_c). Thus, the problem is transformed into an unconstrained optimization problem, which can be solved using $fminsearch$.

$$PF = \frac{1}{2}\sum_{i=1}^{m}(\max(0, g))^2 \tag{8.22}$$

In the battery model, both the N_{sc} and N_{pc} are integer valued design variables. Especially, the N_{pc} has only a few design possibilities within the bounds, so the MSA does not work well as it gets locked in the initial values of N_{pc}. The genetic algorithm can be a good alternative as the battery model is computationally simple. A population size of 100 with 20 generations has given consistent results for the optimum layout of battery cells. The standard stochastic transition rules such as mutation and crossover are employed for getting the genetically improved populations in the successive generations. The individual with maximum fitness value at the final generation is considered to be the optimum solution. On the other hand, the objective functions and constraints in the suspension model are continuously differentiable with respect to the continuous design variables, so the MATLAB implementation of sequential quadratic programming ($fmincon$) is utilised effectively for the accurate and computationally efficient results.

8.3 Hierarchical multi-objective optimisation

Optimising the subsystems separately and combining them together does not give the overall optimum solution. The synergistic solution can be achieved only when the interactions between the subsystems are maintained. The ATC algorithm manages the interactions using consistency constraints of the linking variables ($t_{ij} = r_{(i+1)j}$). It is important to relax these consistency constraints in order to ensure convergence of the problem [71]. Augmented-Lagrangian penalty function (ϕ) is used on the difference of linking variables as defined in (2.17).

The number of battery cells (N_{bc}) required from the vehicle model is cascaded down to the battery model as a target. Similarly, the sprung mass (m_1) and unsprung mass (m_2) of the vehicle which are calculated from the optimised design variables k_a, k_r, and N_{bc} as in (8.23) are passed to the suspension model.

$$\begin{aligned} m_1 &= k_r^2 k_a m_{motor,ref} + m_{fixed} \\ m_2 &= (m_{body} + N_{bs} m_{cell}\, k_{pc})/4 \end{aligned} \tag{8.23}$$

where $m_{motor,ref}$ is the mass of the reference motor, m_{fixed} is the mass of wheel end that is not influenced by scaling, m_{body} is the vehicle body mass, and m_{cell} is the battery cell mass. The battery pack to cell weight ratio (k_{pc}) is obtained through bench-marking the existing vehicle data and its value for Li-ion battery is ≈ 1.8. The shared variables P_{in} is formulated using the rated voltage (V_r) and the maximum current (I_{max}) of the motor.

$$P_{in} = \sqrt{3} V_r I_{max}$$

The subsystem level models verify if the targets from system model can be achieved without violating the local constraints. When the targets are not met, feedback is sent back by updating the linking variables, and the vehicle model is optimised again. When the consistency deviation between the target and response linking variables is within a predefined variable, the optimisation process is completed as presented in Table. 8.10. The hierarchical flowchart of the in-wheel motor electric vehicle model is given in Fig.8.8.

Table 8.10: *Evolution of consistency deviation considering gradeability limit of 30%. Stopping criteria:* $\epsilon_1 = \epsilon_2 = 0.01$

Iteration	$\|\|c_s^n\|\|$	$\|\|c_s^n - c_s^{n-1}\|\|$
1	inf	0.3873
2	0.3653	0.0253
3	0.0244	0.0031
4	0.0066	0.0058

In the proposed hierarchical multi-objective optimisation model, Pareto-optimal front between the objective functions in the vehicle model is generated using constraint method (8.24) [4, 59].

$$\min_{x \in \mathcal{F}} \; E_c + \phi_{11}$$
$$E_c \leq E_{batt} \quad N_{EM} P_{in} \leq P_{batt} \quad \Delta T \leq 60 \quad SPL \leq 15 \tag{8.24}$$

The results are plotted in Fig.8.9 between energy consumption and the inverse of gradability limit (GL), which converts GL to a minimisation function. Equivalent acceleration is also shown in the second x-axis. Similarly, the Pareto-optimal front of the suspension system, which is obtained by varying the weights (λ_i) in (8.19), is given between discomfort, road holding, and working space in Fig.8.10 for specific values of

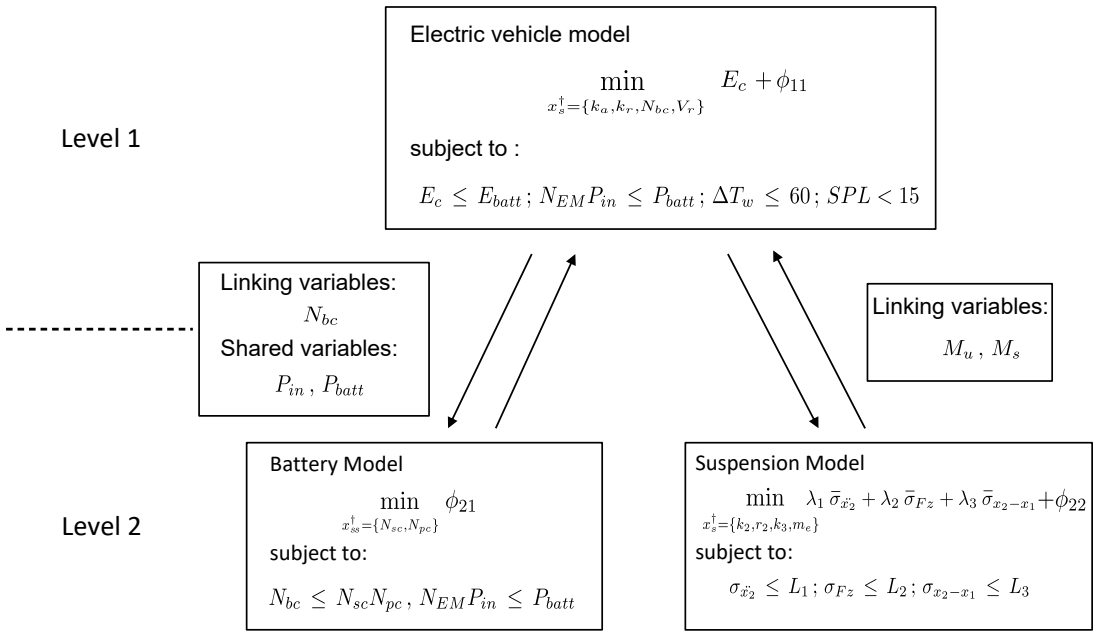

Fig. 8.8: *Hierarchical partitioning structure for in-wheel motor electric vehicle.*

m_1 and m_2. Optimum values of design parameters that correspond to two example vehicles, namely A and B as shown in the figures, are presented in Table. 8.11 along with the reference vehicle parameters. The vehicle A has the gradability limit of 55% and high weight for the discomfort. On the other hand, the vehicle B has 30% GL and high weight for the road holding. Thus the analytical target cascading together with MOO techniques can be used effectively to optimise the in-wheel motor electric vehicle.

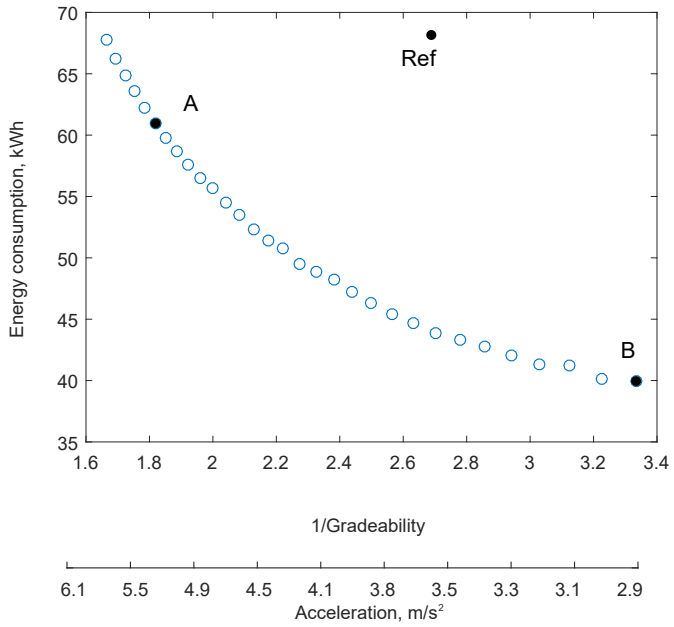

Fig. 8.9: *Pareto-optimal set between energy consumption and the inverse of gradeability limit.*

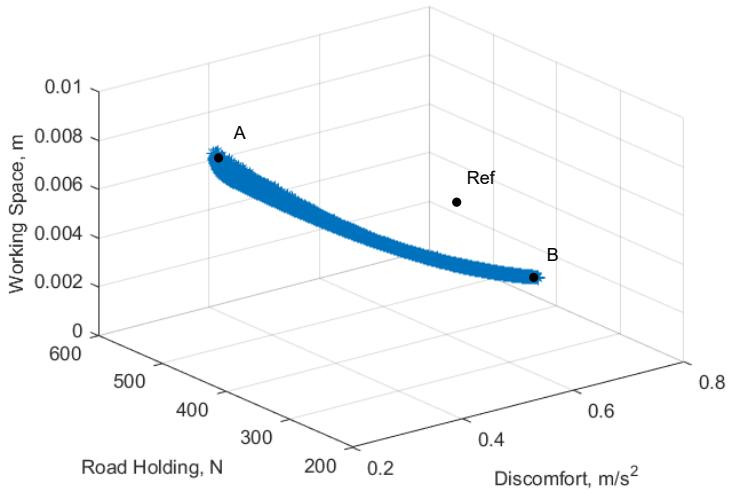

Fig. 8.10: *Pareto-optimal set of the suspension architecture S5 in the objective functions domain where* $m_2 = 310\text{kg}$ *and* $m_1 = 45\text{kg}$.

8.4 Comparison with All-in-one optimisation

The performance of proposed ATC based methodology is compared with the All-in-one (AiO) or single level optimisation model in terms of its accuracy and calculation time. Two different AiO models are considered in this study. In the first model, the vehicle mass is fixed before the optimisation. In other words, the vehicle mass does not change

Table 8.11: *Optimum values of the design parameters for vehicles A and B*

Parameters	Symbol	Reference	Optimum-A	Optimum-B
Pole number	$2p$	40	40	40
Slot number	Q_s	120	120	120
Magnet arc, %	α_p	0.75	0.75	0.75
Air gap length, mm	g	1.2	1.4	1.1
Inner rotor radius, mm	R_r	144.8	167.2	129.9
Inner magnet radius, mm	R_m	148.8	171.9	133.5
Outer stator radius, mm	R_s	150	173.3	134.6
Core length, mm	l_{stk}	66	79.2	69.8
Slot opening, mm	b_0	3.6	4.2	3.2
Slot depth, mm	d_s	13	15.0	11.7
Number of conductors in a slot	N_s	6	6	6
Maximum current, A	I_{max}	297.9	313.7	217.2
Rated voltage, V	V_r	200	153	153
Number battery cells	N_{bc}	200	444	312
Suspension spring stiffness, N/m	k_2	10000	14810	20000
Suspension damping ratio, Ns/m	r_2	1000	1230	1727
Additional spring stiffness, N/m	k_3	20000	5648	10476
Inerter equivalent mas, kg	m_e	200	144.8	231.6

with motor and battery sizes (the design variables). In the second model, the motor and battery sizes are used to estimate the vehicle mass while considering fixed values for the body and front axle masses. In order to generalise the models between the different approaches, a simplified multi-level optimisation model is built considering only the vehicle and battery models as in Fig. 8.11. The suspension model and the acoustic performance evaluation, discussed in Section 8.3, are not included as it is difficult to manage five objective functions together in the AiO formulation.

This multi-level optimisation problem is solved using the ATC approach as discussed in Section 8.3 and the Pareto optimal solutions between the energy consumption and inverse of gradability are given in Fig. 8.14.

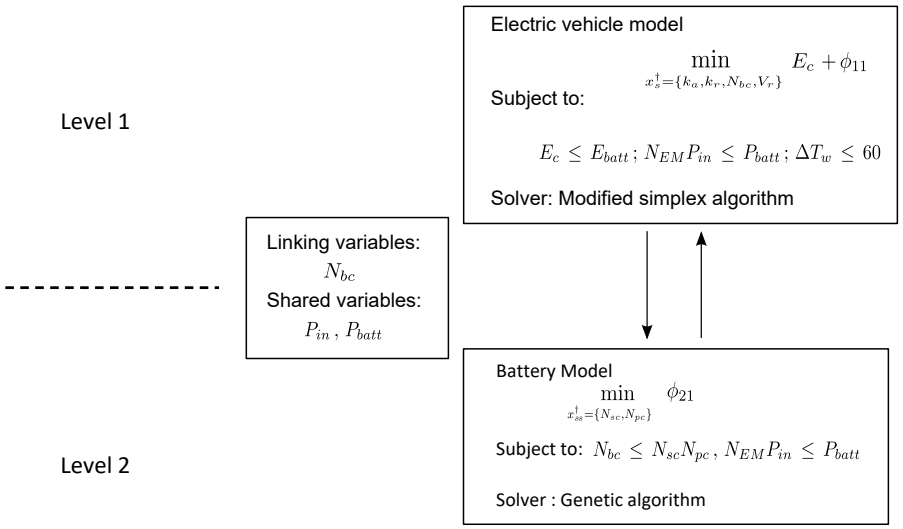

Fig. 8.11: *A simplified two level electric vehicle model*

8.4.1 All-in-one model with fixed vehicle mass

In the AiO approach, the electric vehicle and battery models are combined and optimised using a single solver. The objective functions are the energy consumption (E_C) and the inverse of gradability. The considered design variables are the axial and radial scaling ratios, maximum current, and rated voltage of the motor. The battery size is calculated from the optimised energy consumption and the rated voltage in post processing stage. The Pareto-optimal solutions between the energy consumption and inverse of gradeability are computed using constrained optimisation method defined in (2.4). The gradeability requirement is transformed into a constraint and the sequential quadratic programming (SQP) algorithm is used to solve the problem.

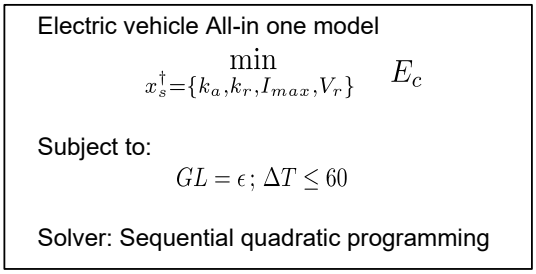

Fig. 8.12: *Problem formulation considering fixed vehicle mass*

8.4.2 All-in-one model considering the variations of vehicle mass

The variations of the vehicle mass can be captured in the optimisation process by modelling it as a function of motor scaling ratios and number of battery cells as given in (8.23). Similar to the fixed vehicle mass model, the energy consumption and inverse of gradability are taken as the objective functions. The design variables are radial and axial scaling ratios (k_a and k_r), maximum current (I_{max}), number of battery cells in series (N_{sc}) and parallel (N_{pc}).
As discussed in Section 8.2, the design variables N_{sc} and N_{pc} are integer valued functions which mandate the use of evolutionary algorithms to solve this non-linear optimization problem. Genetic algorithm is used to solve this mathematical programming problem.

Electric vehicle All-in one model

$$\min_{x_s^{\dagger}=\{k_a,k_r,I_{max},N_{sc},N_{pc}\}} \quad E_c$$

Subject to:

$$E_c \leq E_{batt}\,,\; N_{EM}P_{in} \leq P_{batt}\,,\; \Delta T_w \leq 60$$

Solver: Genetic algorithm

Fig. 8.13: *All-in one problem formulation considering the variations of vehicle mass*

8.4.3 Comparative analysis

The Pareto optimal sets from the proposed hierarchical method and AiO approaches are compared in Fig. 8.14 where the benefit of modelling the vehicle mass as a function of the motor and battery sizes is evident. When the gradability or acceleration demand is high, the motor size should be scaled up in order to achieve the required torque. This results in increased vehicle mass and energy consumption. Conversely, when the gradability or acceleration requirement is low, the actual energy consumption will be lower than the estimation of the fixed vehicle mass model.

Table 8.12: *Calculation time of the optimisation methods.*

Optimisation model	Calculation time, s
Proposed optimization methodology based on ATC	440
All-in-one model with fixed vehicle mass	111
All-in-one model considering the variation of vehicle mass	4601

The AiO approach with fixed vehicle mass does not capture this effect and estimates lower energy consumption as shown in Fig. 8.14. On the other hand, the AiO approach

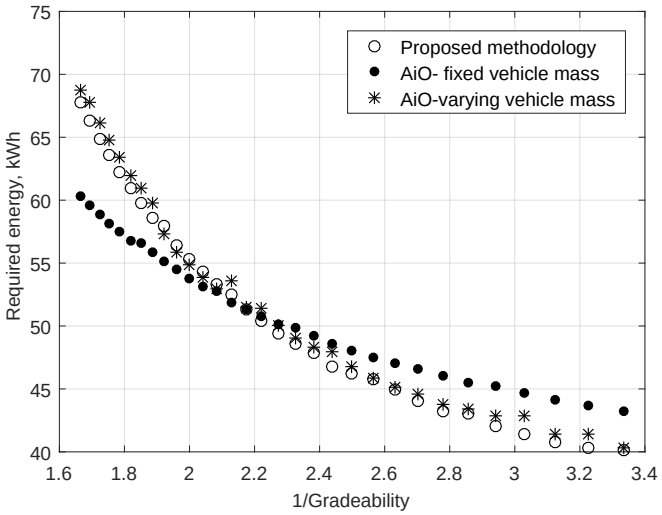

Fig. 8.14: *Comparison of Pareto optimal sets obtained from AiO optimisation models and proposed methodology*

considering the vehicle mass variation gives similar results with respect to proposed ATC based method. However, the computational time of the evolutionary algorithms required to solve this problem is unacceptable. Table 8.12 compares the calculation time of all the three formulations.

From the shown results, it can be suggested that the proposed ATC based optimisation algorithm is quite useful in the pre-design stage of complex systems such as in-wheel motor electric vehicles in achieving accurate solutions with reasonable calculation time.

CHAPTER 9

Conclusion

This thesis analysed the modelling techniques of in-wheel motor electric vehicles and proposed a decomposition based multi-objective optimisation approach for sizing the vehicle components. The considered optimisation problem involves multi-disciplinary subsystems such as electric motor, power electronics, battery, and suspension with complex interactions between them. The subsystems consist multiple design objectives to be handled simultaneously. In order to solve such a complex system, analytical target cascading (ATC) algorithm was used in combination with multi-objective optimisation (MOO) techniques. As per the proposed methodology, the electric vehicle model was partitioned into manageable subsystems and the objective functions that belong to each subsystem were treated together using MOO techniques. Appropriate optimisers were used to solve the subsystems individually and the ATC coordination strategy was used to achieve the overall synergistic solution.

Conclusions from chapters

It is important to use accurate and computationally effective models for the success of optimisation. Hence, a comparative analysis of electromagnetic models was performed for the surface permanent magnet machine. The air-gap field solutions and the global parameters including cogging torque, total torque, and back-emf waveforms were calculated using six different techniques and compared with the results from finite element analysis. The modelling complexity of each method was quantified in terms of the back-emf waveform computation time. For this particular application and eval-

uation criteria, the most accurate result compared to finite element model (FEM) was obtained from the MM technique, and its calculation time was two order of magnitude less than the FEM. Although the tangential field component of the complex relative permeance model had some deviations, its radial field component was accurate. The closed form solutions of the global parameters, offered by this model, reduced the computational effort significantly. The harmonic model and semi-analytical conformal mapping method were accurate and at the same time computationally expensive. The results of the Carter factor and relative permeance models were comparatively inaccurate. Therefore, the analytical motor model was developed based on the complex relative permeance electromagnetic model and compared with the motor scaling approaches such as proportional scaling of efficiency map, Willans line model, and scalable saturated motor model. The baseline efficiency maps of the reference and scaled motors were created using Motor-CAD software. By comparing the efficiency maps obtained from the motor scaling models, the analytical motor model was chosen as the appropriate method for the optimisation problem formulation.

As the performance of electric motor was affected by the magnet and winding temperatures, a coupled electromagnetic-thermal model was developed in this study. The copper losses were observed to be high at low speed and high torque region due to its dependency on the winding temperature. It was noted from the results that the iron losses in the stator decreased as the magnet temperature increased. The variations in the magnet losses were negligible. In order to assess the implications of the differences observed in the calculated losses or efficiencies on a real world application, the energy consumption of an electric vehicle in New European Driving Cycle (NEDC) was computed with and without the thermal model. A difference of $\approx 2\%$ was observed in the calculated energy requirements. A rough but reasonable way to account for the temperature effects on the energy consumption calculations, without the thermal model, was to use the average driving cycle temperature for the magnet and winding. Using the coupled electromagnetic-thermal model, temperature evolutions of the end-winding and magnet were predicted on a particular motor operating condition. The same model was used to estimate the gradability of the vehicle considering peak motor torque in the optimisation process.

Though the noise is a subjective measure, an understanding of the acoustic performance of the electric machines can be useful in the early optimisation process. A 1D multiphysics model was developed for the combined electromagnetic and vibroacoustic simulations. The radial component of Maxwell stress tensor, which was calculated from the air-gap field solutions, gave the radial force distribution. The intrinsic structural dynamics of the rotating member (rotor and housing) was calculated using a ring model

with equivalent properties and validated with the FEM results. The induced vibrations due to the radial force distribution allowed the computation of acoustic pressure levels assuming an infinite cylinder radiator for the outer rotor. The model was simplified significantly in order to be included in the optimisation process.

It is important to optimise the suspension parameters along with the other subsystems like electric motor and battery to accommodate the variations in sprung and unsprung masses. In addition, the performance improvements offered by the inerter and relaxation spring were studied. Six suspension architectures with the suspension components arranged in different configurations have been considered. A general approach for deriving the objective functions of the suspension architectures such as discomfort, road holding, and working space was presented. Multi-objective optimisation was carried to obtain the Pareto-optimal sets of all the architectures, and the results were compared in the objective functions domain. The addition of inerter and relaxation spring in the architecture S5 gave improvements over S1 in all the objective functions. On the contrary, the architectures S3 and S4 did not provide any improvements. The additional spring in S2 improved the road holding, and the inerter in architecture S6 did not give any significant improvement over S2. The results showed that the architecture S5 can be used to improve the suspension performance of the in-wheel motor electric vehicles.

The interactions between the subsystems should be maintained to obtain consistent optimal solutions. The ATC algorithm manages the interactions using consistency constraints. In the in-wheel motor electric vehicle problem formulation, the vehicle model, along with the electric motor and power electronics models, was considered at the top level, and the other subsystem models (suspension and battery) were studied at the bottom level. The linking variables (number of battery cells, sprung, and unsprung masses) and the shared variables (motor input power and battery output power) confirmed the interactions between the subsystems. A modified simplex algorithm was proposed to optimise the vehicle model with integer valued design variables, which worked faster than the evolutionary algorithms. The battery and suspension models were solved using a genetic algorithm and sequential quadratic programming respectively. The Pareto-optimal solutions for the vehicle and suspension models were obtained by solving the complete vehicle problem synergistically each time.

The benefits of proposed method were studied by comparing it with the AiO optimisation approach. A simplified vehicle optimisation problem was considered for this study. Two different AiO models were formulated. In the first model, the vehicle mass was fixed and it was assumed not to change with the motor and battery sizes. This assumption simplified the model considerably. A standard non-linear programming al-

gorithm (SQP) was used to obtain the results with minimum calculation time. On the other hand, the vehicle mass was defined as a function of the motor and battery sizes in the second model for improved model accuracy. As the number battery cells was a discrete valued design variable, evolutionary optimisation algorithms were used which resulted in high computation time. The second model was effectively solved using the proposed ATC based algorithm which gave similar accuracy as that of AiO model with a significant reduction in computation time. When the modelling complexity is really high (more than three objective functions) such as the in-wheel motor electric vehicle problem, the implementation of AiO algorithm might be impractical. For such complex systems, the proposed hierarchical multi-objective optimisation algorithm can effectively be employed.

Synthesis and Future developments

Hierarchical multi-objective programming was introduced and its usefulness for solving complex engineering problems was demonstrated. This approach will help the designers to obtain the Pareto-optimal design solutions considering all the relevant models of subsystems together. Electric motor modelling techniques for surface PM machines were compared and their performance differences were discussed in details. The benefits of passive suspension components such as inerter and relaxation spring were analysed for improved suspension performances. Analytical coupled models were presented for electromagnetic-thermal calculations as well as electromagnetic-vibroacoustic simulations.
As a part of the future work, the following topic should be further addressed to augment the scope of this thesis:

1. Electric vehicle architectures with interior permanent magnet (IPM) machines or magnet-less machines should be optimised. The scalable saturated motor model, similar to the one discussed in this thesis for PM machines, can be used to estimate the motor performances. A thermal model should be coupled with the scalable SFLL model to study the overloading capabilities of the machines.

2. The proposed optimisation method should be tested against more complex design problems including hybrid vehicles. The ATC coordination algorithm should be exploited for hierarchical models with more than two levels.

Appendices

APPENDIX $\mathcal{A}$

Calculation of the flux linkage in d-axis

In order to calculate the $\psi_{(pm-d)}$, the flux linkage of phase windings is mapped to d-q reference frame using Park transformation. The transformation matrix is given as

$$T = \begin{bmatrix} cos(\theta) & cos(\theta - \frac{2\pi}{3}) & cos(\theta + \frac{2\pi}{3}) \\ -sin(\theta) & -sin(\theta - \frac{2\pi}{3}) & -sin(\theta + \frac{2\pi}{3}) \\ \frac{1}{2} & \frac{1}{2} & \frac{1}{2} \end{bmatrix} \tag{A.1}$$

The permanent magnet flux linkage in d-axis is

$$\psi_{(pm-d)}(t) = \psi_a cos(\omega t) + \psi_b cos(\omega t - \frac{2\pi}{3}) + \psi_c cos(\omega t + \frac{2\pi}{3}) \tag{A.2}$$

where ψ_a, ψ_b, ψ_c are the flux linkages of the phase windings A, B,and C respectively. The flux linkage of phase windings is calculated by integrating the radial air gap permanent magnet flux density across a coil pitch (ψ_c) and by summing it vectorially across the number of coils connected in series. The ψ_c is given as,

$$\psi_c(t) = l_a R \int_{-\frac{\gamma_c}{2}}^{\frac{\gamma_c}{2}} B_{sr}(R, \theta, t) d\theta \tag{A.3}$$

where B_{sr} is the radial component of no-load field distribution in the slotted air gap which is obtained by multiplying slotless air gap flux density, from (3.31) to (3.34), and complex relative permeance in (3.89).

$$B_s = B_{sr} + jB_{s\theta} = B_k \lambda^* = (B_r \lambda_a + B_\theta \lambda_b) + j(B_\theta \lambda_a + B_r \lambda_b) \tag{A.4}$$

So the radial and tangential components of the flux density in (A.4) can be written when the coil pitch is an odd integer of slot pitch as [111],

$$\begin{aligned} B_{sr} = B_r\lambda_a + B_\theta\lambda_b =& \lambda_0 \sum_n B_{rn}\cos[np(\theta-\alpha)] + \\ & \sum_n\sum_m B_{rn}\lambda_{am}\cos[np(\theta-\alpha)]\cos(mQ_s\theta) + \\ & \sum_n\sum_m B_{\theta n}\lambda_{bm}\sin[np(\theta-\alpha)]\sin(mQ_s\theta) \end{aligned} \tag{A.5}$$

$$\begin{aligned} B_{s\theta} = B_\theta\lambda_a - B_r\lambda_b =& \lambda_0 \sum_n B_{\theta n}\sin[np(\theta-\alpha)] + \\ & \sum_n\sum_m B_{\theta n}\lambda_{am}\sin[np(\theta-\alpha)]\cos(mQ_s\theta) - \\ & \sum_n\sum_m B_{rn}\lambda_{bm}\cos[np(\theta-\alpha)]\sin(mQ_s\theta) \end{aligned} \tag{A.6}$$

By substituting (A.5) in (A.3),

$$\begin{aligned} \psi_c(t) =& l_a R\sum_n \Bigg\{ \lambda_0 B_{rn} 2\frac{1}{np} sin\left(np\frac{\gamma c}{2}\right) + \\ & \sum_m (B_{rn}\lambda_{am} - B_{\theta n}\lambda_{bm})\frac{1}{np+mQ_s} sin\left[(np+mQ_s)\frac{\gamma c}{2}\right] + \\ & \sum_m (B_{rn}\lambda_{am} + B_{\theta n}\lambda_{bm})\frac{1}{np-mQ_s} sin\left[(np-mQ_s)\frac{\gamma c}{2}\right] \Bigg\} cos(np\omega_{rm}t) \end{aligned} \tag{A.7}$$

when $np = mQ_s$, the term

$$\frac{1}{np-mQ_s} sin\left[(np-mQ_s)\frac{\gamma_c}{2}\right]$$

should be replaced with $\frac{\gamma_c}{2}$ [111].

Phaser sum of the flux linkages in the coils connected in series gives the total flux linkage in a phase. The distribution factor of an integer slot winding that takes care of the phaser sum is given for its n^{th} harmonic in (A.8).

$$k_{dn} = \frac{sin\left(np\frac{\alpha}{2}\right)}{q\sin\left(n\frac{\alpha}{2}\right)} \tag{A.8}$$

where q is the number of slots per pole per phase and α is the phase shift between two adjacent coils. The total number of turns per phase connected in series is given by

$$N_s = \begin{cases} N_c\frac{Qc}{2ma_p}, \text{for a single-layer winding} \\ N_c\frac{Qs}{ma_p}, \text{for a two-layer winding} \end{cases} \tag{A.9}$$

In the above equation, α_p is number parallel paths. The final expression for the flux linkage in a phase can be given as,

$$\begin{aligned}\psi_{phase}(t) =& N_s l_a R \sum_n k_{dn} \Bigg\{ \lambda_0 B_{rn} 2 \frac{1}{np} sin\left(np\frac{\gamma c}{2}\right) + \\ & \sum_m (B_{rn}\lambda_{am} - B_{\theta n}\lambda_{bm}) \frac{1}{np + mQ_s} sin\left[(np + mQ_s)\frac{\gamma_c}{2}\right] + \\ & \sum_m (B_{rn}\lambda_{am} + B_{\theta n}\lambda_{bm}) \frac{1}{np - mQ_s} sin\left[(np - mQ_s)\frac{\gamma_c}{2}\right] \Bigg\} cos(np\omega_{rm}t - \beta_0)\end{aligned} \tag{A.10}$$

The angle β_0 is zero for phase A, $2\pi/3$ for phase B, and $4\pi/3$ for phase C.

APPENDIX B

Calculation of the electric motor inductance

Armature field solution in the air gap, which can be calculated using conformal mapping, is used to derive the self (L_s) and mutual (L_m) inductances. In addition, the slot leakage inductance and end-winding inductance are also considered. For the calculation of armature field solution, the air gap of the slotted geometry is mapped to a canonical domain as suggested in [111] for an inner rotor PM machine. The derivation is repeated for the external rotor PM machine here. While mapping the air gap, only half of the slot is considered as the potentials in the adjacent teeth of a slot are $I\frac{N_c}{2}$ and $-I\frac{N_c}{2}$ with respect to the zero potential rotor surface and slot centre. The steps followed in the conformal mapping process are given in Fig. B.1

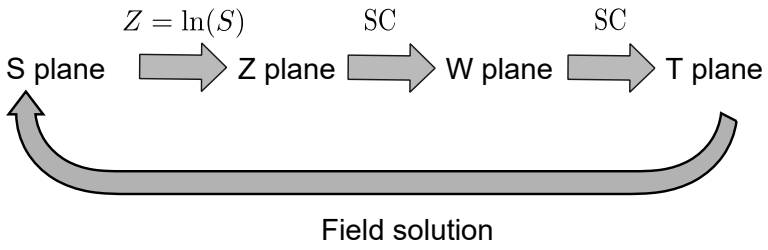

Fig. B.1: *Steps involved in converting the slotted air gap geometry into a infinite long parallel plates and finding the field solution*

Similar to the conformal mapping performed for the permanent magnet field calculation in Section 3.1.3, the logarithmic transformation is used to map the S-plane shown in

Fig. B.2 to the Z-plane in Fig. B.3.

$$z = log(s) \tag{B.1}$$

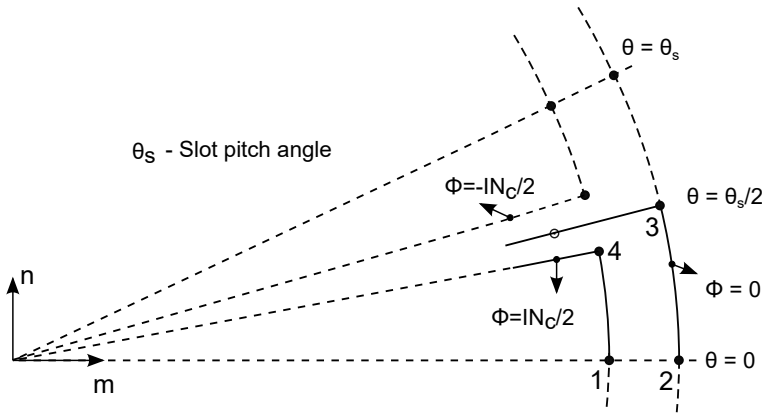

Fig. B.2: *One half of the slot opening in S-plane*

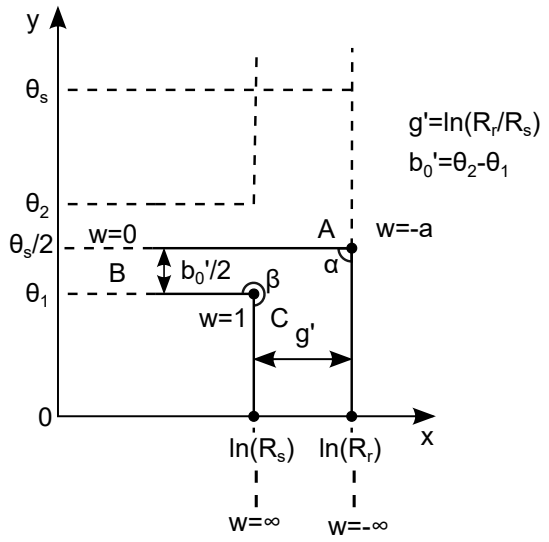

Fig. B.3: *One half of the slot opening in Z-plane*

The Schwarz-Christoffel equation gives the differential from transformation equation between Z-plane and W-plane as given below.

$$\frac{dz}{dw} = A(w - w_a)^{\frac{\alpha}{\pi}-1}(w - w_b)^{\frac{\beta}{\pi}-1}(w - w_c)^{\frac{\gamma}{\pi}-1} \tag{B.2}$$

In (B.2), the two of these constants w_a, w_b,and w_c are given convenient values and the other constant value is derived from the geometry. α, β, and γ are the inner angles of the corners A,B,and C shown in Fig. B.3.

$$\frac{dz}{dw} = A\frac{(w-1)^{\frac{1}{2}}}{(w)(w+a)^{\frac{1}{2}}} \tag{B.3}$$

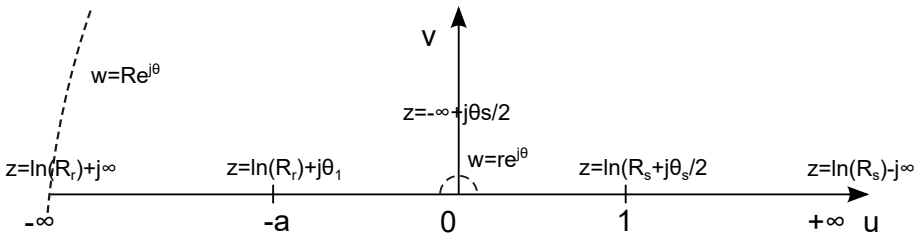

Fig. B.4: *One half of the slot opening in W-plane*

Equation B.3 is integrated using substitution method,

$$p^2 = \frac{w+a}{w-1} \tag{B.4}$$

$$dz = \frac{-2A(a+1)}{(p^2+a)(p^2-1)} \tag{B.5}$$

After taking partial fraction

$$dz = \frac{2A}{(p^2+a)} + \frac{2A}{(1-p^2)} \tag{B.6}$$

Equation B.6 can be integrated as

$$z = 2A\left[\frac{1}{\sqrt{a}}\arctan\left(\frac{p}{a}\right) + \frac{1}{2}\ln\left(\frac{1+p}{1-p}\right)\right] + C \tag{B.7}$$

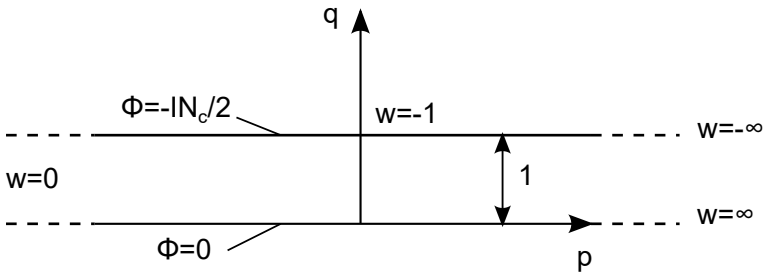

Fig. B.5: *One half of the slot opening in T-plane*

The value of A can be calculated by integrating B.3 in the w-plane along a semi-circle with the radius approaching infinity ($w = Re^{j\theta}$) and equating it to corresponding value in Z-plane.

$$\int(dz) = \int_0^{\pi} \frac{A(Re^{j\theta}-1)^{\frac{1}{2}}}{Re^{j\theta}(Re^{j\theta}+a)^{\frac{1}{2}}} jRe^{j\theta}d\theta = \int_0^{\pi} jAd\theta \tag{B.8}$$

In the Z-plane $\int dz = g'$, so

$$A = -j\frac{g'}{\pi} \tag{B.9}$$

Similarly the value of a is derived by integrating B.3 in the w-plane along a semi-circle with the radius approaching zero ($w = re^{j\theta}$).

$$\int (dz) = \int_0^{\pi} \frac{A(re^{j\theta}-1)^{\frac{1}{2}}}{re^{j\theta}(re^{j\theta}+a)^{\frac{1}{2}}} jre^{j\theta}d\theta = \int_0^{\pi} \frac{A(-1)^{\frac{1}{2}}}{re^{j\theta}(a)^{\frac{1}{2}}} jre^{j\theta}d\theta = j\frac{g'}{\sqrt{a}} \tag{B.10}$$

In the Z-plane $\int dz = j\frac{b'_0}{2}$, so

$$a = \left(\frac{2g'}{b'_0}\right)^2 \tag{B.11}$$

The integration constant in B.7 is calculated by evaluating the value of z at one of the known vertices.
When $w \to a$, $p = 0$

$$z = 2A\left[\frac{1}{\sqrt{a}}\arctan\left(\frac{0}{a}\right) + \frac{1}{2}\ln(1)\right] + C \tag{B.12}$$

From the Fig. B.3, $z = ln(Rr) + j\frac{\theta_s}{2}$

$$C = ln(Rr) + j\frac{\theta_s}{2} \tag{B.13}$$

In the T-plane, the location and the distance between to the plates can be set arbitrarily. If the lower plate is aligned with the real axis of T-plane and the distance to upper plane is 1, then the transformation can be formulated as,

$$t = \frac{1}{\pi}\ln(w) \tag{B.14}$$

The lower plate potential is observed to be $\varphi = 0$ and of the upper plate is $\varphi = -\frac{Nc}{2}I$. N_c is number of conductors in a slot and I is the current in each conductor. Inside the plates, the potential term changes only along the imaginary axis, so the field solution in the T-plan can be written as.

$$B_t = -j\mu_0\frac{\partial\varphi}{\partial q} = j\mu_0\frac{N_c}{2}I \tag{B.15}$$

The field solution in S-plane is mapped from B_t

$$B_s = B_t\left(\frac{\partial t}{\partial s}\right)^* = B_t\left(\frac{\partial t}{\partial w}\frac{\partial w}{\partial z}\frac{\partial z}{\partial s}\right)^* \tag{B.16}$$

where

$$\begin{aligned}
\frac{\partial t}{\partial w} &= \frac{1}{\pi}\frac{1}{w} \\
\frac{\partial w}{\partial z} &= j\frac{\pi}{g'}\frac{w(w+a)^{\frac{1}{2}}}{(w-1)^{\frac{1}{2}}} \\
\frac{\partial z}{\partial s} &= \frac{1}{s}
\end{aligned} \tag{B.17}$$

Substituting (B.17) in (B.16),

$$B_s = B_m + jB_n = \mu_0 \frac{N_c}{2g'} I \left(\frac{1}{s} \sqrt{\frac{w+a}{w-1}} \right)^* \tag{B.18}$$

As the field solution in the canonical domain B_T is given in Cartesian coordinates, the resulting field solution B_s is also in Cartesian coordinates, which are converted to cylindrical coordinates according to (B.19).

$$\begin{aligned} B_{ar} &= B_m \cos\theta + B_n \sin\theta \\ B_{a\theta} &= -B_m \sin\theta + B_n \cos\theta \end{aligned} \tag{B.19}$$

The solution from (B.19) represents the field produced by a single slot with 1A of current. In order to get the total armature flux in the air gap, the contribution from each slot should be added together based on the methodology detailed by Zarko in [111]. The entire armature field solution at the center of air gap can be written in the form

$$\begin{aligned} B_{ar}(r,\theta,t) =& N_c \sum_{i=1}^{\frac{Q_s}{m}} \sum_{n=1}^{N_a} B_{arn}(r) \{ (i_A(t) sgn_{A_i} \cos[n(\theta - \alpha_{A_i})] + \\ & i_B(t) sgn_{B_i} \cos[n(\theta - \alpha_{B_i})] + i_c(t) sgn_{C_i} \cos[n(\theta - \alpha_{C_i})] \} \end{aligned} \tag{B.20}$$

$$\begin{aligned} B_{a\theta}(r,\theta,t) =& N_c \sum_{i=1}^{\frac{Q_s}{m}} \sum_{n=1}^{N_a} B_{a\theta n}(r) \{ i_A(t) sgn_{A_i} \sin[n(\theta - \alpha_{A_i})] + \\ & i_B(t) sgn_{B_i} \sin[n(\theta - \alpha_{B_i})] + i_c(t) sgn_{C_i} \sin[n(\theta - \alpha_{C_i})] \} . \end{aligned} \tag{B.21}$$

where i_A, i_B, and i_C are the phase current magnitudes, sgn_A, sgn_B, sgn_C are the current directions in each coil, N_c is the number of coils in a slot, and Q_s is the number coils connected in series. The above (B.21) assumes the relative permeance of magnet as 1, but in reality it is slightly higher (1.05). The influence of higher permeance on the armature flux is captured by multiplying the analytical solution with a relative permeance function. The slotless air gap permeance Λ_{gsl} in the region without magnets is defined as,

$$\Lambda_{gsl} = \frac{\mu_0}{g + l_m} \tag{B.22}$$

and with magnets,

$$\Lambda_{gmsl} = \frac{\mu_0}{g'} = \frac{\mu_0}{g + \frac{lm}{\mu_r}} \tag{B.23}$$

The relative air gap permeance can be generalised as

$$\lambda_{gsl} = \begin{cases} \frac{\Lambda_{gmsl}}{\Lambda_{gsl}} = \frac{g+l_m}{g+\frac{l_m}{\mu_r}} = \lambda_{gm}, & \text{where the magnets are present} \\ 1, & \text{where the magnets are not present} \end{cases} \tag{B.24}$$

where l_m is the magnet height and g is the air gap height. The relative permeance function waveform is observed to be periodic even function, so it can be written in the Fourier form as

$$\lambda_{gsless} = \lambda_{g0} + \sum_{n=1}^{\inf} \lambda_{gn} \cos[2np(\theta - \alpha)] \tag{B.25}$$

where

$$\lambda_{g0} = \frac{2p}{\pi} \int_0^{\frac{\pi}{2p}} \lambda_{gsless}(\theta) d\theta = 1 + \alpha_p(\lambda_g m - 1)$$

$$\lambda_{gn} = \frac{4p}{\pi} \int_0^{\frac{\pi}{2p}} \lambda_{gsless}(\theta) \cos(2np\theta) d\theta = \frac{2}{n\pi} \sin(n\alpha_p \pi)(\lambda_g m - 1).$$

The term α accounts for the magnet rotation as the permeance function rotates along with the rotor magnets. The armature field solution (B.21) is multiplied with the relative permeance function to get much better agreement with FEM results. The radial and tangential components of armature flux after multiplying them with the relative permeance function are given in (B.26), (B.27).

$$\begin{aligned} B_{ar}(r,\theta,t) =& N_c \lambda_{g0} \sum_{i=1}^{Q_{coil}} \sum_{n=1}^{N_a} B_{arn}(r) \{(i_A(t) sgn_{A_i} \cos[n(\theta - \alpha_{A_i})] + \\ & i_B(t) sgn_{B_i} \cos[n(\theta - \alpha_{B_i})] + i_c(t) sgn_{C_i} \cos[n(\theta - \alpha_{C_i})]\} + \\ & N_c \lambda_{g0} \sum_{i=1}^{Q_{coil}} \sum_{n=1}^{N_a} \sum_{h=1}^{\inf} \lambda_{gh} B_{arn}(r) \{(i_A(t) sgn_{A_i} \cos[n(\theta - \alpha_{A_i})] + \\ & i_B(t) sgn_{B_i} \cos[n(\theta - \alpha_{B_i})] + i_c(t) sgn_{C_i} \cos[n(\theta - \alpha_{C_i})]\} \cos[2hp(\theta - \alpha)] \end{aligned} \tag{B.26}$$

$$\begin{aligned} B_{a\theta}(r,\theta,t) =& N_c \lambda_{g0} \sum_{i=1}^{Q_{coil}} \sum_{n=1}^{N_a} B_{a\theta n}(r) \{(i_A(t) sgn_{A_i} \cos[n(\theta - \alpha_{A_i})] + \\ & i_B(t) sgn_{B_i} \cos[n(\theta - \alpha_{B_i})] + i_c(t) sgn_{C_i} \cos[n(\theta - \alpha_{C_i})]\} + \\ & N_c \lambda_{g0} \sum_{i=1}^{Q_{coil}} \sum_{n=1}^{N_a} \sum_{h=1}^{\inf} \lambda_{gh} B_{a\theta n}(r) \{(i_A(t) sgn_{A_i} \cos[n(\theta - \alpha_{A_i})] + \\ & i_B(t) sgn_{B_i} \cos[n(\theta - \alpha_{B_i})] + i_c(t) sgn_{C_i} \cos[n(\theta - \alpha_{C_i})]\} \cos[2hp(\theta - \alpha)] \end{aligned} \tag{B.27}$$

where

$$Q_{coil} = \begin{cases} \frac{Q_s}{3}, & \text{for two-layer winding} \\ \frac{Q_s}{6}, & \text{for single-layer winding} \end{cases}$$

The radial component of the armature flux density B_{ar} due to phase A current is integrated across a coil of phase A winding and summed with the flux linkages of the remaining phase A coil to get the total flux linkage of phase A.

$$\psi_a(t) = l_a R N_c^2 \sum_{j=1}^{Q_{coil}} \mathrm{sgn}_{Aj} \int_{-\frac{\gamma_c}{2}+\alpha_{Aj}}^{\frac{\gamma_c}{2}+\alpha_{Aj}} \sum_{i=1}^{Qcoil} \sum_{n=1}^{N_a} B_{arn}(R)\lambda_{g0} i_A(t) \mathrm{sgn}_{Ai} \cos[n(\theta-\alpha_{Ai})]d\theta +$$
$$l_a R N_c^2 \sum_{j=1}^{Q_{coil}} \mathrm{sgn}_{Aj} \int_{-\frac{\gamma_c}{2}+\alpha_{Aj}}^{\frac{\gamma_c}{2}+\alpha_{Aj}} \sum_{i=1}^{Qcoil} \sum_{n=1}^{N_a} \sum_{h=1}^{\infty} B_{arn}(R)\lambda_{gh} i_A(t) \mathrm{sgn}_{Ai}$$
$$\cos[n(\theta-\alpha_{Ai})] \cos[2hp(\theta-\alpha)]d\theta \tag{B.28}$$

The self inductance is given by $L_a = \frac{\psi_a}{i_a}$.

$$L_a = l_a R N_c^2 \sum_{j=1}^{Q_{coil}} \sum_{i=1}^{Qcoil} \sum_{n=1}^{N_a} B_{arn}(R)\lambda_{g0} \frac{2}{n} \mathrm{sgn}_{Aj} \mathrm{sgn}_{Ai} \cos[n(\alpha_{Aj}-\alpha_{Ai})] \sin\left(n\frac{\gamma_c}{2}\right) +$$
$$l_a R N_c^2 \sum_{j=1}^{Q_{coil}} \sum_{i=1}^{Qcoil} \sum_{n=1}^{N_a} \sum_{h=1}^{\infty} B_{arn}(R)\lambda_{gh} \mathrm{sgn}_{Aj} \mathrm{sgn}_{Ai} \left\{ \frac{1}{n+2hp} \cos\left[n(\alpha_{Aj}-\alpha_{Ai}\right.\right.$$
$$\left. +2hp(\alpha_{Aj}-\alpha)\right] sin\left[(n+2hp)\frac{\gamma_c}{2}\right] + \frac{1}{n-2hp} \cos[n(\alpha_{Aj}-\alpha_{Ai}) - 2hp(\alpha_{Aj}-\alpha)]$$
$$\left. \sin\left[(n+2hp)\frac{\gamma_c}{2}\right] \right\} \tag{B.29}$$

when $n = 2hp$

$$\frac{1}{n-2hp} \sin\left[(n+2hp)\frac{\gamma_c}{2}\right] \tag{B.30}$$

is replaced with $\frac{\gamma_c}{2}$.

The flux linkage of phase A winding due to the phase B current (ψ_{ab}) is estimated in (B.31) and the mutual inductance is calculated as $L_{ab} = \frac{\psi_{ab}}{i_b}$.

$$\psi_{ab}(t) = l_a R N_c^2 \sum_{j=1}^{Q_{coil}} \mathrm{sgn}_{Aj} \int_{-\frac{\gamma_c}{2}+\alpha_{Aj}}^{\frac{\gamma_c}{2}+\alpha_{Aj}} \sum_{i=1}^{Qcoil} \sum_{n=1}^{N_a} B_{arn}(R)\lambda_{g0} i_B(t) \mathrm{sgn}_{Ai} \cos[n(\theta-\alpha_{Bi})]d\theta +$$
$$l_a R N_c^2 \sum_{j=1}^{Q_{coil}} \mathrm{sgn}_{Aj} \int_{-\frac{\gamma_c}{2}+\alpha_{Aj}}^{\frac{\gamma_c}{2}+\alpha_{Aj}} \sum_{i=1}^{Qcoil} \sum_{n=1}^{N_a} \sum_{h=1}^{\infty} B_{arn}(R)\lambda_{gh} i_B(t) \mathrm{sgn}_{Bi}$$
$$\cos[n(\theta-\alpha_{Bi})] \cos[2hp(\theta-\alpha)]d\theta \tag{B.31}$$

$$L_{ab} = l_a R N_c^2 \sum_{j=1}^{Q_{coil}} \sum_{i=1}^{Qcoil} \sum_{n=1}^{N_a} B_{arn}(R)\lambda_{g0}\frac{2}{n}\mathrm{sgn}_{Aj}\mathrm{sgn}_{Bi}\cos[n(\alpha_{Aj}-\alpha_{Bi})]\sin\left(n\frac{\gamma_c}{2}\right) +$$
$$l_a R N_c^2 \sum_{j=1}^{Q_{coil}} \sum_{i=1}^{Qcoil} \sum_{n=1}^{N_a} \sum_{h=1}^{\infty} B_{arn}(R)\lambda_{gh}\mathrm{sgn}_{Aj}\mathrm{sgn}_{Bi}\left\{\frac{1}{n+2hp}\cos\left[n(\alpha_{Aj}-\alpha_{Bi})\right.\right.$$
$$\left.+2hp(\alpha_{Aj}-\alpha)\right] sin\left[(n+2hp)\frac{\gamma_c}{2}\right] + \frac{1}{n-2hp}\cos[n(\alpha_{Aj}-\alpha_{Bi})-2hp(\alpha_{Aj}-\alpha)]$$
$$\left.\sin\left[(n+2hp)\frac{\gamma_c}{2}\right]\right\} \tag{B.32}$$

when $n = 2hp$

$$\frac{1}{n-2hp}\sin\left[(n+2hp)\frac{\gamma_c}{2}\right]$$

is replaced with $\frac{\gamma_c}{2}$.

Considering straight parallel slot shown in Fig B.6, the slot leakage inductance is formulated with the assumption of infinite permeable core [130, 131] as

$$L_{sl} = \mu_0 \frac{Q_s}{3a_p^2} N_c^2 l_a \left(\frac{h1}{3b} + \frac{h2}{b}\right). \tag{B.33}$$

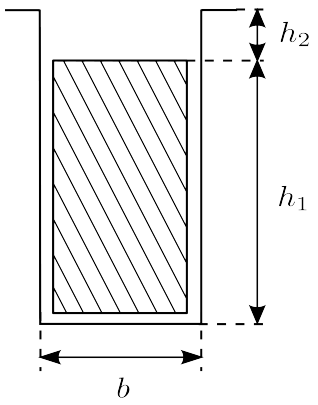

Fig. B.6: *Slot geometry of a single layer winding*

The end winding leakage inductance is rather small and depends on the three dimensional flux paths produced by the currents flowing in the end windings. In addition the geometry of the end windings is also complicated to be modelled. Hence, the analytical solutions given by Liwschitz-Garik [132], which was observed to give results in the same order of magnitude compared to detailed models in [111], is employed.

$$L_{ew} = 2\mu_0 \frac{N_s^2}{p} k_p k_d 2.4(l_{e2} + \frac{l_{e1}}{2}) \tag{B.34}$$

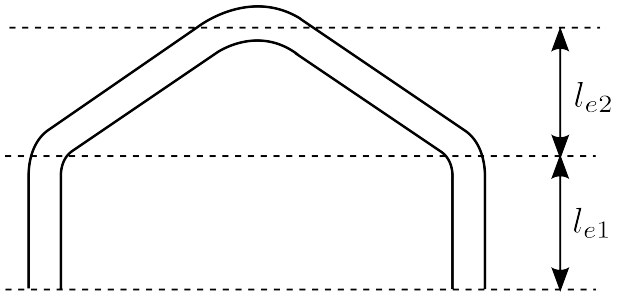

Fig. B.7: *Model of an end coil*

The total phase inductance (L) can be calculated as in (B.35) which should be closely equal to the inductance in d-axis (L_d) for the SPM machines.

$$L = L_s + L_{ew} + L_{sl} - L_m \tag{B.35}$$

APPENDIX C

Derivation of the objection functions of suspension model

Quarter car model with suspension architecture S5 is solved to obtain the analytical expression of discomfort. The equations of motion can be rewritten by substituting the mechanical admittance in (7.2),

$$\begin{aligned} m_1 s^2 x_1 + k_1(x_1 - r) - \left(k_2 + \frac{1}{\frac{1}{k_3 + s r_2} + \frac{1}{m_e s^2}} \right)(x_2 - x_1) = 0 \\ m_2 s^2 x_2 + \left(k_2 + \frac{1}{\frac{1}{k_3 + s r_2} + \frac{1}{m_e s^2}} \right)(x_2 - x_1) = 0 \end{aligned} \tag{C.1}$$

The transfer function between X_1 and r

$$X_1 = \frac{k_1(k_2 + m_2 s^2 + m_e s^2(k_3 + r_2 s))}{D(s)} \tag{C.2}$$

The transfer function between X_2 and r

$$X_2 = \frac{k_1(m_e s^2(k_2 + k_3 + r_2 s)) + k_2(k_3 + r_2 s)}{D(s)} \tag{C.3}$$

where the denominator D(s) is

$$\begin{aligned} D(s) =& s^6(m_1\ m_2\ m_e) + s^5\ r_2(m_2\ m_e + m_e\ m_1 + m_1\ m_2) \\ &+ s^4(k_1\ m_2\ m_e + k_2(m_1\ m_e + m_2\ m_e) \\ &+ k_3(m_1\ m_e + m_2\ m_e + m_1\ m_2)) \\ &+ s^3 r_2(k_1\ m_2 + k_2\ m_1 + k_2\ m_2 + k_1\ m_e) \\ &+ s^2(k_3\ m_2(k_1 + k_2) + k_1\ m_e(k_2 + k_3) + k_2\ k_3\ m_1) \\ &+ k_1 k_2 r_2 s + k_1 k_2 k_3 \end{aligned}$$

The transfer function between r and $\ddot{x}_2$ is

$$H_1(s) = s^2 X_2(s) \tag{C.4}$$

The standard deviation of the vertical acceleration can be derived by substituting (7.9) in (7.15).

$$\sigma_l = (A_b V)^{\frac{1}{2}} \|sX_2(s)\|_2 \tag{C.5}$$

The H2 norm for the transfer function $sX_2(s)$ is obtained using (7.18) and the value of L is written as,

$$L = \frac{1}{2a_0\ detH} \sum_{k=0}^{n-1} H_{k+1,1} \sum_{m=0}^{2k} (-1)^m\ A_m\ BB^T\ A_{2m-k}^T \tag{C.6}$$

where n is the degree of denominator of the transfer function, H is the Hurwitz matrix of order n, A and B are the characteristic and input matrices of the state space form. The term A_m can be obtained from (C.7).

$$A_m\ =\ AA_{m-1}\ +\ a_m E \tag{C.7}$$

where A_0 is the identity matrix (E). By substituting the auxiliary matrices from (C.7) and the Hurwitz matrix in (C.6), the explicit solution for Lyapunov equation can be

derived [119],

$$L = \begin{bmatrix} \frac{a_1(a_4a_1-a_2a_3-a_5)+a_3^2}{2a_0a_5L_0} & 0 & \frac{a_1a_2-a_3}{2a_0L_0} & 0 & \frac{a_5-a_1a_4}{2a_0L_0} \\ 0 & \frac{a_3-a_1a_2}{2a_0L_0} & 0 & \frac{a_1a_4-a_5}{2a_0L_0} & 0 \\ \frac{a_1a_2-a_3}{2a_0L_0} & 0 & \frac{a_5-a_1a_4}{2a_0L_0} & 0 & \frac{a_3a_4-a_2a_5}{2a_0L_0} \\ 0 & \frac{a_1a_4-a_5}{2a_0L_0} & 0 & \frac{a_3a_4-a_2a_5}{2a_0L_0} & 0 \\ \frac{a_5-a_1a_4}{2a_0L_0} & 0 & \frac{a_3a_4-a_2a_5}{2a_0L_0} & 0 & \frac{a_5a_2^2+(a_1a_4-a_3a_2-a_5)a_4}{2a_0L_0} \end{bmatrix}$$

$$L_0 = a_1^2a_4^4 + a_1a_2^2a_5 - a_1a_2a_3a_4 - 2a_1a_4a_5 - a_2a_3a_5 + a_3^2a_4a_5^2$$

The values for $a_1, a_2, ..., a_5$ are from the transfer function $sX_2(s)$.

$$\begin{aligned} a_0 &= 1, \\ a_1 &= (m_1m_2 + m_1m_e + m_2m_e)r_2/(m_1m_2m_e), \\ a_2 &= (k_3m_1m_2 + m_e(k_1m_2 + k_2m_1 + k_2m_2 + k_3m_1 + k_3m_2))/(m_1m_2m_e), \\ a_3 &= (k_1m_2r_2 + k_2m_1r_2 + k_2m_2r_2 + k1m_er_2)/(m_1m_2m_e), \\ a_4 &= (k_1k_3m_2 + k_2k_3m_1 + k_2k_3m_2 + (k_1k_2 + k_1k_3)m_e)/(m_1m_2m_e) \\ a_5 &= (k_1k_2r_2)/(m_1m_2m_e), \\ a_6 &= 0, a_7 = 0, a_8 = 0 \end{aligned}$$

The output matrix of the state space form consists of the coefficient from the numerator of the transfer function in (C.4).

$$\begin{aligned} b_0 &= 0, \\ b_1 &= (k_1r_2)/(m_1m_2), \\ b_2 &= (k_1(k_2 + k_3))/(m_1m_2), \\ b_3 &= (k_1k_2r_2)/(m_1m_2m_e) \\ b_4 &= (k_1k_2k_3)/(m_1m_2m_e) \end{aligned}$$

Using these constant values, the state space matrices and the Hurwitz matrix can be built and by substituting them in (7.18) and (7.15), the expression for discomfort can

be obtained.

$$\begin{aligned}\sigma_1 =&(A_b V)^{\frac{1}{2}}((d_1 + d_2 m_e^{-1} + d_3 m_e^{-2})r_2 + ((d_4 + d_5 m_e^{-1} \\ &+ d_6 m_e^{-2})k_3^2 - (d_2 + 2d_3 m_e^{-1})k_3 + d_7)m_e^{-1})\end{aligned} \tag{C.8}$$

$$\begin{aligned}where, d_1 &= (k_1)/(2m_2^2), \\ d_2 &= -(m_1 + m_2)k_2/m_2^2, \\ d_3 &= ((m_1 + m_2)^2 k_2^2 + m_2^2 k_1)/(2m_2^2 k_1) \\ d_4 &= (m_1 + m_2)/2m_2^2 \\ d_5 &= -(2(m_1 + m_2)^2 k_2 + m_2^2 k_1)/(2m_2^2 k_1) \\ d_6 &= ((m_1 + m_2)^3 k_2^2 + 2m_2^2(m_1 + m_2)k_1 k_2 + m_2^3 k_1^2)/(2(m_2 k_1)^2) \\ d_7 &= (m_1 + m_2)k_2^2/(2m_2^2)\end{aligned}$$

Similarly, the expressions of road holding and working space for the architecture S5 can be derived. For other suspension architectures, the equations motion need to be updated with corresponding mechanical admittance and then the same procedure can be followed.

List of Figures

List of Tables

Bibliography

[1] G. D'Errico, T. Cerri, and G. Pertusi, "Multi-objective optimization of internal combustion engine by means of 1d fluid-dynamic models," *Applied Energy*, vol. 88, no. 3, pp. 767–777, 2011.

[2] P. Zhang, K. Qian, C. Zhou, B. G. Stewart, and D. M. Hepburn, "A methodology for optimization of power systems demand due to electric vehicle charging load," *IEEE Transactions on Power Systems*, vol. 27, no. 3, pp. 1628–1636, 2012.

[3] K. Deb, K. Sindhya, and J. Hakanen, "Multi-objective optimization," in *Decision Sciences: Theory and Practice*. CRC Press, 2016, pp. 145–184.

[4] G. Mastinu, M. Gobbi, and C. Miano, *Optimal Design of Complex Mechanical Systems: With Applications to Vehicle Engineering*. Springer, 2007.

[5] K. Ramakrishnan, M. Gobbi, and G. Mastinu, "Multi-objective optimization of in-wheel motor powertrain and validation using vehicle simulator," in *Ecological Vehicles and Renewable Energies (EVER), 2015 Tenth International Conference on*. IEEE, 2015, pp. 1–9.

[6] K. Ramakrishnan, L. Yang, F. M. Ballo, M. Gobbi, and G. Mastinu, "Multi-objective optimization of road vehicle passive suspensions with inerter," in *ASME 2016 International Design Engineering Technical Conferences and Computers and Information in Engineering Conference*. American Society of Mechanical Engineers, 2016, pp. V003T01A007–V003T01A007.

[7] H. M. Kim, D. G. Rideout, P. Y. Papalambros, and J. L. Stein, "Analytical target cascading in automotive vehicle design," *Journal of Mechanical Design*, vol. 125, no. 3, pp. 481–489, 2003.

[8] R. D. Braun, "Collaborative optimization: an architecture for large-scale distributed design," 1996.

[9] W. Wang, "Network target coordination for design optimization of decomposed systems," Ph.D. dissertation, 2012.

[10] J. Sobieszczanski-Sobieski, J. S. Agte, and R. R. Sandusky, "Bilevel integrated system synthesis," *AIAA journal*, vol. 38, no. 1, pp. 164–172, 2000.

[11] O. L. Mangasarian and S. Fromovitz, "The fritz john necessary optimality conditions in the presence of equality and inequality constraints," *Journal of Mathematical Analysis and applications*, vol. 17, no. 1, pp. 37–47, 1967.

[12] B. Zhang, Z. Chen, C. Mi, and Y. L. Murphey, "Multi-objective parameter optimization of a series hybrid electric vehicle using evolutionary algorithms," in *Vehicle Power and Propulsion Conference, 2009. VPPC'09. IEEE*. IEEE, 2009, pp. 921–925.

[13] H. M. Kim, N. F. Michelena, P. Y. Papalambros, and T. Jiang, "Target cascading in optimal system design," *Journal of mechanical design*, vol. 125, no. 3, pp. 474–480, 2003.

[14] N. Michelena, H. Park, and P. Y. Papalambros, "Convergence properties of analytical target cascading," *AIAA journal*, vol. 41, no. 5, pp. 897–905, 2003.

[15] M. R. Kianifar and I. F. Campean, "Analytical target cascading framework for engine calibration optimisation," *International Journal of Powertrains*, vol. 3, no. 3, pp. 279–302, 2014.

[16] M. R. Kianifar and F. Campean, "Application of analytical target cascading for engine calibration optimization problem," in *ASME 2014 International Design Engineering Technical Conferences and Computers and Information in Engineering Conference*. American Society of Mechanical Engineers, 2014, pp. V02BT03A036–V02BT03A036.

[17] M. R. Kianifar, F. Campean, T. Beattie, and D. Richardson, "Analytical target cascading framework for diesel engine calibration optimisation," SAE Technical Paper, Tech. Rep., 2014.

[18] Z. Li, M. Kokkolaras, P. Papalambros, and S. J. Hu, "Product and process tolerance allocation in multistation compliant assembly using analytical target cascading," *Journal of Mechanical Design*, vol. 130, no. 9, p. 091701, 2008.

[19] J. J. Michalek, F. M. Feinberg, and P. Y. Papalambros, "Linking marketing and engineering product design decisions via analytical target cascading," *Journal of Product Innovation Management*, vol. 22, no. 1, pp. 42–62, 2005.

[20] A. E. Bayrak, N. Kang, and P. Y. Papalambros, "Decomposition-based design optimization of hybrid electric powertrain architectures: Simultaneous configuration and sizing design," *Journal of Mechanical Design*, vol. 138, no. 7, p. 071405, 2016.

[21] M. Gobbi, I. Haque, P. Papalambros, and G. Mastinu, "A critical review of optimization methods for road vehicles design," in *11th AIAA/ISSMO Multidisciplinary Analysis and Optimization Conference*, 2006, p. 6998.

[22] D. W. Gao, C. Mi, and A. Emadi, "Modeling and simulation of electric and hybrid vehicles," *Proceedings of the IEEE*, vol. 95, no. 4, pp. 729–745, April 2007.

[23] A. Urlaub, *Verbrennungsmotoren:Grundlagen, Verfahrenstheorie, Konstruktion*. Springer, 1995, vol. 1.

[24] G. R. . L. G. . B. Baumann, "Unified modeling of hybrid electric vehicle drivetrains," *IEEE/ASME Transactions on Mechatronics*, vol. 4, no. 3, pp. 246 – 257, 2002.

[25] S. Stipetic and J. Goss, "Calculation of efficiency maps using scalable saturated flux-linkage and loss model of a synchronous motor," in *2016 XXII International Conference on Electrical Machines (ICEM)*, Sept 2016, pp. 1380–1386.

[26] J. Goss, P. Mellor, R. Wrobel, D. Staton, and M. Popescu, "The design of AC permanent magnet motors for electric vehicles: A computationally efficient model of the operational envelope," in *6th IET International Conference on Power Electronics, Machines and Drives (PEMD 2012),*, March 2012, pp. 1–6.

[27] J. Goss, M. Popescu, D. Staton, R. Wrobel, J. Yon, and P. Mellor, "A comparison between maximum torque/ampere and maximum efficiency control strategies in ipm synchronous machines," in *Energy Conversion Congress and Exposition (ECCE), 2014 IEEE*, Sept 2014, pp. 2403–2410.

[28] S. Stipetic, D. Zarko, and M. Popescu, "Scaling laws for synchronous permanent magnet machines," in *Tenth International Conference on Ecological Vehicles and Renewable Energies,EVER-2015*, March 2015, pp. 1–7.

[29] ——, "Ultra-fast axial and radial scaling of synchronous permanent magnet machines," *IET Electric Power Applications*, April 2016.

[30] S. Stipetic, "Optimization of electromagnetic design of synchronous permanent magnet motor series," Ph.D. dissertation, University of Zagreb, Croatia, 2014.

[31] D. Zarko and S. Stipetic, "Criteria for optimal design of interior permanent magnet motor series," in *2012 XXth International Conference on Electrical Machines*, Sept 2012, pp. 1242–1249.

[32] Z. Zhu, D. Howe, E. Bolte, and B. Ackermann, "Instantaneous magnetic field distribution in brushless permanent magnet dc motors. i. open-circuit field," *IEEE Transactions on Magnetics*, vol. 29, no. 1, pp. 124–135, 1993.

[33] D. Žarko, D. Ban, T. Lipo *et al.*, "Analytical solution for cogging torque in surface permanent-magnet motors using conformal mapping," *IEEE Transactions on Magnetics*, vol. 44, no. 1, pp. 52–65, 2008.

[34] K. Boughrara, D. Zarko, R. Ibtiouen, O. Touhami, and A. Rezzoug, "Magnetic field analysis of inset and surface-mounted permanent-magnet synchronous motors using schwarz–christoffel transformation," *IEEE Transactions on Magnetics*, vol. 45, no. 8, pp. 3166–3178, 2009.

[35] B. L. J. Gysen, K. J. Meessen, J. J. H. Paulides, and E. A. Lomonova, "General formulation of the electromagnetic field distribution in machines and devices using fourier analysis," *IEEE Transactions on Magnetics*, vol. 46, no. 1, pp. 39–52, Jan 2010.

[36] R. L. J. Sprangers, B. L. J. Gysen, J. J. H. Paulides, J. Waarma, and E. A. Lomonova, "Calculation of induced rotor current in induction motors using a slotted semi-analytical harmonic model," in *16th European Conference on Power Electronics and Applications, ECCE-2014*, Aug 2014, pp. 2700–2705.

[37] R. L. J. Sprangers, B. L. J. Gysen, J. J. H. Paulides, and E. A. Lomonova, "A fast semi-analytical model for the slotted structure of induction motors with 36/28 stator/rotor slot combination," in *ELECTRIMACS 2014*, May 2014.

[38] E. Ilhan, B. L. J. Gysen, J. J. H. Paulides, and E. A. Lomonova, "Analytical hybrid model for flux switching permanent magnet machines," *IEEE Transactions on Magnetics*, vol. 46, no. 6, pp. 1762–1765, June 2010.

[39] R. Sprangers, J. Paulides, B. Gysen, and E. Lomonova, "Magnetic saturation in semi-analytical harmonic modeling for electric machine analysis," *IEEE Transactions on Magnetics*, vol. 52, no. 2, pp. 1–10, 2016.

[40] R. L. J. Sprangers, J. J. H. Paulides, B. L. J. Gysen, J. Waarma, and E. A. Lomonova, "Semi-analytical framework for synchronous reluctance motor analysis including finite soft-magnetic material permeability," *IEEE Transactions on Magnetics*, vol. PP, no. 99, pp. 1–1, 2015.

[41] M. Curti, J. Paulides, and E. Lomonova, "An overview of analytical methods for magnetic field computation," in *Tenth International Conference on Ecological Vehicles and Renewable Energies (EVER), 2015*, March 2015, pp. 1–7.

[42] B. Hague, *The principles of electromagnetism applied to electrical machines: (formerly titled: Electromagnetic problems in electrical engineering).* Dover Publications, 1962.

[43] K. J. Binns, C. Trowbridge, and P. Lawrenson, *The analytical and numerical solution of electric and magnetic fields*. Wiley, 1992.

[44] E. P. Furlani, *Electric Machines and Drives*, I. Mayergoyz, Ed. Acadenic Press, 2001.

[45] D. Zarko, D. Ban, and T. A. Lipo, "Analytical calculation of magnetic field distribution in the slotted air gap of a surface permanent-magnet motor using complex relative air-gap permeance," *IEEE Transactions on Magnetics*, vol. 42, no. 7, pp. 1828–1837, 2006.

[46] K. Ramakrishnan, P. Romanazzi, D. Zarko, G. Mastinu, D. A. Howey, and A. Miotto, "Improved analytical model for outer rotor surface permanent magnet machine for efficiency calculation with thermal effect," *SAE International Journal of Alternative Powertrains*, vol. 6, no. 2017-01-0185, 2017.

[47] M. C. Smith, "Synthesis of mechanical networks: the inerter," *IEEE Transactions on Automatic Control*, vol. 47, no. 10, pp. 1648–1662, 2002.

[48] M. C. Smith and F.-C. Wang, "Performance benefits in passive vehicle suspensions employing inerters," *Vehicle system dynamics*, vol. 42, no. 4, pp. 235–257, 2004.

[49] M. C. Smith and G. W. Walker, "Performance limitations and constraints for active and passive suspensions: a mechanical multi-port approach," *Vehicle System Dynamics*, vol. 33, no. 3, pp. 137–168, 2000.

[50] F. Scheibe and M. C. Smith, "Analytical solutions for optimal ride comfort and tyre grip for passive vehicle suspensions," *Vehicle System Dynamics*, vol. 47, no. 10, pp. 1229–1252, 2009.

[51] M. Gobbi, F. Levi, and G. Mastinu, "Multi-objective stochastic optimisation of the suspension system of road vehicles," *Journal of sound and vibration*, vol. 298, no. 4, pp. 1055–1072, 2006.

[52] P. Romanazzi, V. Galizzi, F. Carbone, A. Miotto, and D. Howey, "Improved thermal equivalent circuit element applied to an external rotor spm machine," in *XXII International Conference on Electrical Machines, ICEM 2016*. IEEE, 2016, pp. 2718–2724.

[53] D. Kurtz and J. Marte, "A review of Aerodynamic Noise from Propellers rotors and lift fans," NASA, Tech. Rep., 1970.

[54] K. Maliti, "Modelling and analysis of magnetic noise in squirrel-cage induction motors," Ph.D. dissertation, Kungl Tekniska Högskolan, Stockholm, 2000.

[55] J. Le Besnerais, "Réduction du bruit audible d'origine magnétique dans les machines asynchrones alimentées par MLI â - règles de conception silencieuse et optimisation multi-objectif," Ph.D. dissertation, Ecole Centrale de Lille, 2008.

[56] G. Myrria, F. Chauvicourt, and C. Faria, "Evaluation of the influence of the control strategy of the electric vehicle's motor on its radiated noise using 1d simulation," *EuroRegio*, June 2016.

[57] M. Gobbi, I. Haque, P. Papalambros, and G. Mastinu, "Optimization and integration of ground vehicle systems," *Vehicle System Dynamics*, vol. 43, no. 6-7, pp. 437–453, 2005.

[58] M. Gobbi, F. Levi, G. Mastinu, and G. Previati, "On the analytical derivation of the pareto-optimal set with applications to structural design," *Structural and Multidisciplinary Optimization*, vol. 51, no. 3, pp. 645–657, 2015.

[59] K. Miettinen, *Nonlinear multiobjective optimization*. Springer Science & Business Media, 2012, vol. 12.

[60] F. BALLO, "Optimal structural design for improving safety of road vehicles," 2015.

[61] I. L. Dalal, D. Stefan, and J. Harwayne-Gidansky, "Low discrepancy sequences for monte carlo simulations on reconfigurable platforms," in *International Conference on Application-Specific Systems, Architectures and Processors, 2008. ASAP 2008.* IEEE, 2008, pp. 108–113.

[62] K. Miettinen, *Nonlinear Multiobjective Optimization*. Springer Science & Business Media, 1999, vol. 12.

[63] S. S. Askar and A. Tiwari, "Finding exact solutions for multi-objective optimisation problems using a symbolic algorithm," in *Proceedings of the Eleventh conference on Congress on Evolutionary Computation*. IEEE Press, 2009, pp. 24–30.

[64] D. Kim, G. Lee, B. Lee, and S. Cho, "Counterexample and optimality conditions in differentiable multiobjective programming," *Journal of Optimization Theory and Applications*, vol. 109, no. 1, pp. 187–192, 2001.

[65] I. Marusciac, "On the fritz john type optimality criterion in multi-objective goal programming," *Revue d'Analyse Numerique et de Theorie de l'Approximation*, vol. 11, no. 1-2, 1982.

[66] F. Levi and M. Gobbi, "An application of analytical multi-objective optimization to truss structures," in *11th AIAA/ISSMO Multidisciplinary Analysis and Optimization Conference*, 2006, p. 6975.

[67] M. Gobbi, G. Previati, F. Ballo, and G. Mastinu, "Bending of beams of arbitrary cross sections-optimal design by analytical formulae," *Structural and Multidisciplinary Optimization*, pp. 1–12, 2016.

[68] A. Björck, *Numerical methods for least squares problems*. Siam, 1996.

[69] C. D. Meyer, *Matrix analysis and applied linear algebra*. Siam, 2000, vol. 2.

[70] J. T. Allison, "Complex system optimization: A review of analytical target cascading, collaborative optimization, and other formulations," Ph.D. dissertation, The University of Michigan, 2004.

[71] S. Tosserams, L. Etman, P. Papalambros, and J. Rooda, "An augmented lagrangian relaxation for analytical target cascading using the alternating direction method of multipliers," *Structural and multidisciplinary optimization*, vol. 31, no. 3, pp. 176–189, 2006.

[72] E. A. Lomonova, J. J. H. Paulides, S. Wilkins, and J. Tegenbosch, "Adept: "advanced electric powertrain technology" - virtual and hardware platforms," in *Tenth International Conference on Ecological Vehicles and Renewable Energies (EVER), 2015*, March 2015, pp. 1–10.

[73] J. W. Jansen, J. P. C. Smeets, T. T. Overboom, J. M. M. Rovers, and E. A. Lomonova, "Overview of analytical models for the design of linear and planar motors," *IEEE Transactions on Magnetics*, vol. 50, no. 11, pp. 1–7, Nov 2014.

[74] Z. Q. Zhu, L. J. Wu, and Z. P. Xia, "An accurate subdomain model for magnetic field computation in slotted surface-mounted permanent-magnet machines," *IEEE Transactions on Magnetics*, vol. 46, no. 4, pp. 1100–1115, April 2010.

[75] L. J. Wu, Z. Q. Zhu, D. A. Staton, M. Popescu, and D. Hawkins, "Comparison of analytical models of cogging torque in surface-mounted pm machines," *IEEE Transactions on Industrial Electronics*, vol. 59, no. 6, pp. 2414–2425, June 2012.

[76] K. Ramakrishnan, M. Curti, D. Zarko, G. Mastinu, J. J. Paulides, and E. A. Lomonova, "Comparative analysis of various methods for modelling surface permanent magnet machines," *IET Electric Power Applications*, vol. 11, no. 4, pp. 540–547, 2017.

[77] D. C. Hanselman, *Brushless permanent magnet motor design*. The Writers' Collective, 2003.

[78] M. N. Sadiku, *Numerical techniques in electromagnetics*. CRC press, 2000.

[79] R. Rabinovici, "Magnetic field analysis of permanent magnet motors," *IEEE Transactions on Magnetics*, vol. 32, no. 1, pp. 265–269, 1996.

[80] H. Gavin, "The levenberg-marquardt method for nonlinear least squares curve-fitting problems," *Department of Civil and Environmental Engineering, Duke University*, pp. 1–15, 2011.

[81] D. Zarko, D. Ban, and T. A. Lipo, "Analytical solution for cogging torque in surface permanent-magnet motors using conformal mapping," *IEEE Transactions on Magnetics*, vol. 44, no. 1, pp. 52–65, 2008.

[82] ——, "Analytical solution for electromagnetic torque in surface permanent-magnet motors using conformal mapping," *IEEE Transactions on Magnetics*, vol. 45, no. 7, pp. 2943–2954, 2009.

[83] T. O'Connell and P. Krein, "The schwarz-christoffel analytical method applied to electric machine slot shape optimization," in *International Conference on Electric Machines & Drives, (IEMDC), Antalya, Turkey, 3-5 May 2007*, vol. 1. IEEE, 2007, pp. 341–346.

[84] T. C. O'Connell and P. T. Krein, "A schwarz–christoffel-based analytical method for electric machine field analysis," *IEEE Transactions on Energy Conversion*, vol. 24, no. 3, pp. 565–577, 2009.

[85] D. Krop, E. Lomonova, and A. Vandenput, "Application of schwarz-christoffel mapping to permanent-magnet linear motor analysis," *IEEE Transactions on Magnetics*, vol. 44, no. 3, pp. 352–359, 2008.

[86] K. Boughrara, R. Ibtiouen, D. Zarko, O. Touhami, and A. Rezzoug, "Magnetic field analysis of external rotor permanent-magnet synchronous motors using conformal mapping," *IEEE Transactions on Magnetics*, vol. 46, no. 9, pp. 3684–3693, 2010.

[87] K. Ramakrishnan, D. Zarko, A. Hanic, and G. Mastinu, "Improved method for field analysis of surface permanent magnet machines using schwarz–christoffel transformation," *IET Electric Power Applications*, 2017.

[88] L. N. Trefethen, *Spectral Methods in MatLab*. Philadelphia, PA, USA: Society for Industrial and Applied Mathematics, 2000.

[89] Z. Zhu and D. Howe, "Analytical prediction of the cogging torque in radial-field permanent magnet brushless motors," *IEEE transactions on magnetics*, vol. 28, no. 2, pp. 1371–1374, 1992.

[90] R. De Doncker, D. W. Pulle, and A. Veltman, *Advanced electrical drives: analysis, modeling, control*. Springer Science & Business Media, 2010.

[91] T. Markel, A. Brooker, T. Hendricks, V. Johnson, K. Kelly, B. Kramer, M. O'Keefe, S. Sprik, and K. Wipke, "Advisor: a systems analysis tool for advanced vehicle modeling," *Journal of power sources*, vol. 110, no. 2, pp. 255–266, 2002.

[92] K. B. Wipke, M. R. Cuddy, and S. D. Burch, "Advisor 2.1: a user-friendly advanced powertrain simulation using a combined backward/forward approach," *IEEE Transactions on Vehicular Technology*, vol. 48, no. 6, pp. 1751–1761, Nov 1999.

[93] ADVISOR, *version 2003*. National Renewable Energy Laboratory: Alliance for Sustainable Energy, LLC, 2003.

[94] QSS-toolbox, *version 2.0.1*. Department of Mechanical and Process Engineering, ETH Zurich: Institute for Dynamic Systems and Control, 2013.

[95] J. Heywood, *Internal combustion engine fundamentals*. McGraw-Hill Education, 1988.

[96] G. Rizzoni, L. Guzzella, and B. M. Baumann, "Unified modeling of hybrid electric vehicle drivetrains," *IEEE/ASME transactions on mechatronics*, vol. 4, no. 3, pp. 246–257, 1999.

[97] S. Stipetic and J. Goss, "Calculation of efficiency maps using scalable saturated flux-linkage and loss model of a synchronous motor," in *International conference on Electrical Machines - ICEM, 2016 IEEE*, September 2016, pp. 1–6.

[98] S. Stipetic, D. Zarko, and M. Popescu, "Ultra-fast axial and radial scaling of synchronous permanent magnet machines," *IET Electric Power Applications*, vol. 10, no. 7, pp. 658–666, 2016.

[99] J. Goss, M. Popescu, D. Staton, R. Wrobel, J. Yon, and P. Mellor, "A comparison between maximum torque/ampere and maximum efficiency control strategies in ipm synchronous machines," in *Energy Conversion Congress and Exposition (ECCE), 2014 IEEE*, Sept 2014, pp. 2403–2410.

[100] P. Mellor, R. Wrobel, and N. Simpson, "Ac losses in high frequency electrical machine windings formed from large section conductors," in *IEEE Energy Conversion Congress and Exposition, ECCE-2014*. IEEE, 2014, pp. 5563–5570.

[101] F. Deng, "Commutation-caused eddy-current losses in permanent-magnet brushless dc motors," *IEEE Transactions on Magnetics*, vol. 33, no. 5, pp. 4310–4318, 1997.

[102] J. Gieras, *Permanent Magnet Motor Technology: Design and Applications, Third Edition*, ser. Electrical and Computer Engineering. CRC Press, 2011.

[103] Motor Design Ltd., "Motor-CAD / Motor-LAB software." [Online]. Available: http://www.motor-design.com/motorlab.php

[104] A. Boglietti, A. Cavagnino, D. Staton, M. Shanel, M. Mueller, and C. Mejuto, "Evolution and modern approaches for thermal analysis of electrical machines," *IEEE Transactions on industrial electronics*, vol. 56, no. 3, pp. 871–882, 2009.

[105] D. Staton, A. Boglietti, and A. Cavagnino, "Solving the more difficult aspects of electric motor thermal analysis in small and medium size industrial induction motors," *IEEE Transactions on Energy Conversion*, vol. 20, no. 3, pp. 620–628, 2005.

[106] B. Xu, P.-W. Li, and C. L. Chan, "Extending the validity of lumped capacitance method for large biot number in thermal storage application," *Solar Energy*, vol. 86, no. 6, pp. 1709–1724, 2012.

[107] P. Romanazzi, M. Bruna, and D. A. Howey, "Thermal homogenization of electrical machine windings applying the multiple-scales method," *Journal of Heat Transfer*, vol. 139, no. 1, p. 012101, 2017.

[108] Z. Huang, F. J. Márquez-Fernández, Y. Loayza, A. Reinap, and M. Alaküla, "Dynamic thermal modeling and application of electrical machine in hybrid drives," in *International Conference on Electrical Machines (ICEM), 2014*. IEEE, 2014, pp. 2158–2164.

[109] C. Kral, A. Haumer, and T. Bauml, "Thermal model and behavior of a totally-enclosed-water-cooled squirrel-cage induction machine for traction applications," *IEEE Transactions on Industrial Electronics*, vol. 55, no. 10, pp. 3555–3565, 2008.

[110] A. S. Murthy, D. P. Magee, and D. G. Taylor, "Vehicle braking strategies based on regenerative braking boundaries of electric machines," in *Transportation Electrification Conference and Expo (ITEC), 2015 IEEE*. IEEE, 2015, pp. 1–6.

[111] D. Žarko, "A systematic approach to optimized design of permanent magnet motors with reduced torque pulsations," Ph.D. dissertation, Department of Electrical and Computer Engineering, University of Wisconsin-Madison, 2004.

[112] B. Weilharter, O. Biro, H. Lang, G. Ofner, and S. Rainer, "Validation of a Comprehensive Analytic Noise Computation Method for Induction Machines," *IEEE Transactions on Industrial Electronics*, vol. 59, no. 5, pp. 2248–2257, May 2012.

[113] M. Gobbi and G. Mastinu, "Analytical description and optimization of the dynamic behaviour of passively suspended road vehicles," *Journal of sound and vibration*, vol. 245, no. 3, pp. 457–481, 2001.

[114] W. F. Milliken and D. L. Milliken, *Race car vehicle dynamics*. Society of Automotive Engineers Warrendale, 1995, vol. 400.

[115] X. Sun, L. Chen, S. Wang, C. Yuan, and X. Zhang, "Analysis of vibration isolation performance for nolinear inerter-spring-damper suspension," *Transactions of the Chinese Society of Agricultural Engineering*, vol. 29, no. 23, pp. 38–45, 2013.

[116] M. Guiggiani, *The Science of Vehicle Dynamics: Handling, Braking, and Ride of Road and Race Cars*. Springer Science & Business Media, 2014.

[117] X.-J. Zhang, M. Ahmadian, and K.-H. Guo, "On the benefits of semi-active suspensions with inerters," *Shock and Vibration*, vol. 19, no. 3, pp. 257–272, 2012.

[118] C. Dodds and J. Robson, "The description of road surface roughness," *Journal of sound and vibration*, vol. 31, no. 2, pp. 175–183, 1973.

[119] P. C. Müller and W. Schiehlen, *Linear vibrations: a theoretical treatment of multi-degree-of-freedom vibrating systems*. Springer Science & Business Media, 2012, vol. 7.

[120] G. Mastinu and M. Gobbi, "On the optimal design of railway passenger vehicles," *Proceedings of the Institution of Mechanical Engineers, Part F: Journal of Rail and Rapid Transit*, vol. 215, no. 2, pp. 111–124, 2001.

[121] J. C. Doyle, B. A. Francis, and A. R. Tannenbaum, *Feedback control theory*. Courier Corporation, 2013.

[122] G. Mastinu and M. Ploechl, *Road and Off-Road Vehicle System Dynamics Handbook*. CRC Press, 2014.

[123] A. Iqbal, A. Lamine, I. Ashraf *et al.*, "Matlab/simulink model of space vector pwm for three-phase voltage source inverter," in *Universities Power Engineering Conference, 2006. UPEC'06. Proceedings of the 41st International*, vol. 3. IEEE, 2006, pp. 1096–1100.

[124] A. Iqbal, S. M. Ahmed, M. A. Khan, and H. Abu-Rub, "Generalised simulation and experimental implementation of space vector pwm technique of a three-phase voltage source inverter," *International Journal of Engineering, Science and Technology*, vol. 2, no. 1, pp. 1–12, 2010.

[125] B. Wu and M. Narimani, *High-power converters and AC drives*. John Wiley & Sons, 2017.

[126] W. Hassan and B. Wang, "Efficiency optimization of pmsm based drive system," in *Power Electronics and Motion Control Conference (IPEMC), 2012 7th International*, vol. 2. IEEE, 2012, pp. 1027–1033.

[127] F. Administration, "The code of federal regulations of the united states of america," p. 10 CRF 420.1, 1996.

[128] E. Haug and J. Arora, "Introduction to optimal design," *McGrawHill, NewYork*, 1989.

[129] J. D'Errico, "Bound constrained optimization using fminsearch: fminsearchbnd. matlab® central," 2005.

[130] J. F. Gieras, *Permanent magnet motor technology: design and applications*. CRC press, 2002.

[131] T. A. Lipo, *Introduction to AC machine design*. Wisconsin Power Electronics Research Center, University of Wisconsin, 2004.

[132] M. Liwschitz-Garik and . Whipple, "Electric machinery, volume ii of ac machines," 1950.